DOCTOR OF PHILOSOPHY

Adaptive optics stimulated emission depletion microscope for thick sample imaging

Zdankowski, Piotr

Award date:
2018

UNIVERSITY OF DUNDEE

DOCTORAL THESIS

Adaptive optics stimulated emission depletion microscope for thick sample imaging

Author:
Piotr ZDANKOWSKI

Supervisors:
Prof. Jason R. SWEDLOW
Dr. David MCGLOIN

A thesis submitted in fulfillment of the requirements for the degree of Doctor of Philosophy in the

Gene Regulation and Expression
School of Life Sciences

July 18, 2018

Declaration of Authorship

I, Piotr ZDANKOWSKI, declare that this thesis titled, "Adaptive optics stimulated emission depletion microscope for thick sample imaging" and the work presented in it are my own. I confirm that:

- This work was done wholly or mainly while in candidature for a research degree at this University.
- Where any part of this thesis has previously been submitted for a degree or any other qualification at this University or any other institution, this has been clearly stated.
- Where I have consulted the published work of others, this is always clearly attributed.
- Where I have quoted from the work of others, the source is always given. With the exception of such quotations, this thesis is entirely my own work.
- I have acknowledged all main sources of help.
- Where the thesis is based on work done by myself jointly with others, I have made clear exactly what was done by others and what I have contributed myself.

Signed:

Date: 20 July 2018

"*Our freedom to doubt was born out of a struggle against authority in the early days of science. It was a very deep and strong struggle: permit us to question — to doubt — to not be sure. I think that it is important that we do not forget this struggle and thus perhaps lose what we have gained.*"

Richard Feynman

In memory of my late father.
To my mother with love and appreciation.

Abstract

Adaptive optics stimulated emission depletion microscope for thick sample imaging

by Piotr ZDANKOWSKI

Over the past few decades, fluorescence microscopy has proven to become the most widely used imaging technique in the field of life sciences. Unfortunately, all classical optical microscopy techniques have one thing in common: their resolution is limited by the diffraction. Thankfully, due to the very strong interest, development of fluorescent microscopy techniques is very intense, with novel solutions surfacing repeatedly. The major breakthrough came with the appearance of super-resolution microscopy techniques, enabling imaging well below the diffraction barrier and opening the new era of nanoscopy. Among the fluorescent super-resolution techniques, Stimulated Emission Depletion (STED) microscopy has been particularly interesting, as it is a purely optical technique which does not require post image processing. STED microscopy has proven to resolve structures down to the molecular resolution. However, super-resolution microscopy is not a cure to all the problems and it also has its limits. What has shown to be particularly challenging, was the super-resolution imaging of thick samples. With increased thickness of biological structures, the aberrations increase and signal-to-noise (SNR) decreases. This becomes even more evident in the super-resolution imaging, as the nanoscopic techniques are especially sensitive to aberrations and low SNR.

The aim of this work is to propose and develop a 3D STED microscope that can successfully image thick biological samples with nanoscopic resolution. In order to achieve that, adaptive optics (AO) has been employed for correcting the aberrations, using the indirect wavefront sensing approach. This thesis presents a custom built 3D STED microscope with the AO correction and the resulting images of thick samples with resolution beyond diffraction barrier. The developed STED microscope achieved the resolution of 60nm in lateral and 160nm in axial direction. What is more, it enabled super-resolution imaging of thick, aberrating samples. HeLa, RPE-1 cells and dopaminergic neuron differentiated from human IPS cells were imaged using the microscope. The results shown in this thesis present 3D STED imaging of thick biological samples and, what is particularly worth to highlight, 3D STED imaging at the 80μm depth, where the excitation and depletion beams have to propagate through the thick layer of tissue. 3D STED images at such depth has not been reported up to date.

Acknowledgements

I would like to thank all the people that helped me go through my postgraduate studies and enabled me writing up this thesis. Foremost, I want to show my gratitude to my supervisor, Prof. Jason R. Swedlow, for taking his time into guiding me through the work and pushing me forward, for his patience, advices and motivation. I have been lucky for having the supervisor that sincerely cared about me and my work. I would also like to thank the friends from Prof. Swedlow group, Michael Porter, for being patient and showing me important biological methods and protocols, without whom I would not be able to prepare experiments, and Iain Porter, for giving me guidance in sample preparation and for the culturing and preparation of iPS cell samples.

I would like to acknowledge Dr David McGloin, my second supervisor, for his tips and notes on optical systems, many discussions and useful feedback on my thesis.

I want to send my thanks to Prof. Martin Booth and his group, for allowing me to understand better adaptive optics and getting hands on experience with STED microscopy. I would like to thank Dr Brian Patton, for the discussions and many useful tips regarding STED microscopy.

A big thank you to all the people involved in the PHOQUS project, especially Wendy Phillips, for tireless reminders about all the paperwork, bureaucracy and deadlines I've been always forgetting about.

I want to show my gratefulness and sincere gratitude for all the PHOQUS friends, for being around when needed, for hours of discussions, for becoming good friends. Seeing the end of my PhD would not be possible without having them.

Finally, I want to show my greatest gratitude to my fiancée, Marta, for her her patience and understanding, love and caring, for constant support and motivation, for standing by in good and bad days. I want to thank my family, my mother and late father, my brother for their love and support. I would like to thank all my friends for their support and encouragement, for allowing me show them the beautiful Scottish highlands.

Lastly, I would like to thank the Marie Curie Actions of the European Union's Seventh Framework Programme (FP7/2007-2013), for funding the project.

Contents

Declaration of Authorship i

Abstract iv

Acknowledgements v

List of Figures viii

List of Tables xi

List of Abbreviations xii

1 Introduction 1

1.1 Fluorescence microscopy . . . 1

1.1.1 Widefield fluorescent microscope. . . . 2

1.1.2 Confocal fluorescent microscope. . . . 3

1.2 Physical image formation . . . 5

1.2.1 Resolution limit. . . . 9

1.3 Imaging beyond resolution limit . . . 12

1.3.1 General super-resolution techniques overview . . . 14

1.3.2 Single molecule localisation microscopy. . . . 16

1.3.3 Structured illumination microscopy. . . . 17

1.3.4 Stimulated emission depletion microscopy . . . 20

1.3.5 Conclusion and comparison of the currently available super-resolution techniques. . . . 23

1.4 STED Microscopy . . . 24

1.4.1 Pulsed STED microscopy . . . 25

1.4.2 CW-STED microscopy . . . 25

1.4.3 Photobleaching and strategies to its minimisation . . . 26

1.4.4 Depletion beam shaping and maximising STED efficiency . . . 27

1.4.5 Thick tissue imaging. . . . 29

1.4.6 Conclusions and overview of the next chapters . . . 29

2 Optical methods **30**
2.1 Design of the STED microscope . . . 30
2.1.1 Depletion laser beam path . . . 31
2.1.2 Excitation beam path . . . 35
2.1.3 Common beam path . . . 36
2.1.4 Imaging beam path . . . 36
2.1.5 Pinhole size calculations . . . 37
2.1.6 Filter Selection . . . 38
2.2 Image acquisition and formation . . . 39
2.3 Microscope control software . . . 43
2.4 Adaptive optics and aberration correction . . . 44

3 Experimental methods **51**
3.1 Super-resolution imaging of biological structures. . . . 51
3.1.1 Sample preparation. . . . 51

4 Characterisation of an Adaptive Optics STED microscope **56**
4.1 Evaluation of microscope performance using gold beads. . . . 56
4.1.1 Laser pulse measurements . . . 61
4.2 Fluorescent beads measurements . . . 61
4.3 Summary and conclusions of the microscope performance evaluation. 66

5 Biological samples imaging results. **67**
5.1 Imaging of HeLa and RPE-1 cells microtubules. . . . 67
5.2 Mitotic spindle imaging of the RPE-1 cells. . . . 68
5.3 Dual colour imaging . . . 71
5.4 iPS cells imaging . . . 73

6 Conclusions and outlook. **80**
6.1 Outlook . . . 80
6.1.1 Image deconvolution . . . 80
6.1.2 Possible system upgrades . . . 83
6.2 Conclusions . . . 86

A Parts list table **88**

B Matlab Code **91**

Bibliography **96**

List of Figures

1.1 Jablonsky diagram for spontaneous emission 1
1.2 Excitation and detection in the fluorescent microscope 2
1.3 The concept of the confocal microscope 3
1.4 Comparison of images acquired with confocal and widefield microscope 4
1.5 Graphical representation of image formation according to Abbe Theory 5
1.6 Graphical representation of image formation according to Abbe Theory in 4f imaging system 6
1.7 Imaging of a point object by the optical system 7
1.8 3D representation of the Airy disk 9
1.9 Graphical interpretation of image formation through convolution. . . 10
1.10 Graphical representation of Rayleigh criterion when imaging two points 10
1.11 3D Intensity distribution in the PSF according to the Born & Wolf paraxial approximation 11
1.12 Relation between resolution and a) wavelength; b)numerical aperture. 12
1.13 Comparison of super-resolution microscopy techniques 14
1.14 Comparison of the performance and application of the most common fluorescent microscopy techniques 15
1.15 Image acquisition in SMLM microscopy 16
1.16 Comparison of OTF in widefield, 2D SIM and 3D SIM microscopes . . 18
1.17 Moiré pattern generation 19
1.18 Jablonski diagram of spontaneous and stimulated emission 21
1.19 Comparison of confocal and STED image scanning 22
1.20 Comparison of the common STED phase masks 22
1.21 Effects of STED phase mask misalignment to the final shape of the depletion beam 28

2.1 Schematic of the designed STED microscope 31
2.2 Photographs of the built STED microscope 32
2.3 Images of Top Hat phase mask acquired in the intermediate imaging planes of the depletion beam path 33
2.4 Locations of Top Hat phase masks with regard to the microscope setup 34
2.5 Calculation of the size of the phase mask at the BFP 34

2.6 Spectra graphs for Atto647 dye and chosen microscope filters 38
2.7 Spectra graphs for Abberior STAR635P dye and chosen microscope filters 39
2.8 Spectra graphs for Abberior STAR470SXP dye and chosen microscope filters 39
2.9 Image acquisition in the laser scanning microscope 40
2.10 Nonlinearity in the resonant scanning movement resulting in the elongation of the acquired image 41
2.11 Application of Ronchi grating for obtaining constant pixel clock . . . 42
2.12 Block diagram of the image acquisition module of microscope control software. 43
2.13 Principle of LC devices operation 44
2.14 Aberration correction with adaptive optics 45
2.15 Graphical representation of Zernike polynomials 46
2.16 Workflow of the aberration correction routine 47
2.17 Aberration correction routine using the indirect wavefront sensing approach 48
2.18 Gaussian fit curves obtained in the process of aberration correction and a resulting phase mask 50

4.1 Simulated PSF for the excitation beam 57
4.2 Simulated PSF for the depletion beam 58
4.3 Excitation beam PSF obtained through imaging of the gold beads . . 59
4.4 Depletion beam PSF obtained through imaging of the gold beads . . 59
4.5 depletion beam shape imaged with gold beads 60
4.6 Spatial alignment of depletion and excitation beams 60
4.7 Pulse measurements of excitation and depletion beams 61
4.8 Comparison of fluorescent beads images obtained with confocal, 2D STED and 3D STED modes 62
4.9 PSF measurement by imaging fluorescent beads for confocal, 2D STED and 3D STED microscope modes 63
4.10 Calculated average axial and lateral FWHM of the STED microscope 63
4.11 Graph showing the relation between resolution and depletion laser power 64
4.12 Graph showing the relation between resolution and pulse delay of the depletion beam 65

5.1 Microtubules of HeLa cells imaged with confocal, 2D STED and 3D STED microscope modes 68
5.2 Confocal, 2D STED and 3D STED images of the RPE-1 mitotic spindle 69
5.3 Cross-sections of the microtubules and Gaussian fit 69
5.4 Confocal, 2D STED and 3D STED images of the RPE-1 mitotic spindle in the early anaphase 70
5.5 Confocal and 2D STED images of mitotic cell obtained with the 488nm excitation laser 71
5.6 Confocal, 2D STED and 3D STED dual colour 3D MIP projection of mitotic cell 72
5.7 Confocal, 2D STED and 3D STED axon end images of the iPS cells . . 74
5.8 Image of the iPS cell tissue stack 74
5.9 Large field of view image stack of the iPS cell tissue with axon located at 80μm 75
5.10 Confocal, aberration corrected 3D STED and not corrected 3D STED image of iPS cell axon acquired at the 80µm depth within tissue . . . 76
5.11 Phase applied to the depletion beam SLM and corresponding Zernike modes used for aberration correction for deep tissue imaging. 77
5.12 Large FOV image of the cell body of the axon located at 80µm depth 77
5.13 Confocal and 3D STED image of the cell body of the axon located at 80µm depth 78

6.1 Image deconvolution 81
6.2 Comparison of raw and deconvolved 2D STED images of fluorescent beads 82
6.3 2D STED and deconvolved 2D STED plots and FWHM of the fluorescent beads 82

List of Tables

2.1 Zernike modes and their mathematical representation that are corrected in the aberration correction procedure 49

4.1 FWHM for the simulated 637nm excitation beam 57
4.2 FWHM for the simulated 766nm depletion beam 58
4.3 Calculated FWHM of the excitation laser PSF 58
4.4 Calculated FWHM of the depletion laser PSF 59
4.5 Lateral resolution of the STED microscope for different depletion laser intensity 64
4.6 STED microscope resolution for different depletion laser pulse delay values 65

A.1 Parts numbers and names used in the built STED microscope. 88
A.1 Parts numbers and names used in the built STED microscope. 89
A.1 Parts numbers and names used in the built STED microscope. 90

List of Abbreviations

2D	2-Dimensional
3D	3-Dimensional
4D	4-Dimensional
AO	Adaptive Optics
APD	Avalanche Photodiode
AU	Airy Units
A.U.	Arbitrary Units
BFP	Back Focal Plane
CCD	Charge-Coupled Device
CMOS	Complementary Metal-Oxide-**S**emiconductor
CW	Continuous Wave
CLSM	Confocal Laser Scanning Microscope
DM	Dichroic Mirror
EM	Electron Microscope
EF	Emission Filter
FOV	Field Of View
FPGA	Field-Programmable Gate Array
FPS	Frames Per Second
FT	Fourier Transform
FWHM	Full Width at Half Maximum
GFP	Green Fluorescent Protein
GLP	Glan-Laser Polariser
GM	Galvanometric (Galvo) Mirror
GPU	Graphics Processing Unit
GSD	Ground State Depletion
GSDIM	Ground State Depletion microscopy followed by Individual Molecule return
I^5M	Image interference imaging Microscopy
iPS	Induced pluripotent stem cells
LC	Liquid Crystal
LCoS	Liquid Crystal on Silicon
LS	Light Sheet
LSM	Laser Scanning Microscopy
MIP	Maximum Intensity Projection
MO	Microscope Objective
MMF	Multi-Mode Fibre
MPPC	Multi Pixel Photon Counter
NA	Numerical Aperture
NL	Non-Linear
OD	Optical Density
OPD	Optical Path Difference

OTF	Optical Transfer Function
paGFP	Photoactivatable Green Fluorescent Protein
PALM	Photoactivated Localization Microscopy
PAINT	Point Accumulation for Imaging in Nanoscale Topography
PH	Pinhole
PMF	Polarisation Maintaining Fibre
PMT	Photon Multiplier Tube
PSF	Point Spread Function
RESLOFT	Reversible Saturable Optical Linear Fluorescence Transitions
RM	Resonant Mirror
RPE-1	Retinal Pigmented Epithelial Cells
SIM	Structured Illumination Microscopy
SSIM	Saturated Structured Illumination Microscopy
SLM	Spatial Light Modulator
SMLM	Single Molecule Localisation Microscopy
SNR	Signal-To-Noise Ratio
SPAD	Single-Photon Avalanche Diode
SR	Super-Resolution
SRM	Super-Resolution Microscopy
SR-SIM	Super-Resolution Structured Illumination Microscope
STED	Stimulated Emission Depletion
STORM	Stochastic Optical Reconstruction Microscopy
TDE	Thiodiethanol
TTL	Transistor-Transistor Logic
UoD	University of Dundee

Chapter 1

Introduction

1.1 Fluorescence microscopy

Since the invention of the microscope people have been in a continuous search for better ways to image objects at higher resolution and especially at a higher contrast. Due to the very sophisticated design of human eye, it is the contrast that helps us perceive details more clearly. With little or no contrast between two objects it is almost impossible to tell them apart. Chameleons use low contrast between colour and pattern on their bodies to hide in plain sight. That is why over the years, people have looked for new ways to improve contrast in microscopy images. The most widely used methods that help increase contrast in images are dark field [1], phase contrast [2], [3], interference contrast [2] and differential interference contrast [4]. Nowadays, the technique of choice in the life sciences is fluorescence microscopy due to its specificity and ease of use. During a cloudless night, in a place far away from the city lights, we can see a sky full of stars. This is because the background is very dark and the only light that is reaching our eye is the light coming from the stars. This is a very simplified analogy to how fluorescence images are acquired.

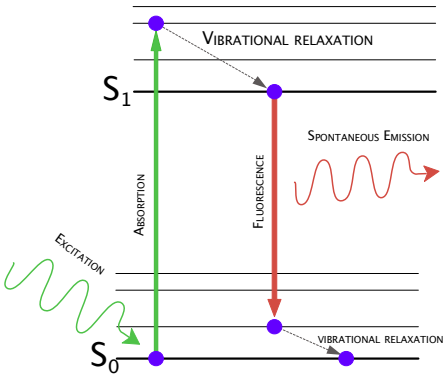

FIGURE 1.1: Jabłoński diagram visualising the process of fluorescence.

In a fluorescence microscope, the object under investigation needs to be labelled with special markers, such as fluorescent dyes, that absorb light with a particular wavelength. When a fluorescent molecule absorbs a photon of light, it changes its

electronic state and moves from the ground state S_0 to an excited state S_1, due to the excess of the energy. Then, while the molecule is relaxing (i.e. going back from S_1 to S_0), it dumps the excess energy in the form of a fluorescent photon, with longer wavelength than the exciting photon. This process, shown in Figure 1.1, was first schematically described by Polish physicist Aleksander Jabłoński [5].

1.1.1 Widefield fluorescent microscope.

Fluorescence is a spontaneous emission phenomena, as it is independent of the number of photons already in the excited state [6]. The emitted, fluorescent photon has a lower energy than the energy of absorbed photon (as some energy is dissipated as heat) and its wavelength is shifted towards a longer value. This is a very important property of the fluorescent light, as due to this, it is possible to distinguish excitation and fluorescent photons. It can be achieved by application of specially designed filters, such as dichroic mirrors, that reflect a particular bandwidth of wavelengths and transmit another bandwidth (Figure 1.2). Then the separated fluorescent photons are imaged by the optical system onto a detector.

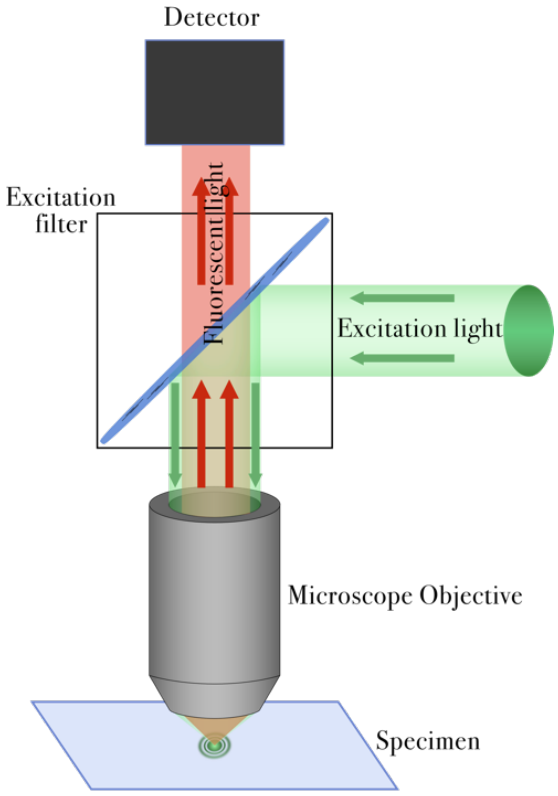

FIGURE 1.2: Schematic of the detection of fluorescence in the fluorescent microscope.

1.1.2 Confocal fluorescent microscope.

The light that excites fluorescent molecules is not only absorbed by molecules located in the in-focus plane, but also in planes behind and in front of it. Due to that, the fluorescent light that is being collected with the detector is "contaminated" with out of focus fluorescent light. This contamination means that the acquired image will be blurred, because of the out of focus light. To overcome this problem a brilliant American mathematician, Marvin Minsky, came up with the idea of blocking the unwanted light with a pinhole. As a result of this idea, the first design of the confocal microscope was proposed [7], [8]. If the pinhole is placed in front of the detector and is conjugated with the focal plane, only fluorescent light originating in the in-focus plane is acquired by the detector. Typical design of the confocal microscope is shown in the Figure 1.3. The confocal microscope is a scanning microscope, which means that the image is captured by scanning the sample point by point and fluorescent photons are detected with the point detector (such as avalanche photodiode (APD) or a photon multiplier tube (PMT), whereas fluorescent detection in widefield microscopy is done by capturing the full image with the CCD or CMOS camera.

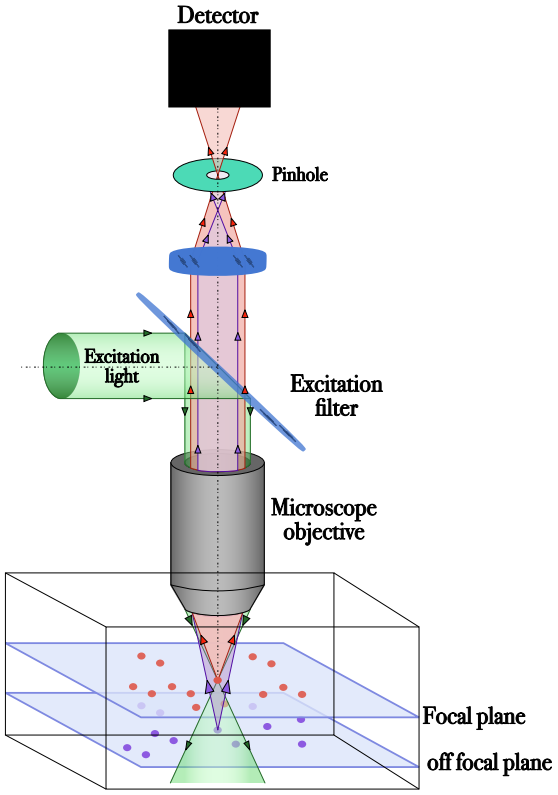

FIGURE 1.3: The concept and optical design of typical confocal microscope.

Thanks to the application of the confocal pinhole, confocal microscope has the ability to carry out layer by layer acquisition (optical sectioning), which leads to improved contrast and axial resolution (by approximately factor of $\sqrt{2}$) of acquired 3D stacks of the imaged sample [9]. A comparison of the images acquired using a widefield microscope and confocal is shown in Figure 1.4.

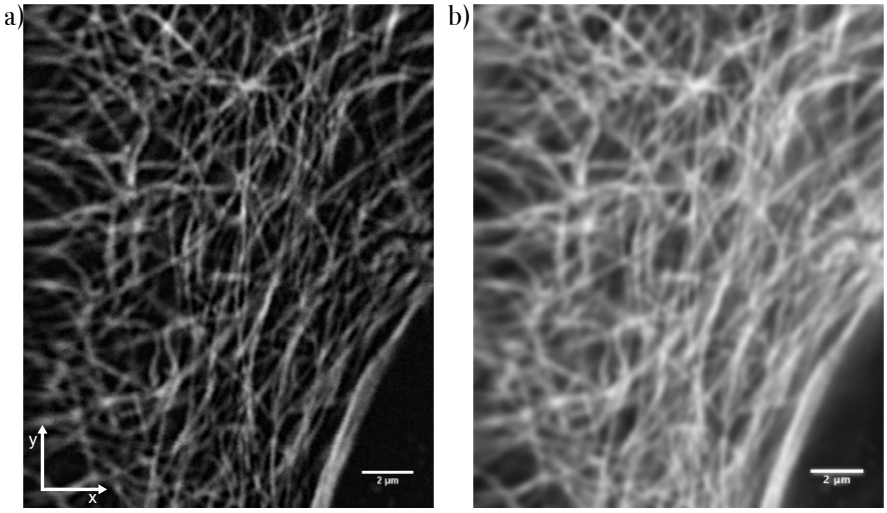

FIGURE 1.4: A comparison between fluorescent images acquired using confocal microscope (a) and widefield microscope (b). Images show the microtubules of HeLa cell. Confocal image provides much clearer and detailed image thanks to the removal of the blurring out of focus light. Scale bar in both images is 2µm.

Unfortunately, the advantages of the confocal microscope come with some practical downsides. Image acquisition is much longer and the power of the excitation light is much higher, as the laser beam is focused into a spot. This leads to photobleaching and lower imaging rate of the confocal microscope compared to the classical widefield fluorescence microscope. Both widefield and confocal fluorescence microscopes are breakthrough inventions and scientists have relied on them for decades. Thanks to them, new possibilities in imaging appeared. However, for a very long time there was an insurmountable challenge: all classical microscopy techniques are limited in spatial resolution due to the effects of diffraction and the limited size of optics. This means that a microscope will not be able to resolve two objects if the distance separating them is smaller than:

$$d = \frac{1.22\lambda}{NA} \tag{1.1}$$

where λ is the wavelength and NA is the numerical aperture of the objective lens:

$$NA = nsin\alpha_{max} = n\frac{D}{2f} \tag{1.2}$$

where n is a refractive index, α_{max} is the maximum angle at which the lens can collect the incident light, D is the diameter of the lens aperture and f is the focal length of the lens. Equation 1.1 is the Rayleigh criterion which will be described in more detail further in this chapter.

1.2 Physical image formation

Equation 1.1 is called the Rayleigh limit and theory behind it was described by Ernst Abbe in 1873 [10]. He was the first person, to give a comprehensive description of image formation. He explained the process of partially coherent optical imaging: light is diffracted at the object and an image is formed by interference. A graphical interpretation of image formation described by Abbe is shown in Figure 1.5 [11]. When the light illuminates the grating-like object, it is diffracted and forms a diffraction pattern in the pupil plane of the objective. Each of the spots in the pupil plane can be treated as point source of the new spherical wave. When those spherical waves interfere in the imaging plane they form the image of the grating placed in the object plane.

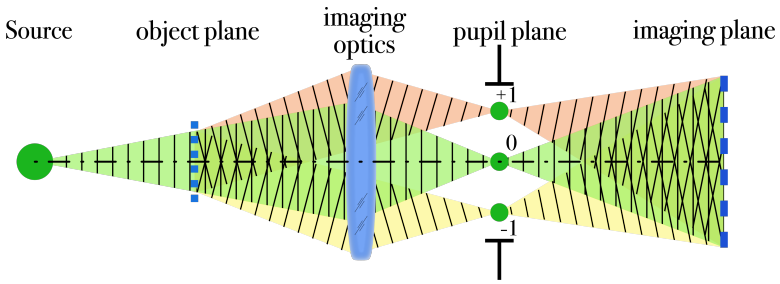

FIGURE 1.5: Graphical representation of Abbe Theory of image formation. [11]

During his considerations about image formation, Abbe discovered that the diffraction pattern is formed at the back focal plane of the microscope objective. If we consider an imaging system, such as 4f system (Figure 1.6), place a grating object in the object plane and illuminate it with a planar wave, we will observe the diffraction pattern of the grating in the back focal plane. The second lens converts the spectrum spots into planar waves, which then interfere in the imaging plane forming a copy of the object. This example clearly explains the effect of diffraction and interference in the process of image formation. Unfortunately, the size of the aperture and incident beam angle α_i defines the number of diffraction orders that pass through the back focal plane. As a result, not all spatial frequencies can be transferred through the optical system. Let us assume that the imaged grating object has the period d and it

is within the same order as the illuminating beam wavelength. The spatial position x_i in the pupil plane of the diffraction orders can be defined as (for the incident beam parallel to the optical axis):

$$x_i = f_1 sin\alpha_n \tag{1.3}$$

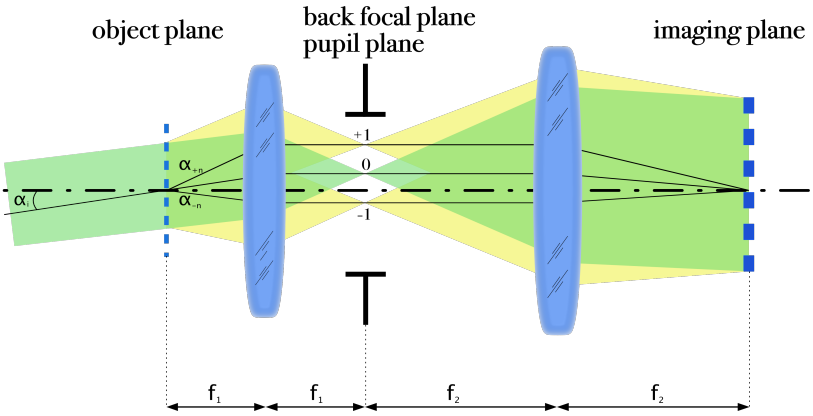

FIGURE 1.6: Typical 4f imaging system, showing the role of the diffraction and interference in the image formation [11].

We will only observe the diffracted wavefronts at the angles α_n fulfilling the Bragg condition, where the interference behind the grating is constructive:

$$dsin\alpha_n = n\lambda \tag{1.4}$$

where n is an integer corresponding to the diffraction order. Putting Equation 1.3 into the Equation 1.4 we get:

$$x_i = \frac{\lambda f}{d} \tag{1.5}$$

The lateral location of the diffraction orders depends on the period of the grating d and illuminating beam wavelength λ. The finer the grating, the further from the optical axis the diffraction order will focus. Similarly, increasing wavelength has the same effect as using a finer grating. Because lenses have a limited aperture size, for very fine gratings, high spatial frequencies that have their foci location outside of the aperture will be lost, as the second lens will not be able to capture them. We can define a minimum object period that will be resolved by the imaging system:

$$d_{min} < \frac{\lambda}{n\ sin\alpha_{max}} = \frac{\lambda}{NA} \tag{1.6}$$

where n is a refractive index. The aforementioned considerations are valid for illumination parallel to the optical axis. For oblique illumination, the resolution can be increased by the factor of two for angles of incidence defined as following [11]:

$$d_{min} = \frac{\lambda}{NA + n\ sin\alpha_i} \tag{1.7}$$

where α_i is an incident angle on the grating as in Figure 1.6.

Using a grating as an object is a good explanation for resolution limitation of imaging through the lens. Let's now replace the grating with a point object. Figure 1.7 illustrates the imaging of a point object.

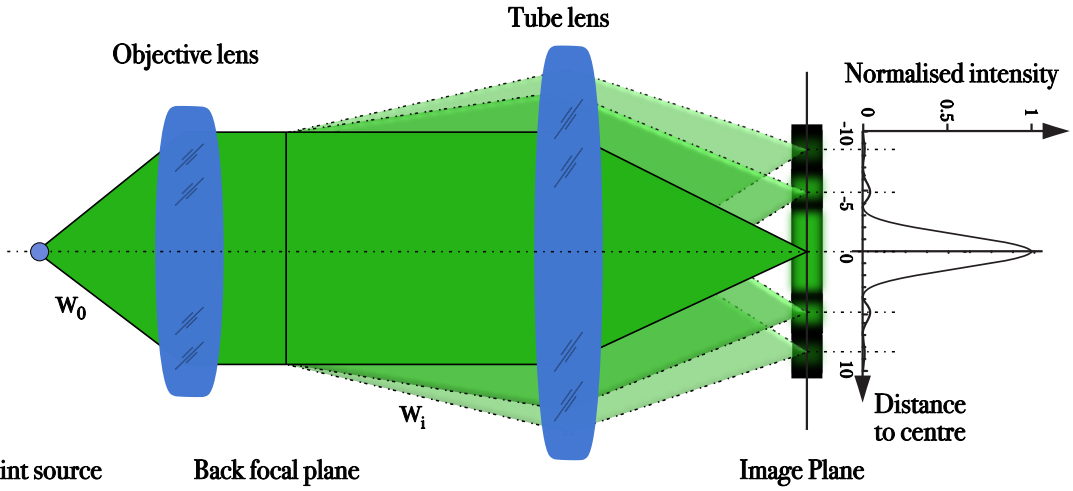

FIGURE 1.7: Imaging of the point object by the optical system [12].

Incident light is emitted by the object into a spherical wave w_0. A tube lens transforms the spherical wave into the planar wavefront w_i. The wavefront w_i has a constant amplitude which is equivalent to the diffraction image of the point object. Due to the limited size of the aperture of the objective lens, not all spatial frequencies of w_0 pass through it, hence the wavefront is disrupted. According to the Huygens-Fresnel principle, each point at the wavefront w_i is a point source of a new spherical wavelet. A tube lens focuses all the wavelets into a point, where they interfere with each other constructively, as they possess the same phase and at the foci the optical path difference (OPD) between all the wavelets is zero. The foci in the image plane will have a finite size because of the aperture size limitations, as the lenses pass a finite number of wavelets. A dark ring around the foci is created by destructive interference. Around the dark ring, a bright ring is formed, as in this area majority of the wavelets interfere constructively. Again, we can observe another dark ring followed by the bright ring. This pattern, formed as a result of constructive and

destructive interference, is called an Airy disk [13], [14]. The cross-section of an Airy disk is shown on the graph in Figure 1.7. The Airy disk can also be described as a result of diffraction at the circular aperture [15]. A circular aperture has a rotational symmetry, hence the image of the point object will have such symmetry as well. We can describe the transmittance h of a circular aperture with diameter d using cylindrical coordinates (ρ, Θ), for $\Theta = 0$ [11]:

$$h(\rho) = circ\left[\frac{\rho}{NA/\lambda}\right] \tag{1.8}$$

For the homogeneous illumination of the circular aperture, the aperture function can be written as:

$$h(\rho) = \begin{cases} 1 & \rho \leq l \\ 0 & \rho > l \end{cases} \tag{1.9}$$

The amplitude distribution of the aperture function $h(\rho)$ is defined by the Fourier transform:

$$H(r) = 2\pi \int_{\rho} h_{\rho}(\rho) \cdot J_0(2\pi r\rho)\rho d\rho \tag{1.10}$$

where J_0 is a Bessel function of the first kind and zeroth order. For the circular function defined as in equation 1.9, equation 1.10 can be written as:

$$H(r) = \frac{NA}{r\lambda} J_1\left(2\pi r \cdot \frac{NA}{\lambda}\right) \tag{1.11}$$

where J_1 is a Bessel function of the first kind and first order. The intensity distribution at the focal plane of the imaged circular object can be described as a following expression:

$$I(r) = |H(r)|^2 = I_0\left(\frac{J_1(2\pi rNA/\lambda)}{2\pi rNA/\lambda}\right) \tag{1.12}$$

where I_0 is the intensity at the focus of the lens. The intensity distribution shown in equation 1.12 describes an Airy disc. The first zero for the $J_1(r)$ function can be found for $r = 3.83$ and this is where the first dark ring of an Airy disk can be observed (Figure 1.8). It can be found at:

$$r_0 = \frac{d}{2} = \frac{0.611\lambda}{NA} \tag{1.13}$$

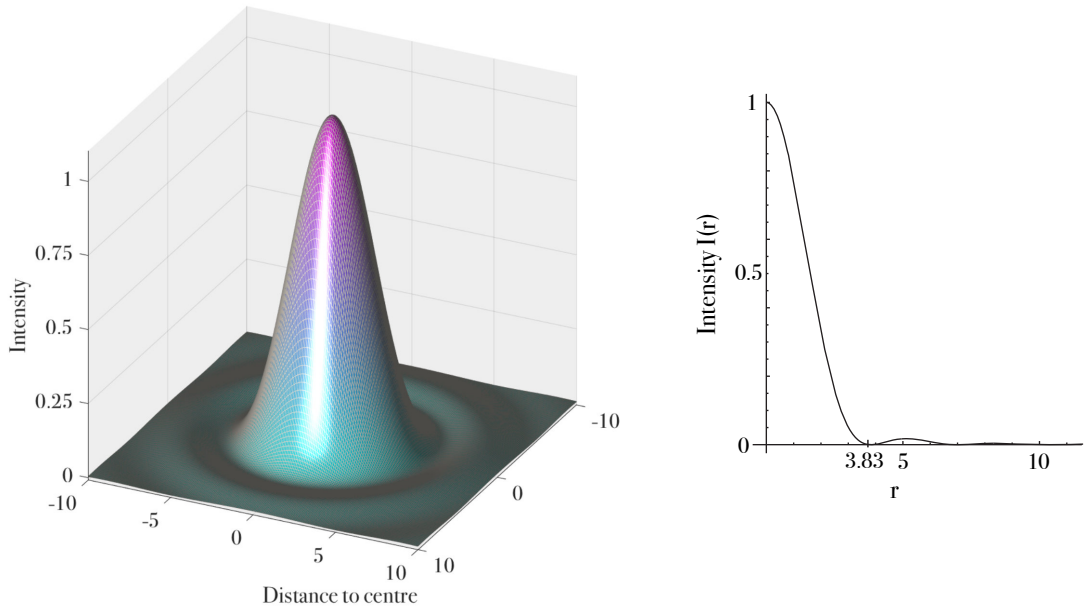

FIGURE 1.8: 3D representation of an intensity $I(r)$ of the point imaged by the imaging system (left) and its cross-section (right). Both plots are shown as a function of the distance r to the centre of the optical axis.

It is worth noting, that the intensity distribution of the point object imaged through the lens is the same as the intensity distribution in the image plane of the lens illuminated with the plane wave. The intensity distribution of a planar illumination of the BFP in the image plane of a lens is called the Point Spread Function (PSF).

1.2.1 Resolution limit.

The aforementioned image formation can be generally formulated as follows. In the 4f system, as shown in Figure 1.7, the objective lens creates a set of spatial frequencies in its back focal plane through the Fourier transform of an object $\mathbb{F}\{A(x,y)\}$. Due to diffraction and NA limitations, not all spatial frequencies can be collected by the objective lens, hence frequencies higher than the limiting frequency are lost. The lens carries out an inverse Fourier transform of the back focal plane creating the image of an object, without the details lost due to the aperture limitations and lost frequencies. This can be described as an imaging system impulse response to a point object or a point source, which is a more general term for the PSF. The Fourier transform of the PSF in the back focal plane of an objective lens is called the optical transfer function (OTF), which is the function describing the ability to collect a finite number of spatial frequencies (limited by the NA) by the objective lens. It means,

that the number of spatial frequencies of the imaged object $A(x,y)$ collected by the lens are defined by the OTF, using the following equation:

$$\mathbb{F}'\{A\} = \mathbb{F}\{A\} \cdot OTF \tag{1.14}$$

where $\mathbb{F}'\{A\}$ is the image of an object A obtained by the optical system defined by the OTF. In Fourier theory, multiplication in the frequency space is equivalent to the convolution operation in the object space. Having that in mind, equation 1.14 can be rewritten as:

$$A'(x,y) = A(x,y) \otimes PSF(x,y) \tag{1.15}$$

The graphical interpretation of equation 1.15 is show in in Figure 1.9.

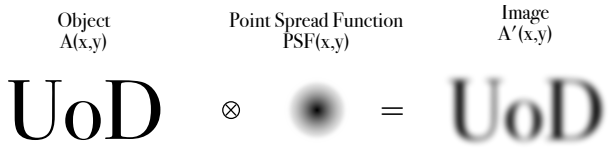

FIGURE 1.9: Graphical interpretation of image formation through convolution.

From equation 1.15 it is easy to deduce that any imaging optical system performance is determined by the PSF of the imaging optics. In fluorescent microscopy, two single fluorescent molecules can only be distinguished when they are separated by the distance larger than r_0 (equation 1.13). This is because it will not be possible to tell whether the image shows one or more single molecules, as the Airy disks in the image plane will overlap each other. This distance is called Rayleigh criterion of resolution [16], [17]. Possible cases of imaging two single incoherent points are shown in the Figure 1.10.

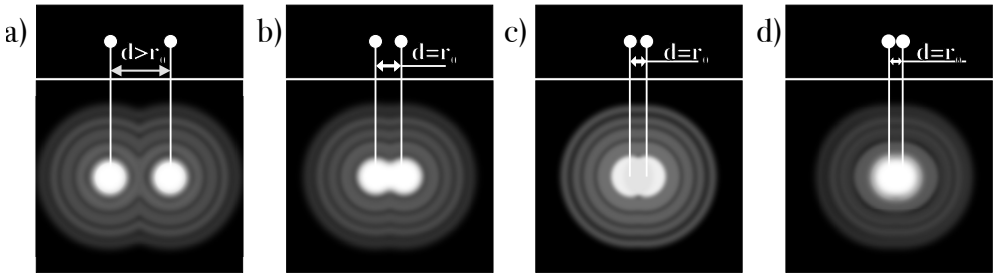

FIGURE 1.10: Intensity distribution of the two light sources in the image plane. The images show the cases, when the distance d between two points is: a) larger than Rayleigh criterion, b) equal to Rayleigh criterion, c) equal to the full width at half maximum (FWHM) of the PSF, d) smaller than $r_0/10$ (equation 1.13), when two points look like a single point and are impossible to distinguish.

For the Rayleigh criterion, two single points are resolved, when the intensity between two maxima of the imaged objects is at 74% of their maximum intensity. This is a distance at which the human eye can still separate two single points. The distance that allows to resolve two single points decreases with the decrease of the imaging wavelength or increase of the NA of the objective lens (Equation 1.13).

Image formation and light distribution is a 3D process. The light not only interferes in the image plane, but also in the space before and after it. The whole intensity distribution, similarly to the image formation described for the 2D process, creates a 3D PSF of an imaging system. The complete 3D light intensity distribution can be calculated using the paraxial approximation theory and has been comprehensively described by Born & Wolf in [18]. A graphical representation of the 3D intensity distribution in the PSF is shown in Figure 1.11. It is worth noting, that for high NA lenses the paraxial approximation is not fully valid, as it does not take into account the vectorial properties (such as polarisation) of the propagating beam. More accurate approximation of the 3D intensity distribution for confocal imaging through high NA lenses has been given by van der Voort and Brakenhoff [19]. However, the paraxial approximation is good enough for the graphical representation of the 3D PSF.

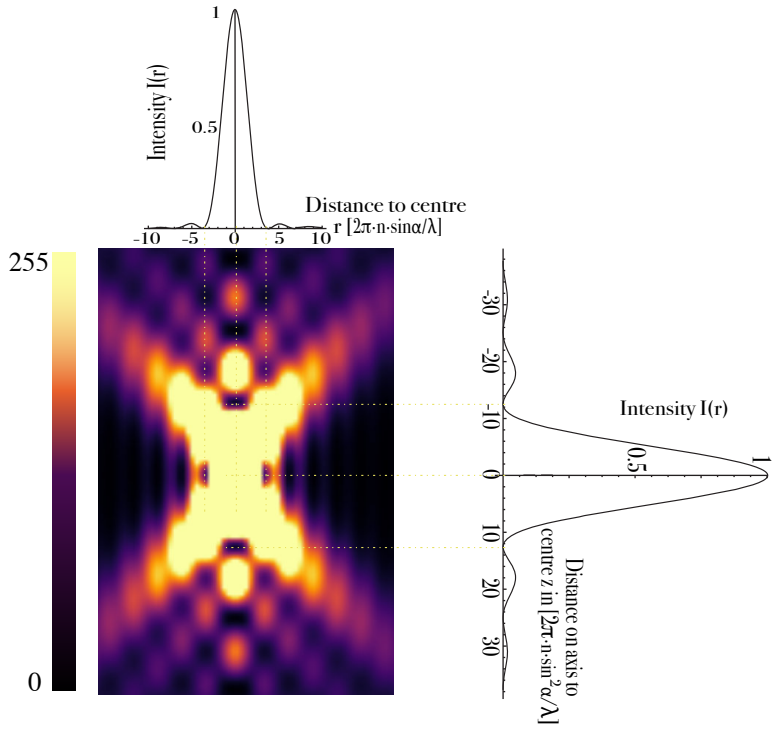

FIGURE 1.11: 3D Intensity distribution in the PSF according to the Born & Wolf paraxial approximation [12].

Axial resolution limit that can be formulated in analogy to equation 1.13 can be written as [11]:

$$z_0 = \frac{2\lambda}{n \cdot sin^2\alpha} \tag{1.16}$$

As shown in both lateral (equation 1.13) and axial resolution (equation 1.16) equations, the resolution of the optical system is proportional to the wavelength used for imaging and is inversely proportional to the NA. Graphs shown in Figure 1.12 show the relation between resolution, wavelength and NA.

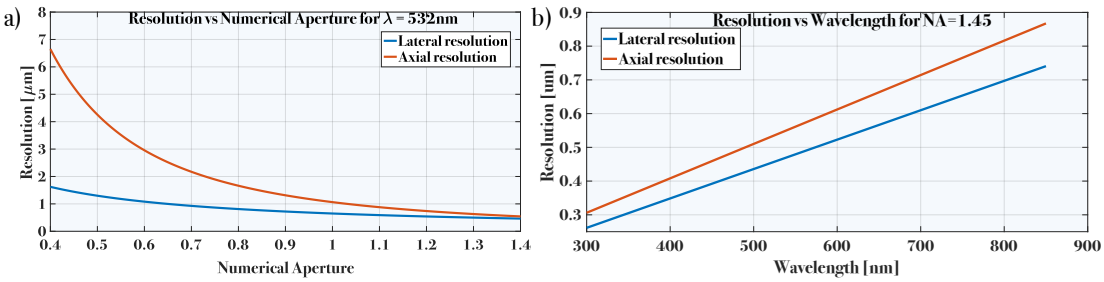

FIGURE 1.12: Plots showing the relation between resolution and a) wavelength; b)numerical aperture.

1.3 Imaging beyond resolution limit

Even though confocal microscopes are great inventions and they helped uncover a huge amount of new biological structures and processes, there is still a lot to unveil and discover, especially in the world of nanoscopic objects, which imaging is limited by the diffraction barrier. As Richard Feynman said in one of his lectures at the American Physical Society meeting "There's plenty of room in the bottom" [20]. Scientists have been working hard for decades to bring tools for sharper and more detailed imaging. Particularly in the world of life sciences, imaging is critical for understanding biological structures and processes. Classical microscopes that utilise visible light for imaging are unable to resolve structures smaller than approximately 200nm. Quoting again Mr. Feynman, "Make the microscope one hundred times more powerful and many problems of biology would be made very much easier" [20]. This highlights the great demand for the tools that would enable scientists see more than they could with currently available devices. In the 1950s, the problem of resolution limit have been tackled by the means of engineering and linear system analysis [15], [21], [22]. Authors of these techniques claimed that increasing brightness could lead to improvement in resolution beyond the diffraction limit. For that reason, those

techniques have been called "super-resolution" [23]. However, the super-resolution was only presented as a principle, it was never used practically for imaging of real world objects. A well known and established tool for imaging with the resolution much greater than the diffraction limit for the visible light is electron microscopy. Following the work of Louis de Broglie, electrons can be treated as waves with a wavelength much shorter than visible light photons. Using electric and magnetic lenses, electron beams can be focused just like regular light sources and thus can be used for detecting contrast and imaging. That led to the construction of the Electron Microscope (EM)[24]–[26]. EM enabled scientists to look deep into nanoscopic structures. Thanks to EM, the discovery of chromatin nanostrucure was possible [27], [28], full volume 3D image of the fly brain providing the complete connectome of learning and memory centre has been imaged [29], [30], even atomic resolution has been achieved [31]. Unfortunately, EM's great downside is that it is challenging to label and distinguish desired structures inside cells. What is more, EM requires samples to be imaged inside the vacuum or under low pressure and samples to be fixed, dehydrated and very thinly sliced, as electrons are unable to penetrate deep into the sample. Sample preparation for the EM gives rise to an ambiguity when analysing images, as it can lead to the specimen shrinkage and modification of tissue structure [32].

The aforementioned problems show the undeniable advantages of fluorescence microscopy: much simpler and straightforward sample preparation, possibility of live cell imaging and high specificity of the imaged structures. This is why biologists reach for the fluorescent microscope much more often. For a very long time there was a great demand for enabling nanoscopic imaging using fluorescent microscopy to bridge the gap between EM and optical microscopy. The breakthrough was achieved with the first super-resolution concept of stimulated emission depletion (STED) microscopy presented by Stefan Hell in 1994 [33]. Since that breakthrough, multiple other super-resolution techniques have emerged: molecule localisation techniques such as photoactivated localization microscopy (PALM) [34], [35] and fluorescence photoactivation localization microscopy fPALM[36], [37], stochastic optical reconstruction microscopy (STORM) [38], [39] and direct STORM (dSTORM) [40], [41]; STED related reversible saturable optical fluorescence transitions microscopy (RESOLFT) [42] and ground state depletion microscopy followed by individual molecule return (GSDIM) [43]–[45]; structured illumination microscopy (SIM) [46] and non-linear saturated SIM (SSIM) [47]. In 2014 the Nobel Prize committee appreciated the efforts made in pursuit for higher resolution and awarded Stephan

Hell, Eric Betzig and William E. Moerner with the Nobel Prize in Chemistry for the development of super-resolved fluorescence microscopy [48]–[50]. Notably, the Nobel prize for SRM was awarded in chemistry , as the SR techniques extract chemical properties of the fluorescence in order to achieve imaging beyond the diffraction limit.

1.3.1 General super-resolution techniques overview

Figure 1.13 shows the comparison of the available super-resolution techniques and Figure 1.14 presents the main properties of most common fluorescent microscopy techniques.

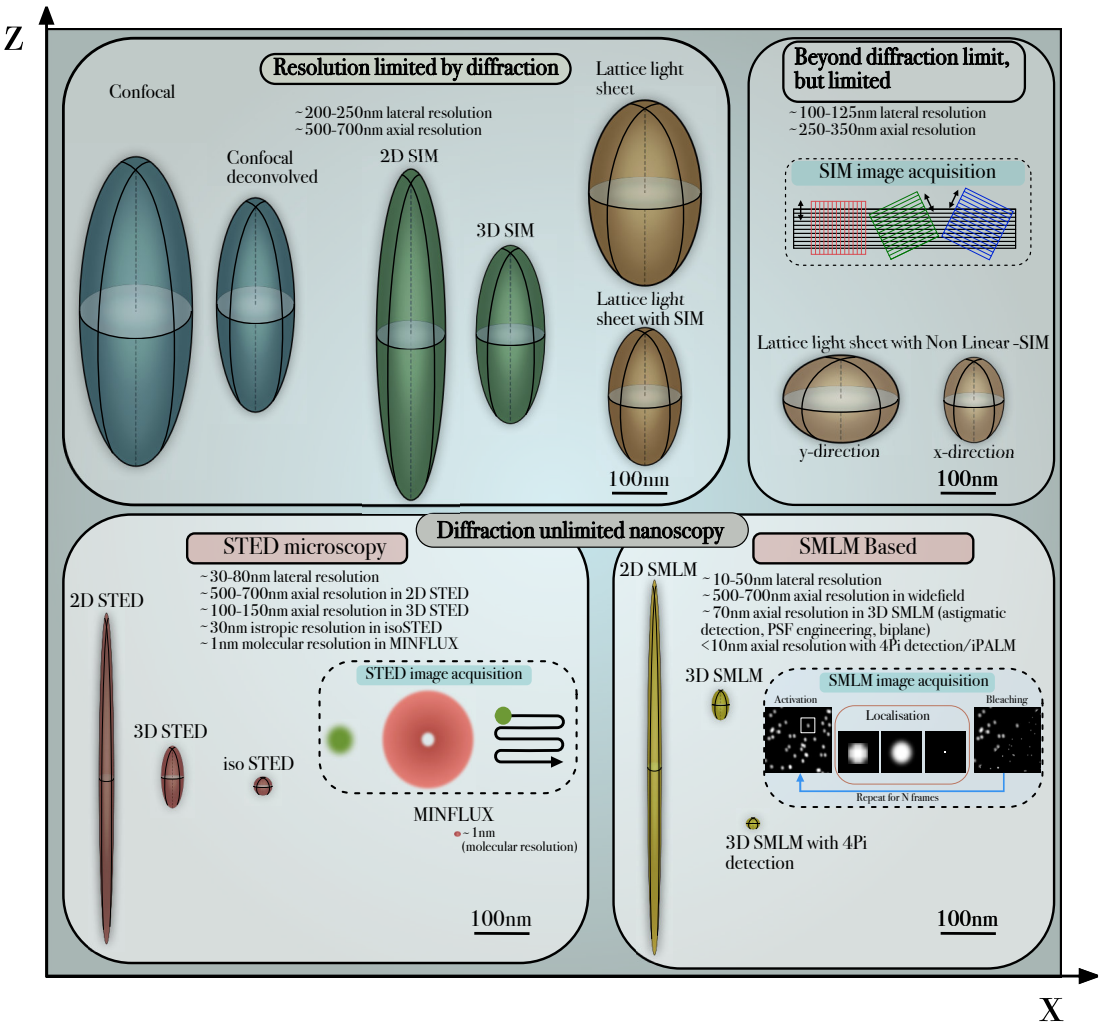

FIGURE 1.13: Comparison between the capabilities, performance and principle of common super-resolution fluorescent microscopy techniques [51], [52].

Each of the techniques utilises different methods of achieving sub-diffraction resolution. SIM and PALM/STORM techniques are based on widefield microscopy while STED principle is laser scanning confocal microscopy. Another common characteristics of SIM and PALM/STORM is that both of these techniques require post processing and reconstruction of the image, while STED microscopy is a purely optical method. All of the super-resolution techniques have been successfully implemented, commercialised and can be easily bought (although the price is very high) from either major microscope producing companies (e.g. Leica, Zeiss, Nikon) or from smaller companies providing super-resolution solutions (Abberior, PicoQuant).

Microscopy technique	Lateral resolution	Axial resolution	Temporal resolution	Imaging depth	Cost	Signal-to-noise	Usability	Phototoxicity
Widefield	Diffraction limited	Usually >1µm	Best, msec/frame, signal limited	Worst	£	High	Simple	Very low (Watts over large FOV)
CLSM	Up to 2-fold increase over diffraction limit (»120nm) with Airyscan	Up to 2-fold increase over diffraction limit (»350nm) with Airyscan	Scanner dependant (1-30 fps)	Up to 100µm	££	Moderate	Very versatile, but complex	Potentially high (as all power is focused into the single spot)
Two-Photon	Diffraction limited	Diffraction limited	Scanner dependant (1-30 fps)	Best (hundreds of µm	£3-£7	Moderate	Complex	Potentially high (as all power is focused into the single spot)
SIM	Diffraction limited	Diffraction limited	1-10 fps	<30µm	£ - ££	Moderate	Simple	Low (depends on the required number of images)
NL-SIM	Up to 2-fold increase over diffraction limit	Up to 2-fold increase over diffraction limit	Good, up to msec/frame with iSIM, signal limited	Up to 50µm with iSIM	£4-£9	Moderate	Simple	Usually low
STED	Super-resolution (typically 30-70nm)	Diffraction limited with 2D STED, up to 100nm with the 3D STED phase mask, 30nm for isoSTED	Scanner dependant (1-30 fps)	Phase mask dependant, <50µm for 2D STED, <15µm for 3D STED	£6-£10	Complex	Low	Poor (very high STED beam power focused into a spot)
SMLM	Super-resolution (10-50nm)	Same as widefield or up to 70nm with 3D SMLM	Poor (require thousandth of images)	Usually less than few µm	£3-£4	Complex (requires post processing)	Low	Varies with the technique, depends on the required number of images
Light Sheet	Diffraction limited	Diffraction limited (but less than in widefield)	Best for 3D imaging, msec/frame	Hundreds of µm	£2-£6	Moderate	High	Low, best technique for 3D or 4D imaging
Lattice Light Sheet with NL-SIM	Up to 2-fold increase over diffraction limit	Up to 2-fold increase over diffraction limit	Best for 3D imaging, msec/frame	Typically 20µm	£2-£6	Complex	Moderate	Low, best technique for 3D or 4D imaging

FIGURE 1.14: Comparison of the parameters and characteristics of most common available fluorescent microscopes. A single pound sign indicates the cost of the state of the art widefield microscope (being in the range of £55k-£80k); number of pound signs refers to the multiplication of the price tag of the widefield microscope. [53], [54].

1.3.2 Single molecule localisation microscopy.

The principle behind obtaining super-resolution images in single molecule localisation microscopy (SMLM) is that the spatial location of the single fluorophore can be determined with the much higher accuracy than the width of the PSF of imaging system. When the number of simultaneously emitting molecules is reduced, they can be temporarily separated by acquiring a number of images with each of the molecules captured within its "on" and "off" state. When each of the emitting molecules is imaged individually, it is possible to determine its position with precision much higher than the diffraction limit by finding the location of the centre of the molecule [55], [56]. After acquiring the required number of images and knowing precise position of each of the emitting molecules, the positions of all molecules are superimposed creating the super-resolution reconstruction of the previously acquired stack. The localisation precision of finding the molecule is inversely proportional to the square root of the number of photons N detected from the emitter [55]:

$$\Delta = \frac{d_0}{\sqrt{N}} \tag{1.17}$$

where d_0 is the resolution of the used widefield microscope. If the fluorescent molecule was bright enough, localisation precision below 1nm could be achieved. Equation 1.17 can also be used as a measure of resolution of the SMLM, as it describes the closest resolvable separation between objects [57]. Figure 1.15 shows graphical process of how SMLM images are obtained.

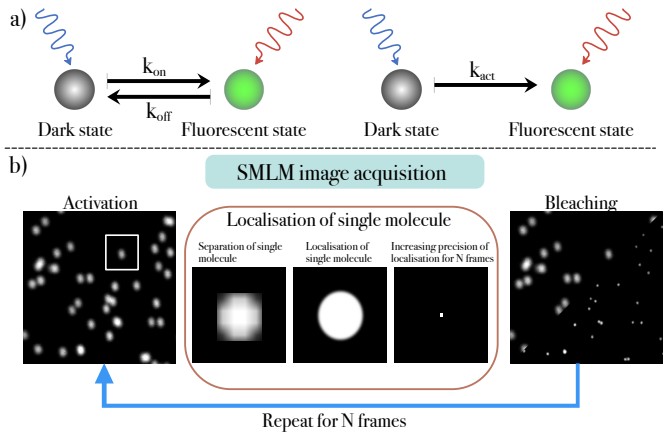

FIGURE 1.15: Schematic of the process of super-resolution image acquisition using SMLM. a) Changing between "on" and "off" state of the molecule, b) acquisition series of images with molecules being stochastically turned "on" and "off" and super-resolution image reconstruction

In order to drive the on/off states of the emitting molecules, fluorescent molecules are required to have specific properties. PALM and STORM techniques share the same principle of operation, however they differ in the type of fluorophore used for obtaining "blinking" of molecules. PALM uses photoactivatable fluorescent proteins such as paGFP [58], while STORM is based on techniques that take advantage of photoswitchable organic fluorophores [40]. The main difference between photoactivation and photoswitching is that photoactivatable fluorescent molecules can be only switched "on" from a non fluorescent state using light with a particular wavelength. Photoswitchable fluorescent molecules on the other hand can be both switched "on" and "off" when they are illuminated with the light with two different wavelengths.

The SMLM techniques have found many admirers and have been modified in many ways. Multiple colour imaging with approximately 20nm resolution have been reported by numerous of groups [35], [39], [59]–[62]. Multiple 3D SMLM have been proposed, such as taking advantage of the astigmatic PSF was shown in [63], shaping PSF into a helix in [64], or using an interferometric approach with impressive axial resolution of 10nm demonstrated in [65]. Even though SMLM imaging can theoretically achieve unlimited lateral resolution with sufficiently bright dyes, labelling density is the limiting factor for obtaining sub 20nm resolution. According to the Nyquist sampling criterion [66], achieving 20nm resolution would require fluorophore binding at least every 10nm which makes it very challenging to get, especially when using the combination of primary and secondary antibodies sample staining [67]–[69]. One of the methods circumventing the problem of insufficient labelling density is a variance of SMLM called PAINT (point accumulation for imaging nanoscale topography). In PAINT, when using oblique illumination, low concentrations of fluorescent molecules are added directly into the medium, so that single molecules can be tracked on the cell surface[53], [58], [70].

1.3.3 Structured illumination microscopy.

According to equation 1.15, an image is a convolution of an object and PSF. As described in the Section 1.2.1, the OTF is a Fourier transform of the PSF:

$$\mathbb{F}\{PSF(x,y)\} = OTF(k_x, k_y) \tag{1.18}$$

If we describe the image formation process as a multiplication in the frequency space, equation 1.15 will look like the following:

$$\mathbb{F}\{A'\} = \mathbb{F}\{A\} \times OTF \tag{1.19}$$

As written before in this chapter, due to the limitations of the NA of the imaging lens, high spatial frequencies are not collected by the imaging system. The highest spatial frequency collected by the lens is called the cut-off frequency $k_{cut-off}$. The OTF for frequencies above $k_{cut-off}$ is zero, so all object features represented by those frequencies will be missing in the image. An OTF can be represented as a toroid that reveals the missing frequencies in the Fourier plane, as shown in Figure 1.16 a) and b).

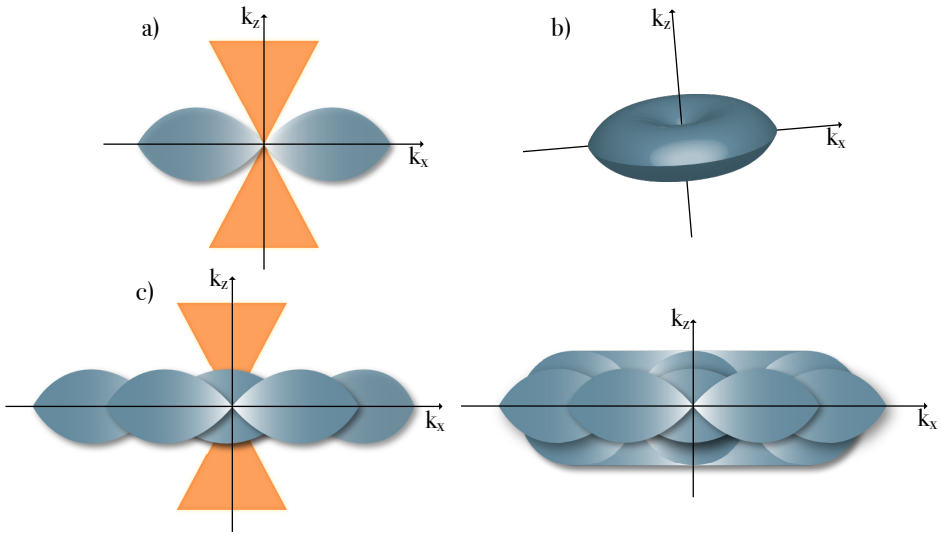

FIGURE 1.16: OTF support comparison of the widefield and SIM microscope. a) shows the conventional OTF volume of typical widefield microscope, viewed along the k_y axis, with the orange "missing cone" representing the missing frequencies along the k_z axis, "missing cone" limits the axial resolution of the optical system; b) shows the 3D interpretation of the aforementioned OTF volume, represented by the toroid; c) shows the OTF support for the case of the 2D SIM, while d) shows OTF support for the case of the 3D SIM [71], [72].

A frequency representation of the use of $k_{cut-off}$ is commonly used as an alternative method of measuring the resolution of an optical system. As shown in the Figure 1.16, for the classical wide-field microscope there is a cone in the centre that is missing, therefore cutting off some of the object features. This missing frequency problem is often defined as a problem of the "missing cone". The purpose of super-resolution techniques is to fill that missing cone with spatial frequencies, so that more features of the object could be imaged. There are two widely implemented uses of SIM: removing the out-of-focus light from the image enabling optical sectioning or increasing the resolution beyond diffraction limit.

Structured illumination microscopy finds the solution to the missing cone. The object is illuminated with a patterned light, e.g. fringe pattern with high spatial frequency. When two periodic structures of high frequencies are superimposed, they produce a downmodulated, low spatial frequency pattern, called moiré fringes [73], as shown in Figure 1.17.

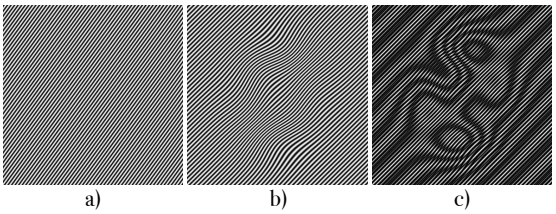

FIGURE 1.17: Moiré pattern generation. When two periodic structures such as a) and b) are superimposed, down-modulated pattern is created, as shown in (c).

When a patterned illumination light is mixed with the structure of the sample a coarse, lower frequency pattern, called a moiré pattern is created. The newly-created pattern, thanks to down-modulation, can be easily resolved by the imaging optics, even though the original structure was too fine to be resolved. This way, high spatial frequency details of the object can be encoded in the much coarser moiré fringes. The illumination pattern is most commonly generated by a physical diffraction grating or a spatial light modulator (SLM). The illuminating pattern is well known *apriori* and the coarse moiré pattern can be collected by the imaging optics. If the moiré pattern is applied in different orientations and different phase shift, it is possible to reconstruct the previously unresolvable information corresponding to the moiré pattern from acquired set of images using numerical reconstruction algorithms. SIM image reconstruction requires recording at least three images with phase shifted moiré pattern in order to obtain a single super-resolved frame.

The SIM principle is based on widefield microscopy. Its first implementation was shown by Nail *et al.* in [74] and was used for optical sectioning, while Gustafsson showed the super-resolution capabilities of SIM [46]. Lateral resolution enhancement by two-fold in SR-SIM over traditional 2D microscopy methods been reported in [46], [75]. Gustafsson *et al.* [71] and Schermelleh *et al.* [76] showed a 3D SIM design, with additional axial resolution increase, where the illumination pattern is created with three beam interference. The classical SIM approach allows only for 2-fold resolution increase in each direction. An impressive combination of image interference imaging microscope (I^5M) [77] with 3D SIM resulted in interferometer-based three-dimensional structured-illumination I^5S microscope with 100nm isotropic resolution [78]. In 2005, Gustafsson [47] presented the

concept of saturated SIM (SSIM), taking advantage of non-linear characteristics of fluorescent dyes enabling the possibility of theoretically unlimited resolution enhancement. For non-linear SIM, a lateral resolution down to 50nm has been reported [47], while Rego et al. [79] were first to achieve 50nm resolution in biological samples. The only resolution limiting factor in non-linear SIM are non-linearities of dyes and the image noise.
There has been a great interest in SIM, as it delivers super-resolution imaging while being gentle to the sample, and images can be acquired with high speed. An especially impressive system has been developed by the Betzig group, combining light sheet microscopy [80], [81] with SIM [82]–[85], enabling video rate, 4D imaging of biological structures.

1.3.4 Stimulated emission depletion microscopy

The concept of stimulated emission depletion microscopy (STED) was first published as a theoretical paper in 1994 [33], however it took half a decade until the first working STED microscope was presented by T. Klar and S. Hell in 1999 [86] and shortly after in 2000 [87]. STED microscopy is based on the confocal laser scanning fluorescence microscopy, allowing the acquisition of images with a resolution well beyond the diffraction limit. The main idea behind STED microscope is that emitted fluorescent photons can be “switched off” by using stimulated emission. When the fluorescent molecules are excited they increase their energetic state and move from the ground state S_{01} to an excited electronic level S_{11}. This is followed by the fast decay to the lowest vibronic excited state S_{12} through phonon assisted transitions (vibrational relaxation). Molecules prefer to stay in the ground state, so they release their energy in the form of fluorescent photons and return from S_{12} to S_{02}. This is a general concept behind any fluorescent microscope. However, the excited molecules at S_{12}, instead of spontaneously emitting energy, can be forced to return to ground electronic S_{03} followed by vibronic transition to S_{01}, by using the stimulated emission. Stimulated emission is a phenomena that is used in order to obtain lasing from the laser. If we illuminate excited molecules we can "turn them off" (deplete them) by forcing them to release their energy in the form of stimulated emission photons. Those photons inherit the properties of the stimulating light, i.e. they will have the same wavelength, phase and polarisation. Both spontaneous emission and stimulated emission processes are shown on the Jabłonski diagram in Figure 1.18.

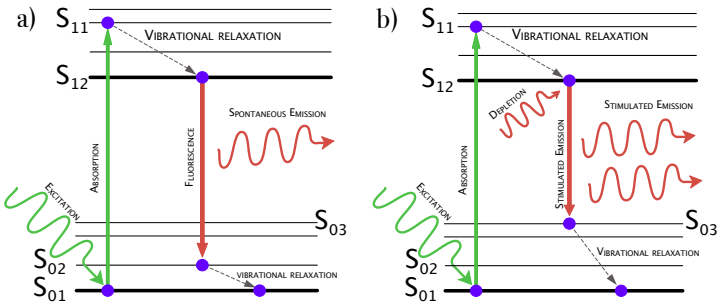

FIGURE 1.18: Jablonski diagram of a) spontaneous emission (fluorescence) and b) stimulated emission.

Now, if the beam used to cause stimulated emission, called depletion beam, is shaped into a Laguerre-Gaussian beam [88], [89] (which lateral intensity distribution resembles a doughnut), with the hole (zero intensity) in the centre and containing all of its energy in the ring, the molecules that appear only in the area of the ring will be depleted. When we take that idea into the confocal microscope and superimpose the Laguerre-Gaussian depletion beam with the excitation beam and scan the sample with such overlapping beam, we will get two sets of photons with different properties: obtained through spontaneous and stimulated emission. Since these photons will have different wavelengths, they can be easily filtered with the bandpass filter and only the molecules in the area of zero-intensity of the depletion beam will be detected by the photon detector. As a result, the sample will effectively be scanned with the PSF of much lower volume compared to the classical CLSM and the final image will have the resolution well beyond than Abbe's resolution limit. The condition that the stimulating photon needs to fulfil is that it has to at least match the energy of the vibronic transition (a phonon assisted transition) of the molecule in the excited state S_{12}. Metaphorically, STED microscopy can be described as painting with a much finer brush, compared to the CLSM. The comparison of the image acquisition between STED and CLSM is shown in Figure 1.19.

In STED microscopy, the volume of the PSF is effectively decreased by confining the region where excited molecules emit fluorescence. The efficiency of depletion and, as a result, resolution of the STED microscope is mainly dependent on the intensity of the depletion beam. According to Westphal and Hell [90], the resolution of a STED microscope can be defined as following:

$$d_{STED} = 0.45 \frac{\lambda}{NA\sqrt{1 + \frac{I_{STED}}{I_{sat}}}} \tag{1.20}$$

where I_{STED} is the intensity if the depletion beam, I_{sat} is the fluorophore specific

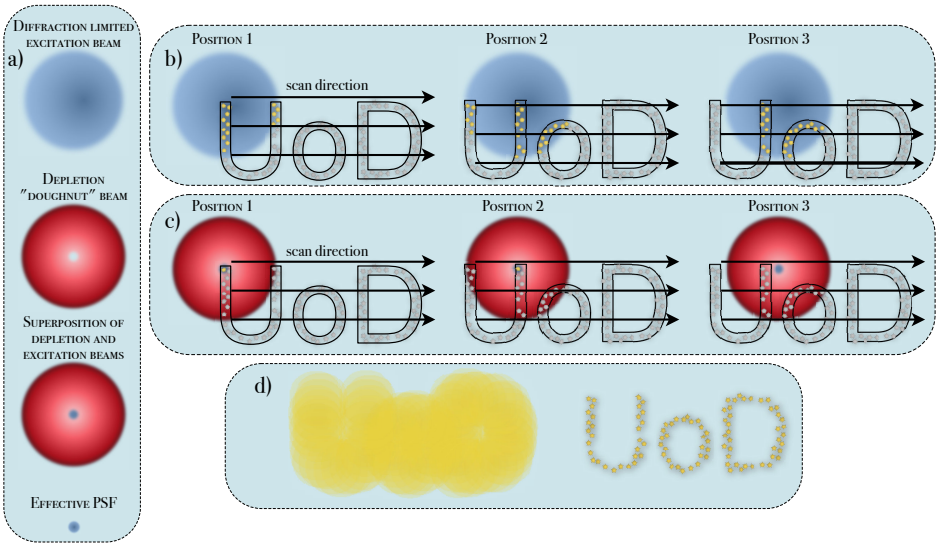

FIGURE 1.19: Graphical principle of STED microscope image acquisition. a) shows the size of the focal spot and the effective STED focal spot when confocal beam is superimposed with the "doughnut" beam. b) represents the scanning of the image with the confocal PSF and the fluorescent molecules it excites, c) is presents the scanning of the image in the STED microscope and effectively excited fluorescent molecules with the combination of depletion and excitation beams, while d) shows the resulting image from the confocal (left) and STED (right) microscope.

saturation intensity, for which the emitted florescence is decreased by the factor of $1/e$. According to Equation 1.20, the higher the intensity of the depletion laser, the higher the resolution that will be achieved. Over the years, it has been reported, that STED microscopy can be used to successfully resolve structures as small as 20nm in biological samples [91], whereas <5nm resolution has been shown for imaging nitrogen vacancy colour centres in nano-diamonds [92].

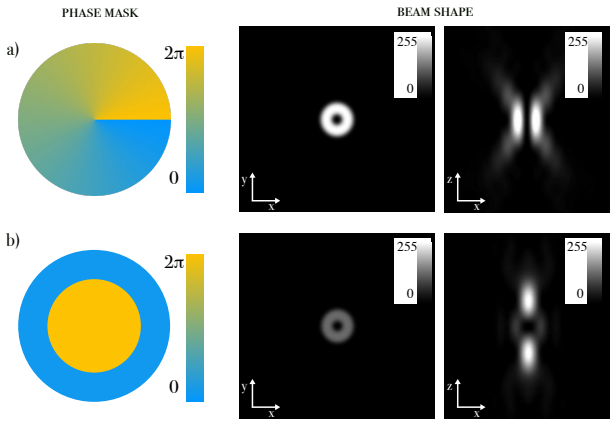

FIGURE 1.20: Phase masks used for (a) 2D STED and (b) 3D STED beam shaping.

Classical STED microscopy enhances the resolution only in the lateral direction,

leaving the axial size of the PSF unmodified. The shape of the depletion beam is obtained by changing its phase. Modification of the wavefront phase changes its shape, as it adds local retardation to the beam which result in the modified shape. This can be done either by a fixed physical phase mask or by using an SLM [93], [94]. The phase mask needed to achieve the doughnut beam is a 2π helical phase mask (as shown in Figure 1.20 a)). Notably, it is possible to modify the shape of the depletion beam by applying the π-step phase mask (Figure 1.20 b)), so that it will be depleting the out-of-focus light, effectively decreasing the size of the PSF in axial direction [87]. The comparison of both a 2D STED phase mask and a 3D STED phase mask is shown in Figure 1.20. Further discussion regarding the phase masks can be found in the section 1.4.4. Resolution up to 45nm laterally and 100nm axially has been reported for the 3D STED with the combination of π-step and 2π helical phase masks [95].

1.3.5 Conclusion and comparison of the currently available super-resolution techniques.

The super-resolution techniques discussed here have been an undeniably huge step forward into the world of nanoscale. In the past 20 years there has been a great interest in developing these techniques into much better tools for biologists. Each of the super-resolution microscopes has found its way into being commercially available. Nowadays, each of the major fluorescent microscope producers must have a super-resolution microscope in their portfolios. However, even though the techniques did help with a plethora of breakthroughs, none of them is perfect. With super-resolution imaging, the sample preparation protocols became more complex and very often device specific, as a lot of the SRM are custom built devices. This requires a long process of optimisation and trials. Reported resolutions, repeatedly spectacular, are obtained for strictly limited conditions and require optimised samples. Another issue is the limited signal-to-noise ratio (SNR) that is present in almost all of the SR techniques. Theoretical resolution limits are very difficult to achieve due to the lack of sufficient signal coming from the sample, mostly due to the photobleaching of the fluorophores [38], [96]. However, probably the most important factor of the limitations of SRM are optical aberrations. They degrade the image quality in classical microscopy [97]–[100], but are even more severe in the SRM [101]. Both optics [97] and specimen introduce aberrations [9], [102]. This is why adaptive optics is being adapted in many SRM, as it allows for aberration correction so crucial in nanoscopic imaging [103]–[105]. Spherical aberration is

one of the greatest enemies of any SRM microscope. It enlarges the PSF laterally and axially as well as decreases the signal coming from the sample [69]. In SIM, spherical aberration degrades the illumination pattern, decreasing resolution and SNR, which can cause artefacts to appear in the reconstructed image [106]. Similarly in STED microscopy, the depletion beam phase mask is very prone to aberrations, as this leads to non uniform intensity in the doughnut as well as increasing the size of the doughnut hole [107]–[109]. Thorough comparison of different fluorescent microscopy techniques can be found in Figures 1.13 and 1.14.

The aim of this work was to build super-resolution 3D STED microscope with the addition of adaptive optics for aberration compensation and use it to image thick samples with both lateral and axial resolution enhancement. Out of the SR techniques, STED and SIM show great promise in 3D imaging of thick samples [110], with STED being able to achieve higher resolution compared to SIM. The following section will be devoted to the detailed description of STED microscopy, the challenges in building the microscope, known problems and possible solutions to them.

1.4 STED Microscopy

STED microscopy is a part of a more generalised concept of reversible saturated optical fluorescence transitions (RESOLFT) [42], [111], [112]. The whole idea of RESOLFT is that some fluorophores can be targeted and optically switched between their "on/off" or bright/dark states. It can be carried out using a depletion laser or reversibly switching fluorescent proteins.
The first theoretical concept regarding STED microscopy was proposed in early 1990s by Hell and Wichmann [33], followed by another RESOLFT concept: ground-state depletion (GSD) fluorescence microscopy, where the diffraction limit is surpassed by the utilisation of transitions of singlet-triplet states as an alternative to STED [113]. In 2003 RESOLFT techniques were described in a common formalism by Stefan Hell in [111]. Over time, multiple implementations of STED microscope had been reported, distinguished mainly by type of depletion laser used for obtaining depletion:

- pulsed STED, with pulsed depletion laser source
- CW-STED, with continuous wave (CW) depletion laser source

1.4.1 Pulsed STED microscopy

The first implementation of a STED microscope shown by Klar and Hell in 1999 [86] and shortly after in 2000 [87] used pulsed lasers for both excitation and depletion. Utilisation of a pulsed laser source for depletion requires precise alignment of excitation and depletion beams both in space and time, as the STED pulse must arrive right after the excitation pulse [114]. First commonly used laser sources for pulsed STED were bulky and expensive Ti:Sapphire lasers [115]–[117]. What is more, Ti:Sapphire laser pulses, in order to optimise the efficiency and timing of stimulated emission, have to be stretched from femtoseconds up to 100-500ps [118]. It has also been proven that longer depletion beam pulses decrease unwanted effects caused by high power of depletion laser such as photobleaching, phototoxicity and direct excitation by the depletion laser (usually through 2-photon excitation) [96], [119], [120]. All this adds complexity and cost to the system. On the other hand, Ti:Sapphire lasers add great flexibility in terms of wavelength tunability, as different fluorescent molecules may require different depletion wavelengths. A solution to decrease cost and complexity was the application of diode lasers as depletion laser sources [121], [122]. It has been shown that diode lasers did not sacrifice the achievable spatial resolution, reporting possibility of imaging structures <15nm [91], [92]. Additionally, diode lasers add a great capability of being able to externally trigger the depletion laser, simplifying the temporal alignment process of laser sources [117]. Thanks to the rapid development in the field of STED microscopy, there are commercially available depletion laser sources that are compact, high power and the output pulses are already stretched to 500ps, that reduce complexity of the STED setup and simplifies temporal alignment of laser sources.

1.4.2 CW-STED microscopy

Another approach to STED microscope design, in terms of the depletion laser, was the application of continuous-wave (CW) lasers [123]–[126]. CW lasers significantly simplify the STED microscope setup, as they do not require laser pulse preparation and synchronisation. However, the performance of a CW-STED microscope is inferior when compared to the pulsed STED solutions [119]. As shown in Equation 1.20, the resolution of a STED microscope depends on the saturation intensity I_{sat}. When CW laser is employed as a depletion laser source, saturation intensity increases by the factor of [123]:

$$I_{sat}^{CW} = \frac{\Gamma}{ln(2) \cdot \tau_{fl}} I_{sat}^{pulsed} \tag{1.21}$$

where Γ is the time between two pulses and τ_{fl} is the fluorescence lifetime of the fluorescent protein. Hence, according to Equation 1.21, in order to achieve the same resolution in CW-STED as in pulsed STED, a CW laser requires its average power to be $\frac{\Gamma}{ln(2) \cdot \tau_{fl}}$ times higher than the peak intensity of the pulsed laser. This translates to 3-5 times higher depletion intensities being required with CW lasers [125] using the typical conditions of the STED imaging (depletion laser repetition rate of 80MHz and $\tau_{fl} \approx 3ns$). Furthermore, in the systems utilising CW depletion lasers, some of the fluorescent molecules emit fluorescence before being illuminated with the depletion beam. This causes residual fluorescence still being picked up by the detector resulting in the increased blur in the image [119]. A solution to this problem is the employment of time-gated detection, where the detector acquires fluorescence signal only after a certain time-delay T_g after arrival of excitation pulse. This way we ensure that the fluorescent molecules have populated the excited state and have been exposed to sufficient number of depletion photons for at least the same time. Acquiring the photons with T_g delay after the excitation pulse ensures efficient depletion and increases the final image resolution without the need for increasing the depletion beam power. The downside of the time-gating is the reduction of the detected signal that is forming the image [127]–[129].

1.4.3 Photobleaching and strategies to its minimisation

Photobleaching is one the major problems of STED systems, due to very high power of depletion laser and longer dwell times compared to the widefield or confocal imaging. When the fluorescent molecules absorb excitation beam photons and change their energetic state, high laser intensities very often might introduce phototoxicity through elevated heating or photobleaching [118]. Even though, theoretically, depletion light should not be absorbed by the fluorescent molecules, it might cause direct excitation or 2-photon excitation. This employs as a primary cause of photobleaching in the STED microscopy [116], [130], [131]. As mentioned already, apart from using longer depletion laser pulses, another method of reducing photobleaching is utilisation of fast laser scanning system, such as resonant mirror [9], [124], [132], [133]. Fast scanning can successfully reduce the population of triplet states, which play a crucial role in photobleaching [134], [135]. The similar effect can be achieved by decreasing the laser pulse repetition rate [116], [136]

which enables relaxation of molecules before the arrival of the next STED pulse and, as a result, a reduction of the population of triplet states. It is also worth noting, that careful choice of depletion laser wavelength and fluorescent molecules can decrease the photobleaching rate in the sample, minimising the excited state absorption [131], [137].

1.4.4 Depletion beam shaping and maximising STED efficiency

Shaping the depletion beam is a vital part of a STED microscope. The first systems utilised glass, polarisation dependent, phase plates, such as classical, vortex phase plates, with 2π spiral phase retardance (Figure 1.20 b)), and a "Top Hat", annular phase mask, with a π phase retardance in the central disk of the phase mask (Figure 1.20 b)). Both of these phase masks have a slightly different way of producing STED images: vortex phase masks deplete the fluorophores in the same focal plane as the excitation beam, producing the laterally super resolved image, while the "Top Hat" phase masks deplete the fluorophores before and after the focal plane of the excitation beam, producing axially super resolved images (however it does have some residual lateral ring, which also increases the lateral resolution) [87], [95], [138], [139]. Hence, taking into account their application, these phase masks can be called a 2D STED phase mask and a 3D STED phase mask. All of the classical phase plates will change the phase of both excitation and depletion beams that pass through them, as the phase plates introduce phase retardation to all wavelengths (although the magnitude of the retardation depends on the wavelength). This adds the necessity of separating the excitation and depletion beams, as only the depletion beam must be modified, and the phase plate needs to be placed in the isolated beam path of the depletion laser, increasing the complexity of the system. The solution to that problem was introduction of the birefringent phase plate, that can convert a confocal microscope into a STED microscope by simply placing the phase plate into the back focal plane of the microscope objective [140], [141]. Such a phase plate significantly simplifies the complexity of the STED system and spatial alignment of the depletion and excitation beams, as they can be coupled into a single fibre, resulting in near perfect spatial alignment [140]. Over time, spatial light modulators (SLM) gained the interest of many groups as devices used for depletion beam shaping [94], [142]–[144]. SLMs add flexibility in the choice of the phase mask, but more importantly, can correct for aberrations occurring in the optical setup as well as in the sample [98], [99], [145]. Theoretically, increasing the depletion beam laser power should give the highest resolution. However, in

reality, this might result in damaging or in best case bleaching the sample. Phase mask alignment is crucial in order to obtain correct depletion beam shape, with uniform intensity distribution and a near perfect zero in the central part of the doughnut. Misalignment of the phase mask introduces unwanted aberrations to the depletion beam, breaking the beam shape [146], which has very similar effect as the appearance of aberrations in the depletion beam path [107], [108], [147], [148]. The effect of aberrations and misalignment on the depletion beam shape are shown in the Figure 1.21. Furthermore, apart from allowing for dynamic change of the phase mask, aberration correction, SLM can also help in the alignment of the phase mask making this task automatic [93].

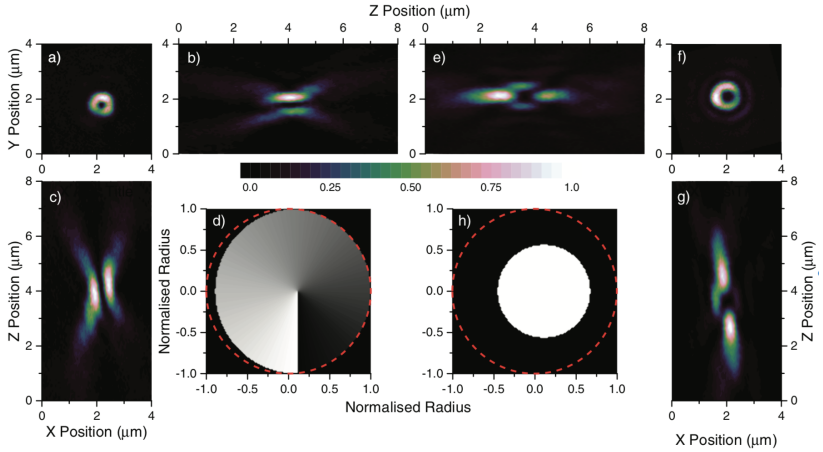

FIGURE 1.21: Importance of the proper alignment of the STED phase masks. a),b) and c) show the 2D STED phase mask (d) in x-y, x-z and y-z planes respectively and the impact of imprecise phase mask alignment on the intensity distribution. Similarly, e), f) and g) show the 3D STED phase mask (h) and intensity distribution with misaligned phase mask in x-z, x-y and y-z planes respectively (image taken from [146]).

Apart from misalignment, polarisation plays a significant role in the shape and intensity distribution in the STED phase mask [108], [149], [150]. In order to obtain a proper intensity distribution in the STED foci, it is important that the circular polarisation in the correct direction is ensured at the BFP of the microscope objective. In case of other polarisation states, the unwanted effects will occur, such as non-zero intensity in the central hole of the Laguerre-Gaussian beam (wrong direction of the circular polarisation) or unequal intensity distribution in the ring (linear or elliptical polarisation)[151]. Both, polarisation and misalignment of the phase mask lead to introduction of residual depletion intensity causing fluorescence quenching also in the central part of the doughnut. Due to this the final STED image will appear

dimmer and with much lower contrast, as the effective STED PSF peak value is reduced.

1.4.5 Thick tissue imaging.

The majority of the publications regarding STED microscopy present super-resolution images that are located in tissue-less, thin samples (<5 μm), close to the coverslip, mostly imaged with the 2D STED phase mask. Much more challenging and interesting, in terms of biological sample imaging, are thick structures located in the tissue that could be resolved with both axial and lateral super-resolution. Urban et. al showed possibility of 2D STED imaging of synapses inside the brain up to 78μm deep, with the use of a glycerol objective with correction collar [110]. Another approach for deep tissue imaging was the combination of STED imaging with 2-photon microscopy [152], enabling imaging at the depth of 30μm inside brain [153]. The main challenge for 3D STED imaging of thick samples is the appearance of aberrations introduced by the specimen. As mentioned in the previous section, aberrations can be compensated with the adaptive optics (AO) such as SLM. There already have been multiple reports, showing 2D STED imaging in aberrating thick samples [142], [154]–[156]. However, 3D STED imaging in the thick aberrating specimens have so far been limited [94], [157], [158], as the 3D STED implementation is even more sensitive to aberrations than its 2D counterpart.

1.4.6 Conclusions and overview of the next chapters

In the introduction chapter I presented the major available techniques used for fluorescent imaging. I compared the three main super-resolution techniques and shown motivation for the STED microscopy as a technique of choice for this thesis. I made a review of the available solutions and designs, that improve the performance of STED microscope and enable imaging of thick samples. The following, Optical methods chapter 2 includes the detailed description of the design of the STED microscope developed for this thesis. Chapter 3 presents the experimental methods used for sample preparation, whereas chapter 4 shows the evaluation of the performance and characterisation of the microscope. Chapter 5 shows the results from imaging of the biological structures. Conclusions of the work done for this thesis and the outlook of the future work and possible further development of the proposed STED microscope are included in the last chapter 6.

Chapter 2

Optical methods

This chapter will be devoted towards detailed description of the microscope. Section 2.1 will contain the explanation of the optical design and purpose of all the elements. Subsections 2.1.1 - 2.1.3 include physical design and description of the main optical beam paths of the microscope: excitation beam path, depletion beam path and imaging beam path. Subsection 2.1.5 has the calculations used for the proper choice of the essential part of every confocal microscope, i.e. pinhole, while subsection 2.1.6 shows the motivation for the selection of the filters allowing for STED imaging. Section 2.2 present the process of the image formation with the resonant mirror laser scanning system I chose, followed by the section 2.3 with the description of the control software written to operate the microscope.

2.1 Design of the STED microscope

Design of the microscope was based on a thorough review of current designs and well proven concepts. Since the most important feature of the microscope was to acquire super-resolution images of thick biological structures, the features of the design sought for were:

- aberration correction of the depletion beam
- thick tissue imaging
- minimisation of photobleaching

The schematic of the designed setup is shown in Figure 2.1 and the photos of the microscope are shown in Figure 2.2. Table A.1 in the Appendix A presents the list of all components that are used in the system. There are three main optical paths in the system: the excitation beam light path starting at the 637nm laser, the depletion beam light path starting at the 766nm depletion laser, and the fluorescent signal light path starting at the sample plane. Each of the light paths will be described in detail in the following sub-chapters.

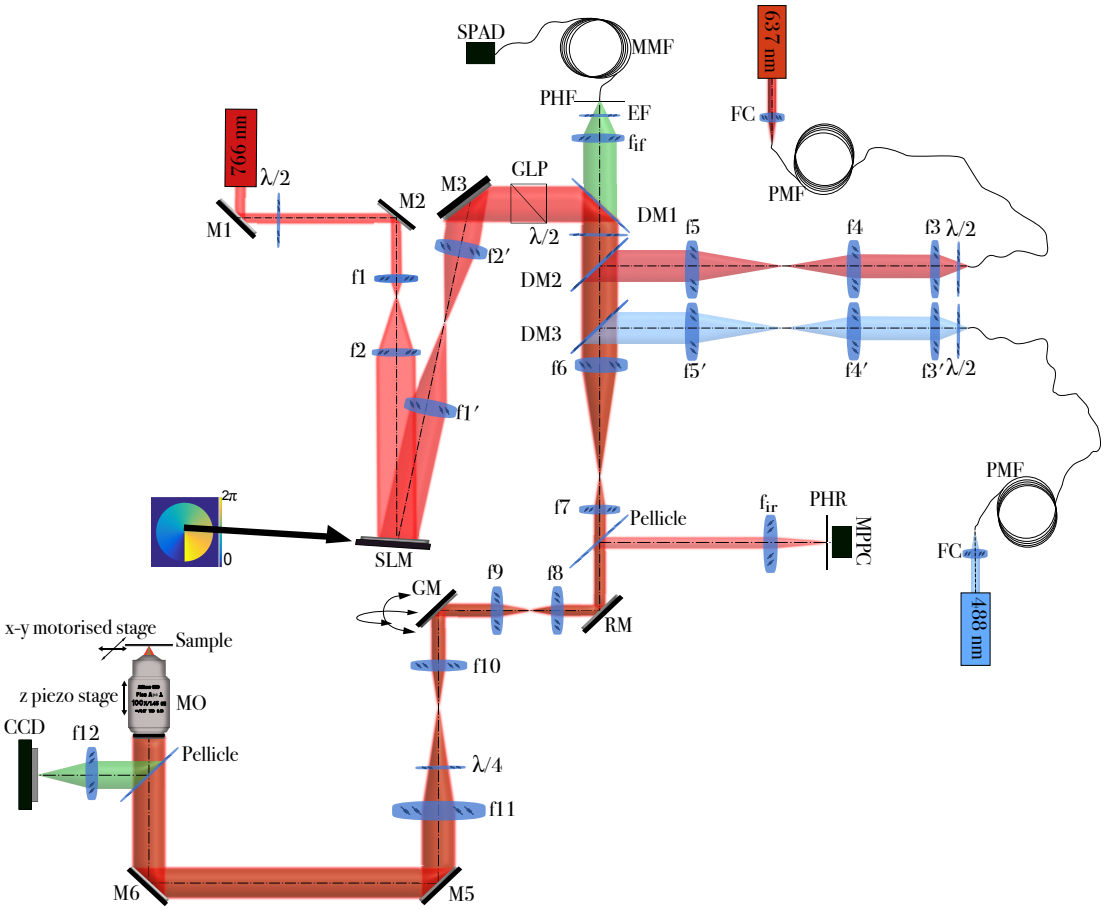

FIGURE 2.1: Schematic of the designed STED microscope. M1-M6 are beam steering mirrors, 766nm, 637nm and 488nm are the wavelengths of depletion and excitation lasers respectively, f1-f12, fir, fif are lenses, FC - fibre coupling lens, RM - resonant mirror, GM - galvanometric mirror, PMF - polarisation maintaining single mode fibre, MMF - multi-mode fibre, pellicle is the 92:2 pellicle beamsplitter, DM1-DM3 are dichroic mirrors, GLP - glan laser polariser,$\lambda/2$ - half-wave plate, $\lambda/4$ - quarter-wave plate, EF - emission filter, PHR and PHF are pinholes, MPPC - multi pixel photon counter, SPAD - single photon avalanche diode, SLM - spatial light modulator. Detailed description of the setup and its elements can be found in text.

2.1.1 Depletion laser beam path

The 766nm depletion beam has a $1/e^2$ diameter of 2.2mm and linear polarisation at the laser aperture. The depletion laser can be set manually to work at 80MHz, 40MHz, 20MHz, 10MHz, 5MHz, or 2.5MHz repetition rates and its pulse duration is approximately 0.5ns. It is deflected by two steering mirrors M1 and M2 and passes through the half-wave plate $\lambda/2$ which rotates its polarisation. $\lambda/2$ ensures that the depletion beam polarisation will match the orientation of the optical axis of the liquid crystal in the liquid crystal on silicon (LCoS) spatial light modulator (SLM) [159]. Lenses f1 and f2 are responsible for beam expansion. The expanded beam

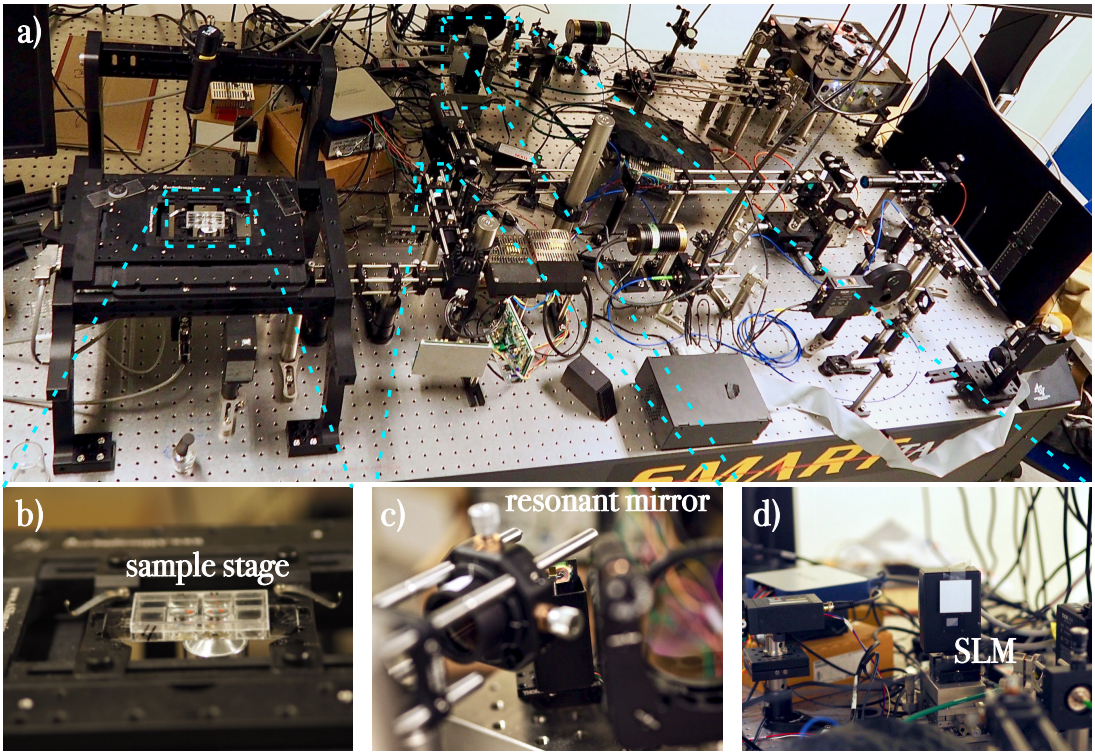

FIGURE 2.2: Photos of the designed and aligned STED microscope system, located in the Physics and Life Science (PaLS) lab at the University of Dundee. a) shows the whole microscope setup on the optical table, with dashed rectangles highlighting some of the critical elements of the microscope, b) is the close up of the XY sample stage with 8-well ibidi sample chamber mounted, c) close up of the resonant mirror and d) is SLM.

size is 16mm, so that the beam diameter overfills the SLM aperture (the aperture is 16mm by 12mm). The SLM displays an appropriate phase mask which shapes the beam. The hologram applied to the SLM is a circular aperture with a blazed grating. The blazed grating is necessary, since it allows the diffraction orders to be spatially separated after the beam reflects from the SLM and ensures we are only using the phase modulated light. The beam shaped by the hologram is represented in the 1^{st} diffraction order of the blazed grating. The size of the phase mask hologram is set to 554 pixels which equates to a 11.08mm beam diameter (the SLM pixel pitch is equal 20µm). A 4f system consisting of lenses f1' and f2' image the SLM hologram plane onto the mirror M3. An image of the SLM plane is shown in the Figure 2.3 a). After reflecting from M3, the depletion beam passes through a Glan-Laser polariser (GLP) that only transmits the linear polarisation corresponding to the SLM polarisation. The fast axis of the GLP is set to maximise the intensity in the 1^{st} diffraction order of the blazed grating. Another half-wave plate, $\lambda/2$, is responsible for rotating the linear polarisation so that when it reaches the quarter-wave plate ($\lambda/4$) the

polarisation state is circular. DM1 is a dichroic mirror, which reflects wavelengths longer than 720nm and transmits wavelengths shorter than 720nm. It separates the fluorescent photons from the depletion beam. Further on, the depletion beam passes through the dichroic mirror DM2 where it is combined with the excitation beam. From DM2, both depletion beam and excitation beam are propagating coaxially using the same optical path. Since the depletion beam is shaped by the SLM, it is very important to accurately image the plane of the SLM onto the back focal plane (BFP) of the objective lens. Proper imaging is assured by three 4f systems:

- lenses f6 and f7, imaging the SLM plane containing the hologram onto the resonant scanning mirror RM,
- lenses f8 and f9, imaging the RM plane onto the plane in-between two galvanometric scanning mirrors GM,
- lenses f10 and f11 imaging GM plane onto the back focal plane of the microscope objective MO.

The intermediate images of the SLM plane are shown in the Figure 2.3. Figure 2.4 shows the locations of the phase masks registered in the intermediate planes of the microscope setup.

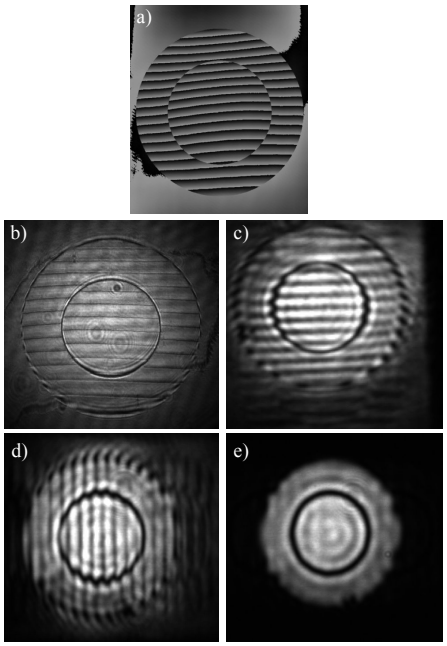

FIGURE 2.3: (a) Top Hat phase mask applied on the SLM and its intermediate images (b) at the M3 plane, (c) at the RM plane, (d) at the GM plane, (e) at the BFP of objective.

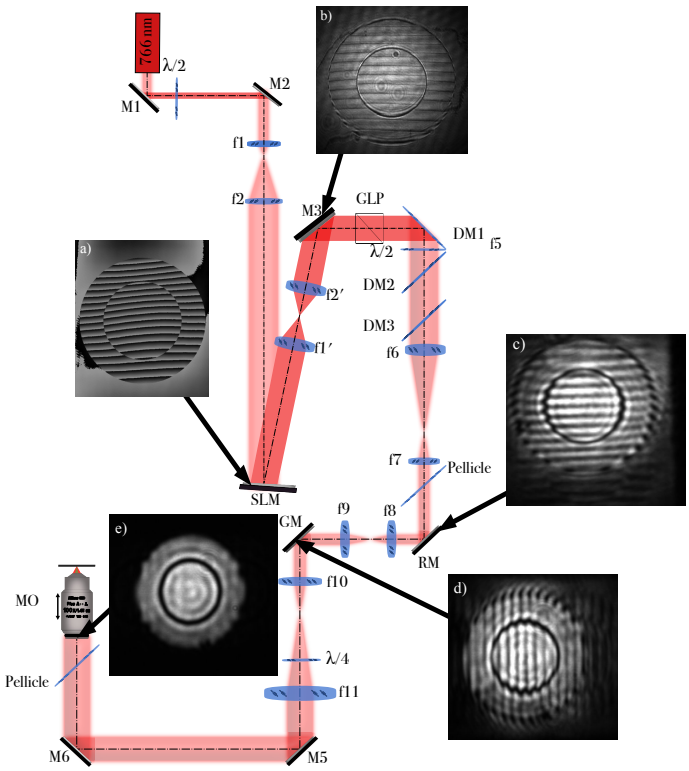

FIGURE 2.4: Locations of Top Hat phase masks from Figure 2.3 with regard to the depletion beam path of the optical setup shown in Figure 2.1.

The SLM phase mask has to be in focus in each of the intermediate image planes, which are the following: M3 plane, RM plane, GM plane and BFP. Apart from proper imaging of the SLM plane onto the BFP, it is crucial to match the size of the phase mask with the pupil size of the MO. The phase mask diameter was calculated, firstly, by placing a CMOS camera at the BFP and phase mask image was acquired. Then, the phase mask diameter was calculated in pixels and multiplied by the camera pixel size (5.2µm) in order to obtain the actual size of the phase mask. According to the calculations, the phase mask size was 1116 pixels which is equal to the 5.8mm. The phase mask image and its size calculations are shown in Figure 2.5.

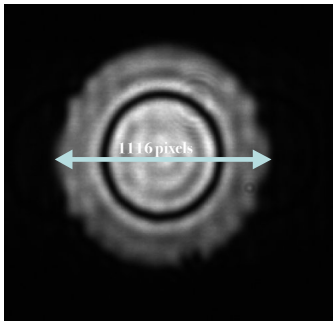

FIGURE 2.5: Image of the phase mask at the BFP of the MO and its size in pixels.

The phase mask image at the BFP was compared to the calculated diameter of the phase mask multiplied by the setup magnification. The total magnification of the depletion beam path is equal to $M_{STED} = 0.53$ and was calculated using the following formula:

$$M_{STED} = \frac{f2'}{f1'} \cdot \frac{f7}{f6} \cdot \frac{9}{f8} \cdot \frac{f11}{f10} \tag{2.1}$$

where each f is the focal length of the lens shown in Figure 2.1. MO entrance pupil diameter is equal 5.8 mm and can be calculated using the following formula:

$$D = 2NA \cdot f = 2 \cdot 1.45 \cdot 2 = 5.8[mm] \tag{2.2}$$

where NA is a numerical aperture of the microscope objective and f is a focal length of the MO. According to the magnification calculations, in order to match phase mask size with the MO entrance pupil size, a hologram displayed by the SLM should have the size of 547 pixels. However, according to the actual calculations, the hologram size equalling 5.8mm at the BFP is 554 pixels, which gives the real magnification equal to $M_{STED} = 0.523$.

2.1.2 Excitation beam path

The excitation beam laser is a pulsed diode laser with a wavelength of 637nm. It can operate at the same repetition rates as the depletion laser, while its pulse width is 90ps. Because of the properties of diode lasers, the output beam has an elliptical shape. Coupling such beam into a fibre results in very poor coupling efficiency. The possible solution to overcome this problem is the use an anamorphic prism pair (APP), which magnify the elliptical beam over one of its axes, making the beam shape nearly circular. As shown in Figure 2.1, the excitation beam, after leaving the laser, passes through APP, and is then coupled into the polarisation maintaining fibre, PMF. Application of the APP resulted in coupling efficiency of 75% compared to the 30% efficiency with no APP applied. Lens f3 is collimating the output of the PMF and has a Gaussian beam profile. The half-wave plate $\lambda/2$, rotates the polarisation to match the polarisation of the depletion beam. Lenses f4 and f5 are expanding the beam, so that its size is equal to 2.1mm. The dichroic mirror DM2 reflects the excitation beam. It is also a plane, where the excitation beam is combined with the depletion beam. After DM2 both STED and excitation beams propagate coaxially. The beam path of the 488nm excitation laser is analogical to the beam path of the 637nm laser.

2.1.3 Common beam path

After both excitation and depletion beams are superimposed, they pass through lenses f6 and f7 and are reflected from the RM. Next, the beams propagate through the f8 and f9 4f system and are reflected from the pair of GM. After GM, the beams pass through the lenses f10 and f11 quarter-wave plate, which changes the polarisation of beams to circular. Finally, the beams are reflected from the pair of steering mirrors M5 and M6 and go through the microscope objective MO, which focuses them onto the sample. The MO is mounted on the piezoelectric scanning stage used for focusing, the sample is mounted on the XY electronically operated translation stage.

2.1.4 Imaging beam path

Three main beam paths can be distinguished when imaging the sample:

- the brightfield imaging path, used for imaging the sample with transmissive light and acquiring data on CCD camera;
- the reflective scanning imaging path, used for imaging the samples that reflect light and acquiring the data with the MPPC photon counter;
- the fluorescent scanning imaging path, used for imaging samples containing fluorescent markers and acquiring fluorescent photons with the SPAD photon counter.

The brightfield imaging path is a detection path which helps in localising desired structures in the sample and finding the initial focus of the MO. The white light diode mounted above the sample passes through the sample and MO. A 92:8 pellicle beamsplitter, reflects 8% of the transmitted light and the lens f12 images the sample plane on the CCD camera. The reflective imaging path is used for imaging samples that reflect either the excitation or depletion beam. Light focused through the objective MO is reflected from the sample and propagates back through the objective lens. Then, it is de-scanned with the GM and RM and 8% of it is reflected from a 92:8 pellicle beamsplitter. Then lens f13 focuses it through the pinhole PHR. The pinhole size is chosen to be approximately 20 Airy Units (AU), resulting in quasi-widefield imaging. Airy units represent the size of the disk radius calculated as a distance between the central maximum and the first minimum of the Airy function. After PHR, the reflected light is collected by the multi pixel photon counter (MPPC).

The fluorescent scanning imaging path is the main imaging path used for detecting fluorescence. Similar to the reflective imaging path, fluorescence from the sample passes through the MO, is de-scanned with the GM and RM, passes through DM2, which separates fluorescence from the excitation beam and passes through DM1, which separates the fluorescent light from the depletion beam. After DM1, a bandpass emission filter, EF, rejects all of the non-fluorescent light and the lens f_{if} couples the light through into the multimode optical fibre MMF which acts as the confocal pinhole PHF. The fibre size is set to approximately 1AU The second end of the MF is attached to the SPAD detector which is counting the incident fluorescent photons.

2.1.5 Pinhole size calculations

The pinhole and its size is a very important part of the confocal microscope. It reduces the out of focus light collected by the detector. Thanks to the pinhole, only light originating in the imaging plane is acquired. It is crucial to pick the correct size of it. If it is too small it will drastically reduce detected signal with no real gain in the resolution. On the other hand, if the pinhole size is too large, the detector will acquire the out of focus light, increasing the background and blurring the image. It has been shown that the optimal size of the pinhole is 1AU [160]. The Airy disc size radius can be calculated using the Abbe's formula:

$$r = \frac{0.61\lambda}{NA} = \frac{0.61 \cdot 637nm}{1.45} = 268nm \tag{2.3}$$

Meaning, that for the excitation beam wavelength of 637nm, the Airy disc radius size is equal to r=268nm. Taking into account the magnification of the whole setup, the Airy disc radius size in the fluorescent pinhole plane PHF is equal to:

$$r_F = 0.268 \cdot \frac{f11}{f_{MO}} \cdot \frac{f9}{f10} \cdot \frac{f7}{f8} \cdot \frac{f_{if}}{f6} = 26.45\mu m \tag{2.4}$$

Similarly, the Airy disc radius for imaging reflective objects PHR is equal to:

$$r_R = 0.268 \cdot \frac{f11}{f_{MO}} \cdot \frac{f9}{f10} \cdot \frac{f_{ir}}{f8} = 35.26\mu m \tag{2.5}$$

Fluorescent imaging pinhole has been chosen so that it would match approximately 1AU, which means that the actual pinhole radius closest to 1AU is 25µm. For reflective objects, in order to obtain quasi-widefield imaging, the pinhole size

diameter is set to approximately 10 AU, for which the actual pinhole radius closest to the calculated Airy disk is 400μm.

2.1.6 Filter Selection

A very important part of the fluorescent microscope setup is the proper choice of filters that will separate the fluorescent photons from any other photons that will introduce noise to the image. Especially when using a high power depletion laser, it is important that the filters have high optical density for cutting out the undesirable light. The fluorescent emission filter EF was placed in front of the SPAD photon counter. In sample staining, the main fluorophores used were Atto 647n and Abberior STAR 635P [161]–[163] that are excited with the 637nm laser and Abberior STAR 470SXP [164] that is excited with the 488nm laser. The absorption and emission spectra for each dye and the excitation and depletion laser lines are presented in Figures 2.6 - 2.8.

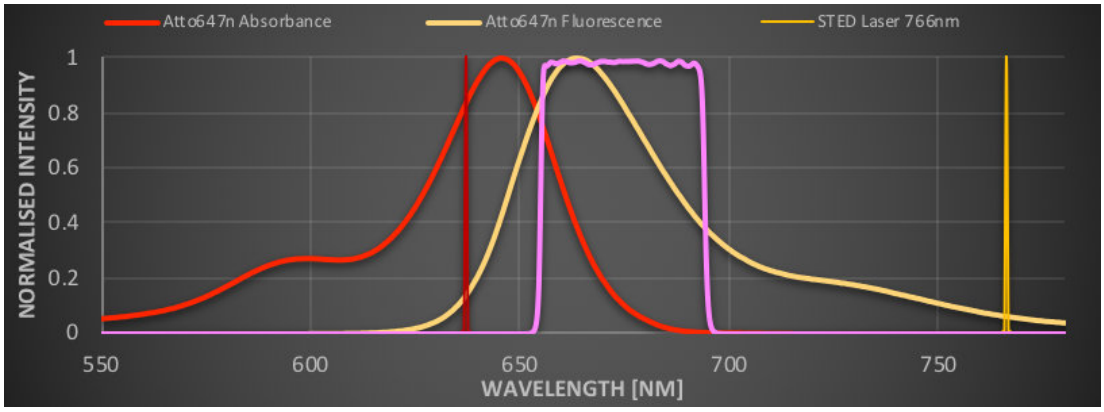

FIGURE 2.6: Graph showing the absorption and emission spectra of the Atto647n dye, excitation 637nm laser line wavelength and 766nm depletion laser line wavelength. Graph also shows the spectral window bandwidth of the chosen emission filter Semrock 676/37.

From analysing the spectra of the fluorescent markers, the Semrock 676/37 emission filter was chosen. This filter transmits the emitted fluorescence of each of the chosen dyes and none of the laser lines. The filter has transmission $T_{avg} > 94\%$ in the wavelength range of 657.5nm - 694.5nm. The optical density of the filter for wavelengths outside of the transmission window is approximately OD=7. Each of the fluorescent emitted photons can be detected with the chosen filter and thanks to the long Stokes shift of the Abberior STAR 470SXP it allows the same depletion laser to be used in order to obtain super-resolution dual colour STED images.

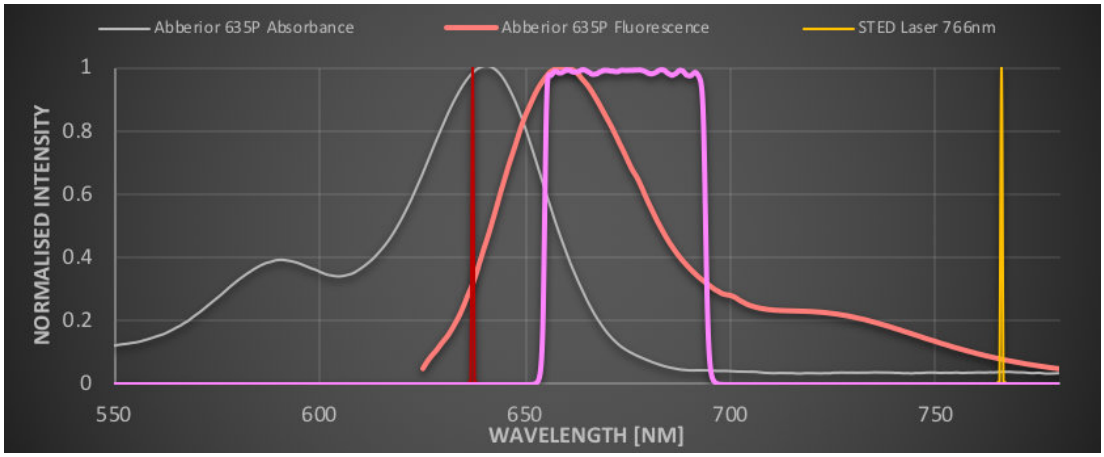

FIGURE 2.7: Graph showing the absorption and emission spectra of the Abberior STAR 635P dye, excitation 637nm laser line wavelength and 766nm depletion laser line wavelength. Graph also shows the spectral window bandwidth of the chosen emission filter Semrock 676/37.

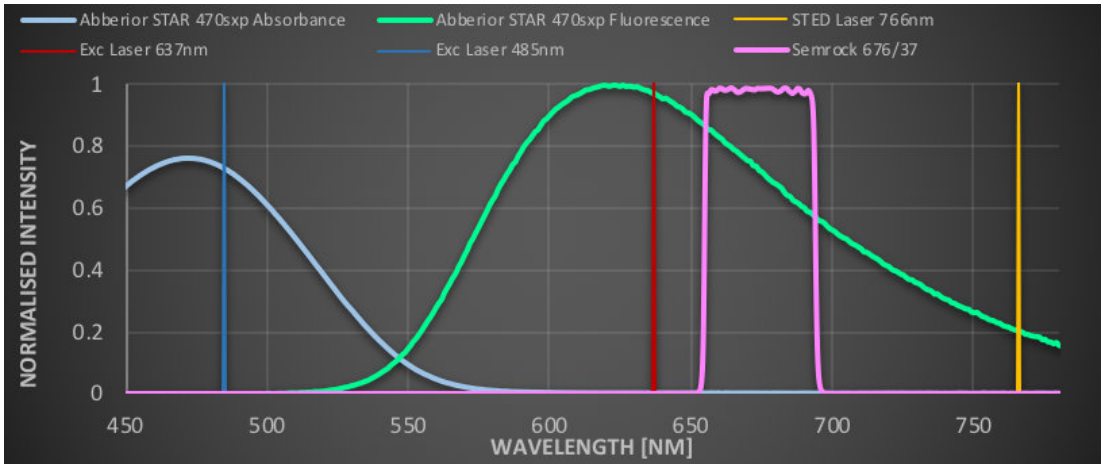

FIGURE 2.8: Graph showing the absorption and emission spectra of the Abberior STAR 470SXP dye, excitation 488nm and 637nm laser line wavelength and 766nm depletion laser line wavelength. Graph also shows the spectral window bandwidth of the chosen emission filter Semrock 676/37.

2.2 Image acquisition and formation

In the laser scanning confocal microscope the image is built point by point by scanning the sample with the focused laser beam. It is carried out by the combination of two scanning mirrors: a galvanometric mirror (GM) for slow axis scanning and a resonant mirror (RM) for fast axis scanning. Figure 2.9 shows a typical scanning pattern resulting in the formation of the image in the resonant laser scanning confocal microscope.

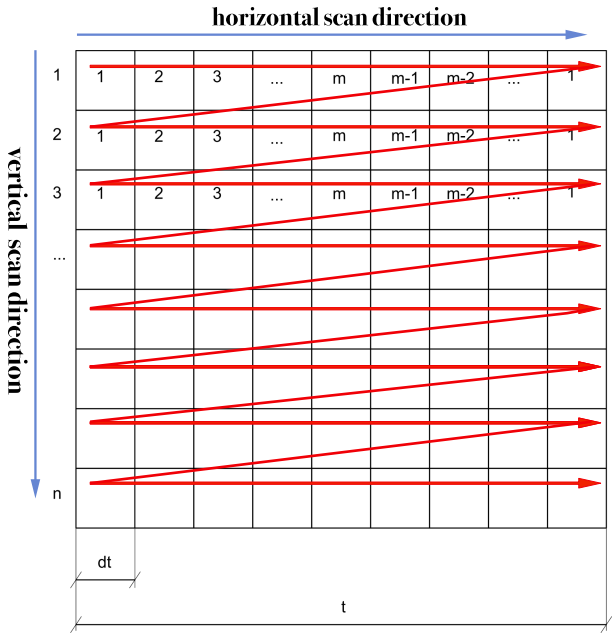

FIGURE 2.9: Schematic of image acquisition in the microscope. Each number represents the pixel of the final image, dt is pixel dwell time (time-frame in which photons are being counted for single pixel). Firstly, a horizontal scan is carried out, acquiring pixels from 1 to m. Horizontal scan is acquired in time equal t=dt·2m. After the horizontal scan is done, beam is moved to the next vertical line. Full image is acquired when all n horizontal line scans are performed. Red arrow represents laser scanning direction when acquiring an image.

Image formation (Figure 2.9) can be described as following:

1. Horizontal line scan. This is the line scan carried out by the resonant mirror. RM has a fixed 16kHz oscillation frequency, which means that the mirror rotates from the 0^o angle to its α_{max} maximum angle and back to 0^o in the period of t=62.5µs. This period is the divided by the requested number of pixels m. Hence, one pixel will have a dwell time of $dt = \frac{0.5t}{m}$. Due to the very rapid movement, pixel dwell times are very short, e.g. for 512 horizontal pixels, $dt \approx 60ns$. For such short dwell times, the number of acquired photon counts is very low, resulting in low signal to noise ratio (SNR). This can be overcome by averaging, either by summing multiple horizontal line scans or by summing multiple frames. Averaging can significantly improve the SNR, but reduces the single frame acquisition time.

2. Vertical line scan. The galvanometric mirror rotates by the required angle after the horizontal scan is finished. This is repeated n number of times. As a result, an image of the size of m x n pixels is obtained. The final acquisition time depends on the number of requested vertical pixels and averaging, e.g. a 512

x 512 pixels image with no averaging will be acquired in $t_I = 512 \cdot 62.5\mu s = 32ms$, which translates to approximately 31 frames per second.

One of the downsides of using the resonant scanning mirror is its non-linear, sinusoidal movement, due to acceleration and de-acceleration at 0^o and α_{max}. Because of this, the pixel dwell dime will be different at the edges compared to the centre of the image, resulting in image elongation at the edges. Typical resonant mirror motion is shown in Figure 2.10.

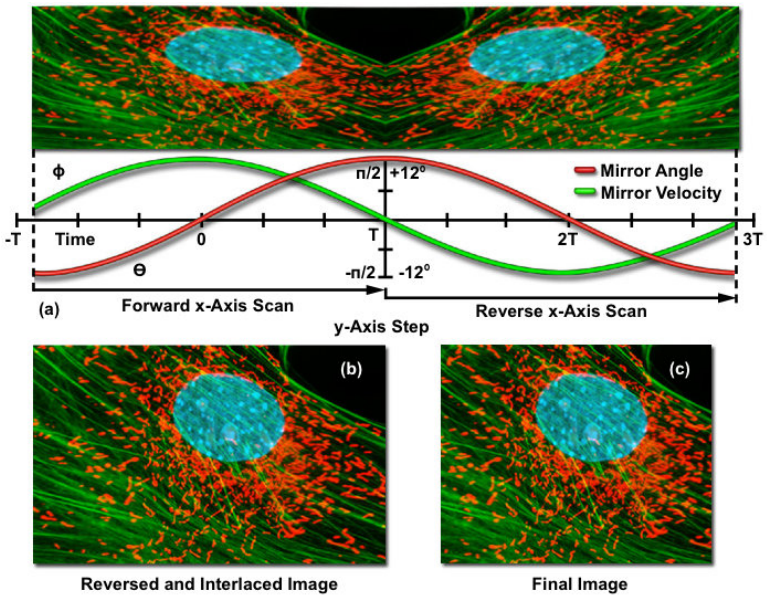

FIGURE 2.10: Typical image and graphs showing raw image acquired using resonant mirror (a). Red curve represents the mirror deflection and green curve represents the velocity at that angle. (b) shows the reversed and interlaced RAW image and (c) the corrected image, with no elongation appearing in the edges of the image (image downloaded from [165]).

The elongation can be corrected using multiple techniques, but they require additional hardware in the microscope setup. Those techniques include image post-processing [166], utilisation of a Ronchi grating for optical generation of the pixel clock [167] and illuminating the back side of the mirror with a laser in order to precisely determine the resonant mirror movement pattern [168]. Coupling Ronchi grating with the photodiode detector generates the feedback through the detected light intensity. As the resonant mirror moves, the light beam scans through the equally spaced grating rulings. The pixel clock is generated by the transitions between dark and bright states corresponding to the clear regions of the grating and it triggers the microscope detector allowing acquisition of equally sized pixels.

A graphical representation of the utilisation of the Ronchi grating is shown in Figure 2.11.

In my design, I decided not to use any of the elongation correction techniques and in the final image I discarded elongated parts of the image, as the developed microscope has already high degree of complexity. During the raw image post-processing, areas acquired with a non-linear velocity are rejected. Since image acquisition is bidirectional, the acquired raw image is doubled, because the resonant mirror period ends at its starting position. In order to utilise the double image, the translation between two images has to be precisely calculated. For this, I employed robust, efficient subpixel image registration algorithm developed by Guizar-Sicairos in the group of prof. Fienup,[169], [170] which I modified to work on the GPU using the Matlab GPU support to increase the processing speed. The algorithm is based on the image upsampled cross-correlation enabling subpixel accuracy to be achieved. The image is first separated into two single images. The second image is flipped and the shift between two images is found. Then the images are either added together or averaged. The Matlab code for the raw resonant image folding is attached in Appendix B.

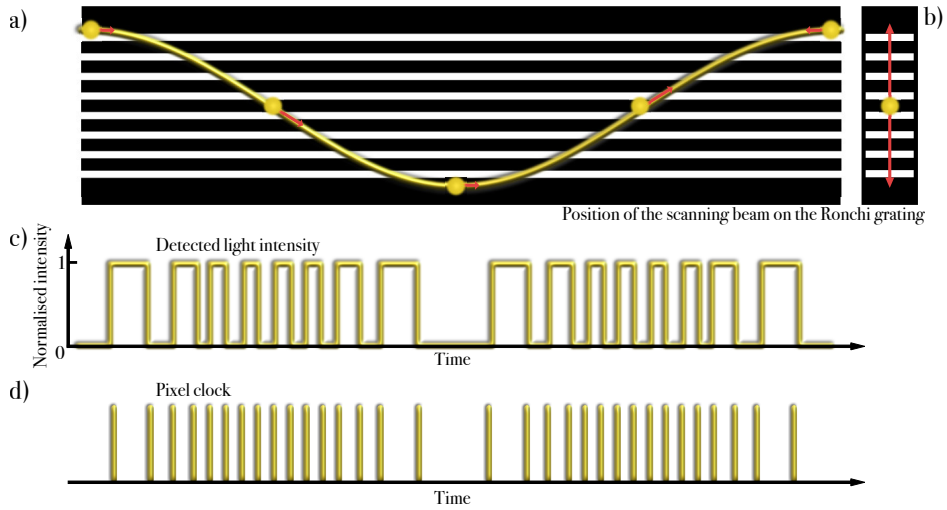

FIGURE 2.11: Application of Ronchi grating for correcting image elongation caused by the inconsistent speed of the resonant mirror. Equally spaced rulings are scanned with the laser light reflected from the resonant mirror (b) with sinusoidal movement profile, represented by the red curve in (a). (c) shows the intensity detected by the photodiode coupled to the grating and (d) is the generated pixel clock corresponding the detected intensity. Pixel clock triggers the microscope detector and thanks to it, acquired pixels have exactly the same size [165].

2.3 Microscope control software

The microscope control software was written in Labview FPGA environment. The system uses a National Instruments FPGA board (PCIe-7852R) for controlling the image acquisition. The block diagram of the acquisition module is shown in Figure 2.12.

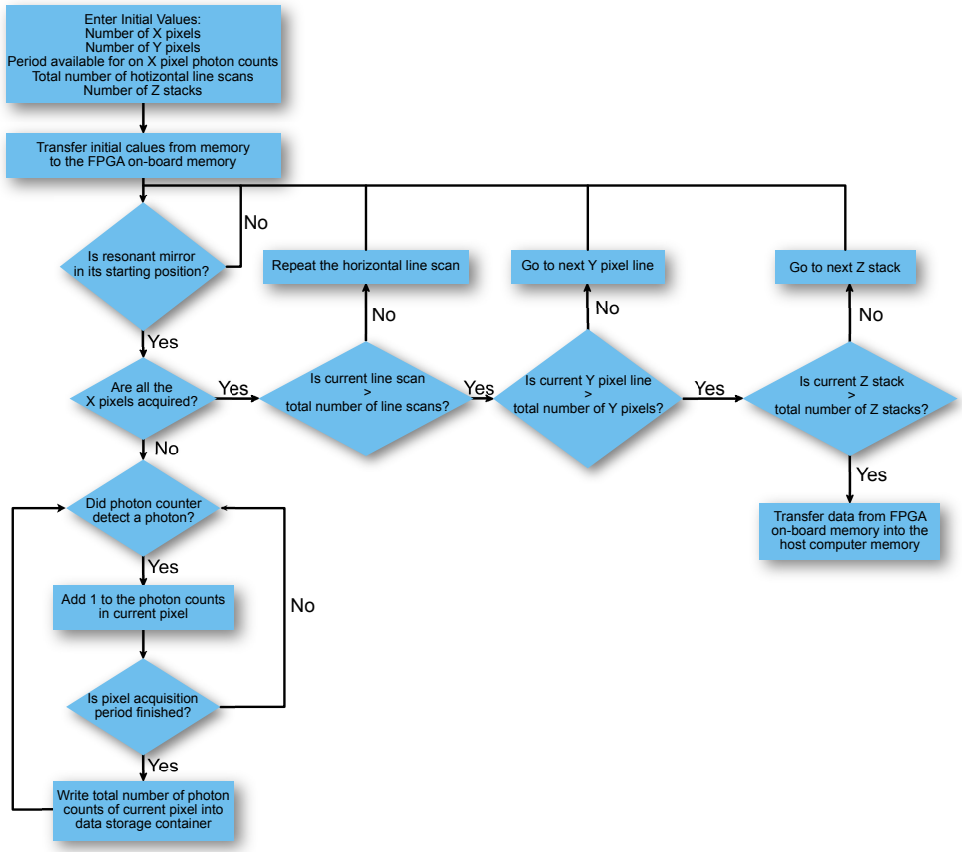

FIGURE 2.12: Block diagram of the image acquisition module of microscope control software.

The FPGA board is responsible for controlling the galvanometric mirrors by applying voltage to them. This causes the rotation of the RM by the angle corresponding to the applied voltage. The FPGA board is also used for detection of a TTL high signal that is generated when the resonant mirror is in its starting position. Both MPPC and SPAD photon counters are connected to the FPGA board and they send a TTL high signal when a photon is detected. The last device connected to the FPGA board is the piezo-electric stage that translates the microscope objective in the axial direction (focusing). The rest of the devices are connected and controlled through LabVIEW by the host computer.

2.4 Adaptive optics and aberration correction

Aberration correction is a very important part of the designed STED microscope. The depletion beam with the vortex or top hat phase mask is very sensitive to aberrations and its shape is easily disturbed when aberrations or misalignment are present. In the system developed for this work, phase mask alignment and aberration correction is carried out by utilising an LCoS SLM. An SLM is a device that can modify the phase of an incident beam. It is filled with anisotropic liquid crystal (LC) molecules, with the same birefringence properties as a birefringent crystal. Depending on the orientation of the optical axis of the LC molecule, its refractive index changes. As a result, light propagating through LC has different propagation speed while passing through differently oriented LC molecules. When a voltage is applied to the SLM, its liquid crystal molecules rotate, changing orientation of their optical axis and effectively their refractive index. This causes the change in the optical beam path of the light propagating through the layer of liquid crystal and ultimately changing the phase of the wavefront of the light that passes through the LC (Figure 2.13). Then, the phase of the SLM is adjusted in the following way. Each of the pixels of the SLM can introduce the phase shift to the incident wavefront in the range from 0 to 2π. Each pixel is responsible for changing the segment of the phase with the size of the pixel. The aberrations cause distortions to the phase of the propagating wavefront. Measuring those distortions we can apply to phase correcting pattern to the SLM, hence correct the aberrations. Then, this phase has to be adjusted in such a way that it will cancel out aberration introduced both by the optical elements and measured specimen.

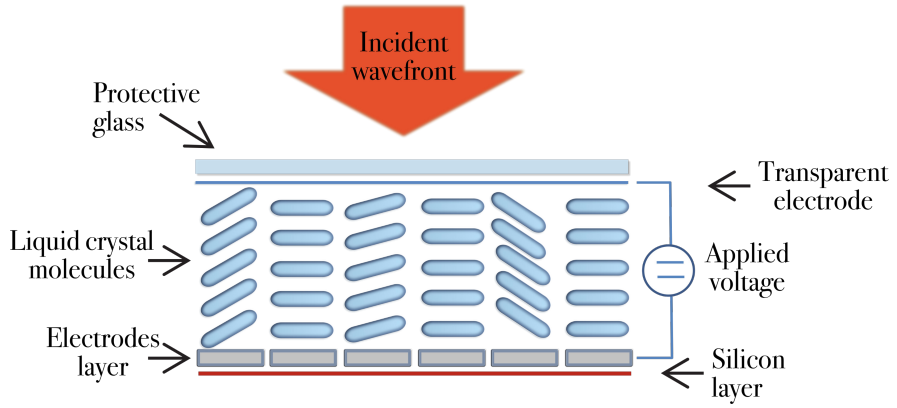

FIGURE 2.13: Schematic of how SLM operates. When voltage is applied, liquid crystal molecules rotate, changing their refractive index which results in modification of the phase of the incident beam.

The aberrations can be mathematically described using Zernike polynomials. Zernike polynomials are used to describe wavefront aberrations for circular aperture. Thanks to this mathematical description, wavefront deformations can be classified and quantitatively described. The aberration correction is carried out by modelling Zernike polynomials and applying them onto the phase mask shaping the depletion beam. A typical applied phase mask is shown in Figure 2.14. The polarisation state of the incident beam has to be linear, matching the orientation of the LC in the SLM, otherwise the SLM will only modulate amplitude of the incident wavefront, while phase will remain unmodified (in the extreme case of crossed linear polarisations). Such a prepared wavefront is reflected from the SLM which modifies its phase. The displayed phase mask is modelled in such a way that it cancels out the aberrations incoming from the optical setup and the sample. The modified wavefront can now properly focus at the desired location even when propagating through a thick, aberrating specimen.

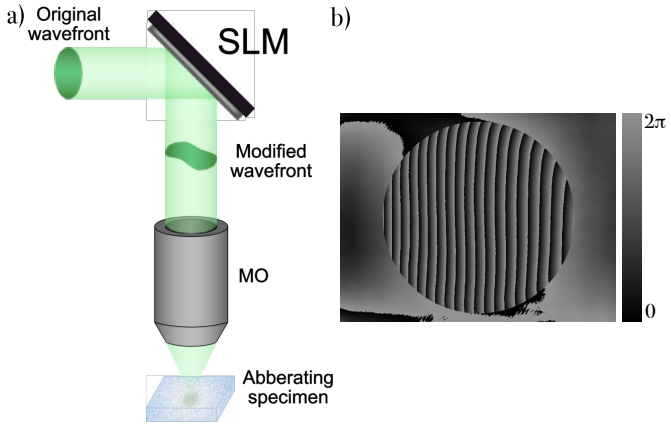

FIGURE 2.14: Schematic of the application of an SLM for aberration correction in microscopy (a). Unmodified wavefront is reflected from the SLM which changes the phase of the incident beam. The wavefront is modified in such a way, that it compensated the aberrations introduced by the specimen. Thanks to the SLM, the beam can reach the desired plane with increased peak intensity when compared to the aberrated beam (assuming the scattering is low). Typical phase mask displayed on the SLM is shown in (b).

The aberration correction method used in the microscope was based on optimisation algorithms and indirect wavefront sensing [100], [171]. Using indirect wavefront sensing requires an iterative search routine that modifies the incident wavefront in accordance to the maxima or minima of the chosen metric. The metric must be directly associated with the image quality or resolution, such as brightness or sharpness [103], [104]. A propagating wavefront can be modelled as a set of orthogonal modes (i.e. independent from each other), such as Zernike modes.

Zernike modes can be described as the polynomials, using the polar coordinates [172]:

$$Z_n^m(r,\varphi) = R_n^m(r) \cdot \begin{cases} \sin(m\varphi) & for \quad m > 0 \\ \cos(m\varphi) & for \quad m < 0 \\ 1 & for \quad m = 0 \end{cases} \tag{2.6}$$

where $R(r)$ is a radial term, r is the normalised circular aperture radius ($0 \leq r \leq 1$), φ is the azimuthal angle measured in the clockwise direction from the y-axis. Subscript n stands for the radial order, superscript m stands for the azimuthal order. Polar coordinates are defined as following:

$$x = r \cdot \sin(\varphi) \qquad y = r \cdot \cos(\varphi) \tag{2.7}$$

Graphical representation of the Zernike polynomials is shown in Figure 2.15.

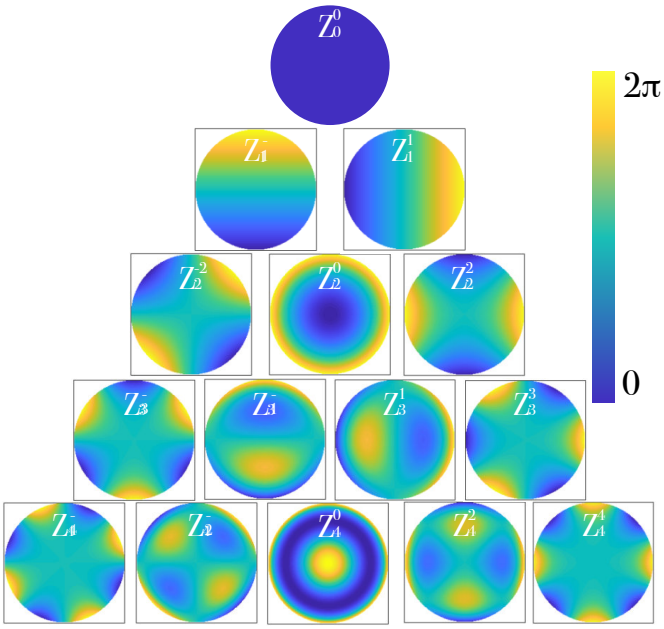

FIGURE 2.15: Zernike polynomials up to a 4th order shown as a phase changes for circular aperture.

Utilisation of the set of orthogonal modes in aberration correction can be described as 'sensorless' wavefront sensing, where the aberration is considered as a summation of orthogonal modes. [103], [173]. In this approach, we first choose the set of modes that will be used for modelling the aberrations, e.g. Zernike polynomials. Aberrations corresponding to Zernike polynomials are corrected one at a time. For each Zernike polynomial Z_n^m corresponding to the currently corrected aberration,

an arbitrary range of amplitudes are chosen. The phase pattern with the range of Z_n^m values is then displayed on the SLM, deforming the wavefront in a controlled manner. An image is acquired for each of the previously defined magnitude of the aberration and the quality metric is calculated. When a set of the quality metric values corresponding to the range of the applied aberration amplitudes is obtained, using the optimisation algorithms we can find an estimate of the aberration amplitude that maximised the quality metric. Then applying the found aberration amplitude will correct the wavefront deformation corresponding to the currently corrected Zernike polynomial. The block diagram representing the correction workflow is shown in Figure 2.16. The aberration process can mathematically be described as an optimisation problem. Having the quality metric chosen, we want to maximise it. Let us denote the metric function as M, which is a function of the set of control signals $P\{c_1,\ldots,c_p\}$ that drive the SLM. The goal of the optimisation is to find a control signal P that will maximise $M\{c_1,\ldots,c_p\}$. The metric function can be expressed as:

$$M \approx M_0 - \alpha(a+c)^2 \tag{2.8}$$

where a is an aberration mode coefficient and α is constant. M_0 and α are unknown, as they are strongly related to the specimen structure, illumination intensity and detection intensity.

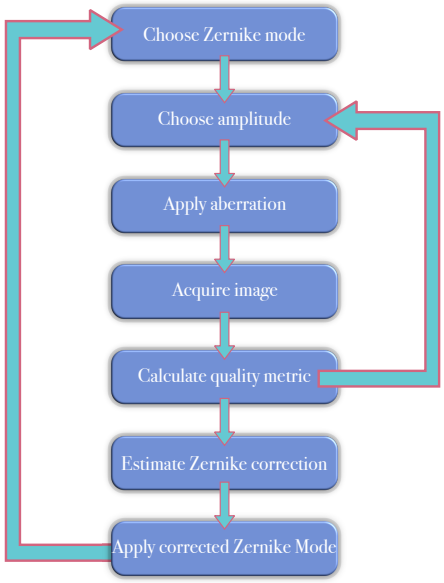

FIGURE 2.16: Workflow of the aberration correction routine used in the developed microscope.

Equation 2.8 obtains its maximum when c=-a. Since the control signal c can be chosen arbitrarily, a can be determined by three measurements of M with different values of c applied. The process of finding a can be described as follows:

- acquisition of an image with zero additional aberration applied (c=0). Metric M_Z corresponding to this image is calculated,
- two images are acquired with small amount of bias aberration applied $c = \pm b$. Metrics $M_+$and $M_$corresponding to the applied aberration are calculated,
- a quadratic maximisation algorithm is used to determine the aberration amplitude a, by using information obtained in previous measurements:

$$a = \frac{b\,(M_+ + M\_)}{(2M_+ - 4M_Z + 2M\_)} \tag{2.9}$$

Using Equation 2.9, the amplitude corresponding to the maxima of the metric M is found, as c=-a. The aberration correction routine is described in Figure 2.17.

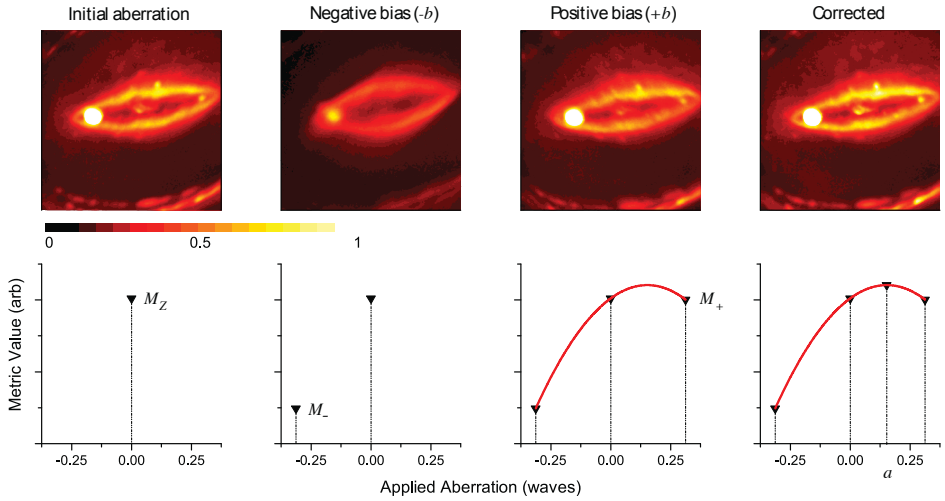

FIGURE 2.17: Aberration correction routine using the indirect wavefront sensing approach (image taken from [173]).

Correcting aberrations of the depletion beam in the STED microscope can be done as following. The depletion beam is initially corrected by direct imaging of the depletion beam using a reflective object, such as gold nanospheres. Using the indirect wavefront sensing technique, the aberrations that are mostly originating in the optical setup are corrected. Zernike polynomials that are corrected in the aberration correction procedure are shown in Table 2.1.

TABLE 2.1: Zernike modes and their mathematical representation that are corrected in the aberration correction procedure

Zernike mode	$Z_n^m(\rho,\theta)$	**Common name**
$Z_{1,1}$	$2\rho\cos\theta$	Tip
$Z_{1,-1}$	$2\rho\sin\theta$	Tilt
$Z_{2,0}$	$\sqrt{3}\left(2\rho^2-1\right)$	Defocus
$Z_{2,-2}$	$\sqrt{6}\rho^2\sin 2\theta$	Oblique astigmatism
$Z_{2,2}$	$\sqrt{6}\rho^2\cos 2\theta$	Vertical astigmatism
$Z_{3,-1}$	$\sqrt{8}\left(3\rho^3-2\rho\right)\sin\theta$	Vertical coma
$Z_{3,1}$	$\sqrt{8}\left(3\rho^3-2\rho\right)\cos\theta$	Horizontal coma
$Z_{3,-3}$	$\sqrt{8}\rho^3\sin 3\theta$	Vertical trefoil
$Z_{3,3}$	$\sqrt{8}\rho^3\cos 3\theta$	Oblique trefoil
$Z_{4,0}$	$\sqrt{5}\left(6\rho^4-6\rho^2+1\right)$	1^{st} order spherical
$Z_{6,0}$	$\sqrt{7}\left(20\rho^6-30\rho^4+12\rho^2-1\right)$	2^{nd} order spherical
$Z_{8,0}$	$3\left(70\rho^8-140\rho^6+90\rho^4-20\rho^2+1\right)$	3^{rd} order spherical

The user has to choose the image quality metric and range of Zernike coefficient values by defining the number of measurements and Zernike coefficient step size. Then, to the acquired set of measurements, a Gaussian curve is fitted. The peak of the Gaussian curve represents the Zernike mode value that maximises the selected quality metric and minimises the aberration corresponding to this Zernike mode. This process is repeated for all the Zernike modes that need to be corrected. After initial aberration correction with gold beads, a second correction is performed. The second correction is necessary, as it enables precise spatial alignment of the excitation and depletion beams and maximises the depletion efficiency in the imaged sample. In the second step of the correction, a fluorescent sample is imaged. When a fluorescent signal is acquired, it is impossible to directly image the depletion beam. In order to do the aberration correction, an image is acquired with both excitation and depletion beams illuminating the sample. The depletion beam has no STED phase mask applied, so a regular Gaussian beam is used. The aberration correction is carried out in a similar manner to the previous step, when gold beads were used, however this time, the valley of the fitted Gaussian curve is found. The valley represents the Zernike mode that maximises the depletion event, which means that the depletion beam has the maximum intensity for the Zernike mode value corresponding to the Gaussian curve minima. Again, this process is repeated for the number of modes that need to be corrected. Typical measurements and curve fits are

shown in Figure 2.18 a) and 2.18 b), while Figure 2.18 c) shows typical corrected phase mask. The aberration correction software was written in LabVIEW and is based on the SLM aberration correction module that was shared by the Dynamic Optics and Photonics group of Prof. Martin Booth.

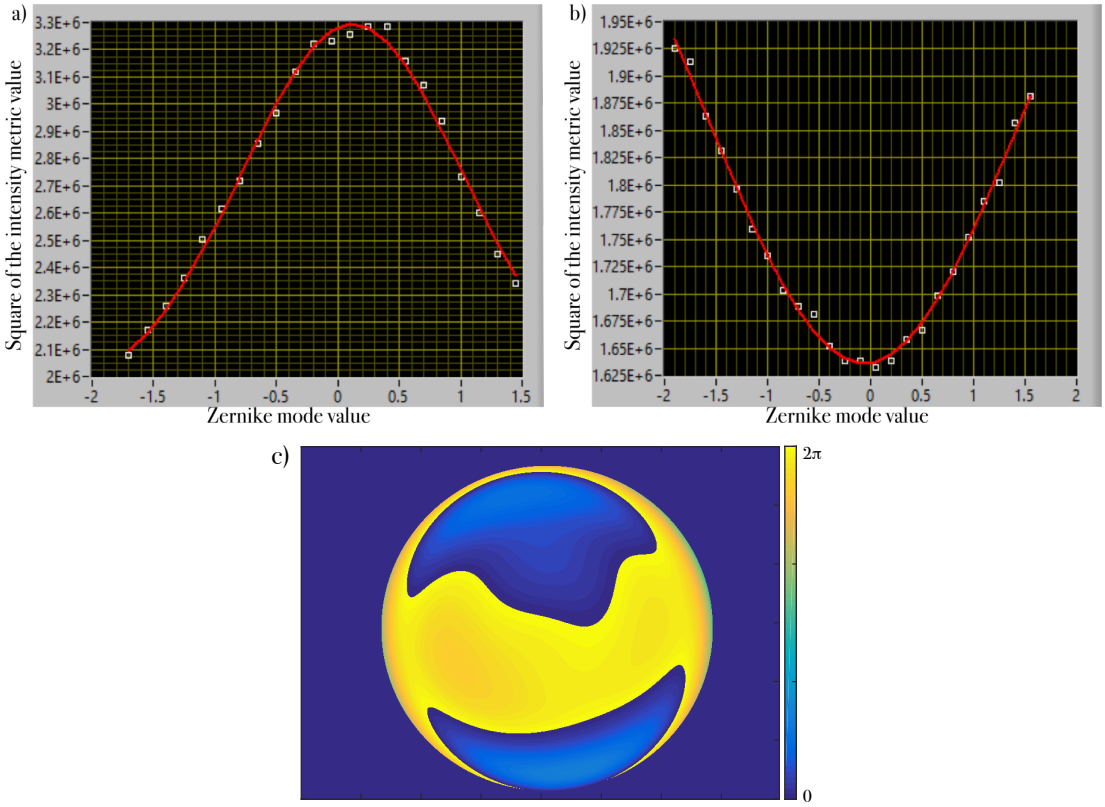

FIGURE 2.18: A Typical aberration correction Gaussian curve fits obtained for (a) direct imaging of depletion beam and finding the maximum of the metric; (b) fluorescent image acquisition and finding minimum of the metric. Both measurements are taken using square of total intensity of acquired image. (c) shows the phase distribution that needs to be displayed on the SLM in order to correct aberrations.

Chapter 3

Experimental methods

3.1 Super-resolution imaging of biological structures.

Having the microscope performance evaluated and being sure it is consistent in getting super-resolution images, the next step was to do the imaging of biological structures. The imaging was done using fixed HeLa cells, fixed RPE-1 cells and fixed iPS cells. The samples were stained using the Atto647n or Abberior STAR635P fluorescent secondary antibodies. The mounting medium that was used was 97% solution of TDE in order to match the refractive index of the immersion oil. It has been shown that TDE has very consistent and proven performance when used in STED microscope [174].

3.1.1 Sample preparation.

- **Cell culture**

  Both HeLa and RPE-1 cell lines were grown in T75 flasks. The growth medium used was DMEM culture media with 10% Fetal Bovine Serum (FBS), 2mM glutamine and antibiotics (100U penicillin / 0.1 mg/ml streptomycin). I used 12ml of growth medium per T75 flask. Cells were cultured in the 37^{o}C CO_2 incubator.

- **Cells splitting protocol**

  When cells reached 100% confluence level they had to be split. I used the regular cell splitting protocol, as following:

  - aspirate growth medium
  - wash cells with phosphate buffered saline (PBS) in order to clean the cells from any dead cells
  - add 2mL of Trypsin to remove the adherent cells from the flask wall

- incubate for 5 minutes in the 37^o CO_2 incubator
- add 10ml of growth medium
- take 500µl - 2ml of suspended cells (depending of the needed cell confluence) and pour them into the new T75 flask
- top up the flask with 12ml of growth medium
- put into 37^o CO_2 incubator

- **Sample preparation**
  For sample preparation, I used #1.5 (0.17mm) coverslips cleaned in the 70% ethanol. When the cell culture reached 100% confluence, cells were split into 6-well plate with coverslips in it, using the same cell splitting protocol described before. Cells were growing on the coverslips in the 37^oC CO_2 incubator until they reached desired confluence level. Then, the samples were fixed with the 3.7% formaldehyde (PFA) or 3.7% PFA with 0.1% Glutaraldehyde. Depending of the used fixation solution, sample preparation differed slightly. Below are the protocols for each step of sample preparation. Usually, the 3.7% PFA with 0.1% Glutaraldehyde is preferred for the microtubules immunofluorescence labelling, as it preserves the microtubule structure much better then pure PFA.

  Preparation of PFA solution:

  - put 10µl of HCl into skirted 50ml Falcon tube
  - put 3.5ml of double-distilled water (DD H_2O) and 10µl of KOH into skirt-less 50ml Falcon tube
  - weight 1.85g of paraformaldehyde and add it to the skirt-less Falcon tube with the DD H_2O
  - boil 0.5l of water in the beaker and put the falcon tube with PFA into it. Loosen the cap of the tube
  - simmer the tube for 5 minutes, until the PFA is fully dissolved in the water and the solution is clear
  - pour the PFA solution into the 10ml syringe and filter it through the 0.2µm filter into the skirted falcon tube with the 10µl HCl
  - top up the PFA solution till 43ml with PBS

For the preparation of 3.7% PFA with 0.1% Glutaraldehyde, the protocol remains the same and additional step is taken at the end with adding 0.1% glutaraldehyde to the final 3.7% PFA solution.

Immunofluerescence labelling protocol:

- warm up the 3.7% PFA (alternatively 3.7% PFA with 0.1% Glutaraldehyde) and PBS to 37^o C in water bath
- take the coverslips with desired confluence level of cells from the incubator and aspirate the growth medium
- wash the cells with warm PBS
- add 0.5ml of 3.7% PFA to each coverslip and incubate for 10 minutes
- aspirate PFA and wash the cells 3 times with the PBS with 0.1% Triton X-100 (PBS-Tx)
- when using 3.7% PFA with 0.1% Glutaraldehyde as the fixing solution, additional step of quenching is needed. Coverslips are put into 1mg/ml of sodium borohydride solution for 5 minutes. Then they are washed 3 times with PBS-Tx
- block the cells overnight with the 1:1000 solution of normal goat serum (NGS) in Antibody Diluting Solution (Abdil)
- wash cells 3 times with PBS-Tx
- add primary antibody solution diluted in Abdil
- incubate for 1hour
- wash cells 3 times with PBS-Tx with 10min incubation times
- add secondary antibodies diluted in Abdil
- incubate for 1hour
- wash cells 3 times with 10 minutes incubation times
- mount the cells with 97% TDE - in order to prevent cellular structure from distortion by osmotic shock during embedding in TDE, the exchange of water with TDE must be slow [174]. That is why the TDE has to be used in the dilution series with PBS:

  > prepare TDE solutions with PBS: 10% (v/v) TDE, 25% (v/v) TDE, 50% (v/v) TDE, and 97% (v/v) TDE.

  > incubate sample in 10% (v/v) TDE for 10 min.

> incubate sample in 25% (v/v) for 5 minutes

> incubate sample in 50% (v/v) TDE for 5 minutes

> incubate sample in 97% (v/v) TDE twice for 5 minutes each

- mount sample using a drop of 97% (v/v) TDE on slide
- seal the coverslip to the slide using clear nail polish
- put the samples into the fridge overnight

- **Dopaminergic differentiation of ChiPSC4 cells**
  Cellartis human iPS cell line 4 (ChiPSC4) dopaminergic differentiation protocol is based on the work published by Chambers et al. [175]. The protocol can be described as following:

  - ChiPSC4 iPS cells (wild type cells (WT) or with Bod1 gene removed (Bod1-/-)) were maintained in mTESR media supplemented with Noggin (10 ng/ml, Peprotech 120-10C), human bFGF (30 ng/ml, Peprotech 100-18B) and 100 U/ml Penicillin/ 100mg/ml Streptomycin.
  - Cells were passaged by treating cells with TryPLE Select dissociation solution at 16 µl/cm2 for 5 - 7 min. Cells were re-suspended in mTESR supplemented as above with 10 µM Y27632 (Tocris 1254).
  - Spin EBs (embryoid bodies) were generated by centrifuging 20,000 cells per well at 600g for 5 min in a 96 well V-bottom plate.
  - EBs were incubated at 37^{o}C, 5% CO_2 for 2 days before being harvested and grown in ultra-low attachment dishes containing 2ml KSR media.
  - After 2 days 50% media was exchanged for N2 media containing LDN-193189 (500nM, Sigma SML0559) and SB-431542 inhibitor (10µM, Transforming growth factor (TGS) beta receptor inhibitor, bio-techne R&D Systems 1614). This exchange was repeated on day 4 and day 6.
  - On day 8 approximately 25 - 30 EBs were plated per well of an ibidi 8 well imaging slide precoated with 1µg/cm2 poly-l-orthinine (Sigma P4957) and laminin (Sigma L5444) into N2-inhib-DA1.
  - Media was exchanged on day 10 and day 12.
  - On day 14 media was exchanged for N2-DA1 and changed on days 16 and 18.
  - On day 20 media was exchanged for N2-DA2 and changed every second day.

- Tissues were fixed and stained on day 30.

KRS media:

- 384 ml Knock Out DMEM
- 100 ml Knock Out replacement serum
- 5 ml glutamax
- 5 ml non-essential amino acids
- 5 ml pen/strep
- 1 ml 2-β-Mercaptoethanol

N2 media:

- Neurobasal media (Fisher 11570556) supplemented with N-2 (Invitrogen 17502048) and B-27 (Invitrogen 17504044)

DA-1 (medium used in the differentiation process)

- N2 media plus:

  20 ng/ml BDNF (Prospec cyt-207)
  200 μM AA (Sigma PHR1008)
  20 ng/ml SHH (US Biological 218561-USB)
  100 ng/ml FGF8 (Prospec cyt-839)

DA-2 (medium used in the differentiation process)

- N2 media plus:

  20 ng/ml BDNF (Prospec cyt-207)
  20 ng/ml GDNF (Prospec cyt-305)
  200 μM AA (Sigma PHR1008)
  1 ng/mlTGFb3 (Prospec cyt-368)
  1 mM cAMP (Sigma D0627)

Chapter 4

Characterisation of an Adaptive Optics STED microscope

Having constructed the AO STED microscope, as described in the Chapter 2, I proceeded to the characterisation of its performance. Following sections show the behaviour of the operating STED microscope and methods used for its characterisation and the importance of the aberration correction of the depletion beam.

4.1 Evaluation of microscope performance using gold beads.

In order to measure the performance of both excitation beam and depletion beam quality it is best to image the beams and calculate their point spread functions (PSF). It is not possible to measure both beams using fluorescent detection, since there are no such beads that would be excited at both wavelengths (637nm and 766nm). Hence the measurements of the PSF for both beams are carried out by imaging gold beads and collecting their reflected signal. Firstly, the PSF of the microscope has been simulated using the following parameters:

- Pixel size: x = 26nm, y = 26nm, z = 30nm.
- Number of z stacks: 100
- NA = 1.45

The simulation was carried out in the ImageJ using the PSF Generator plugin developed at the Biomedical Imaging Group of the École Polytechnique Fédérale de Lausanne (EPFL) [176], [177]. For calculating the theoretical resolution of the bead image, calculations of full width at half maximum values (FWHM) had to be carried out. In order to do that, the cross-section of the bead in the XY, XZ and YZ planes were taken and the Gaussian distribution was fitted to the intensity values.

The fitting was done using an ImageJ curve fitting plugin. The Gaussian distribution formula used in the curve fitting is shown in Equation 4.1:

$$G(x, x_0, \Gamma, a, B) = a \cdot e^{-\frac{1}{2}\left(\frac{x-x_0}{\Gamma/2.3548}\right)} + B \tag{4.1}$$

where x is the position of the cross-section data, x_0 is the position of the centre of the peak, a is the value of the peak's centre, Γ is the FWHM value and B is the background value. Figure 4.1 shows the simulated PSF and its orthogonal views for the excitation laser wavelength 637nm. The graphs in Figure 4.1 show the cross-section of the simulated PSF and Gaussian distribution fitted to it according to the Equation 4.1. Table 4.1 shows the FWHM values obtained for the simulated PSF. Figure 4.2 and Table 4.2 show simulated PSF and the FWHM values obtained for the same simulation for the wavelength equal to the depletion laser wavelength 766nm.

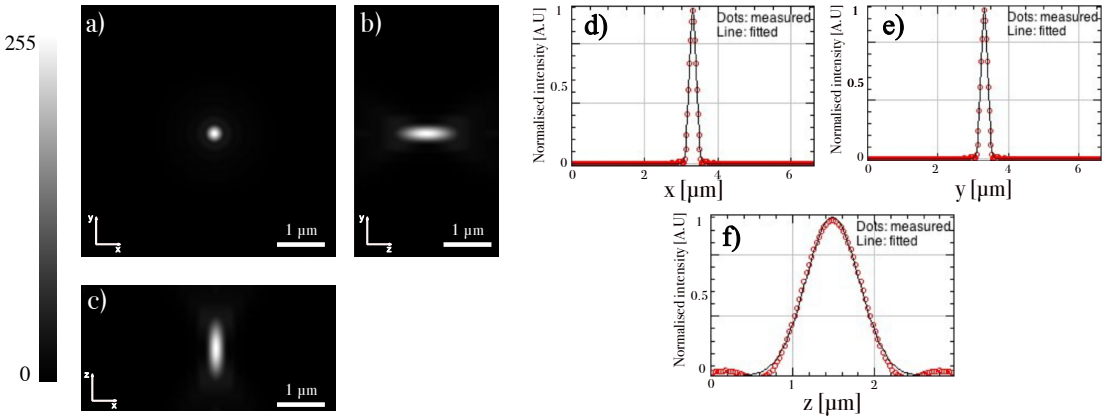

FIGURE 4.1: 256x256 pixels simulation of the PSF for 637nm using the scalar Born & Wolf's approximation algorithm [178]. a) presents xy plane of the PSF, b) yz profile, c) xz profile; d) x profile and Gaussian fitting, e) y profile and Gaussian fitting, f) z profile and Gaussian fitting

TABLE 4.1: Calculated FWHM for the simulated PSF shown in Figure 4.1.

	Number of pixels	**Pixel size [nm]**	**FWHM [nm]**
x	256	26	219
y	256	26	219
z	100	30	763

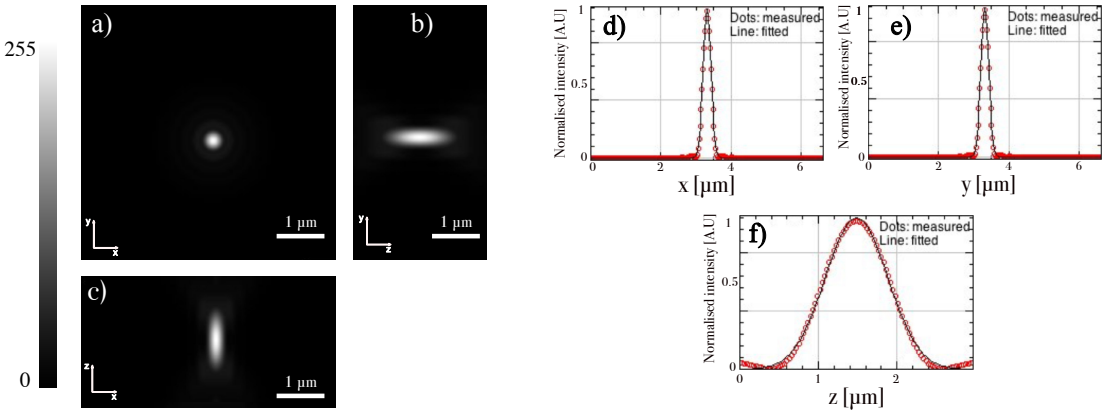

FIGURE 4.2: 256x256 pixels simulation of the PSF for 766nm using Born & Wolf's algorithm. a) presents xy plane of the PSF, b) yz profile, c) xz profile; d) x profile and Gaussian fitting, e) y profile and Gaussian fitting, f) z profile and Gaussian fitting.

TABLE 4.2: Calculated FWHM for the simulated PSF shown in Figure 4.2

	Number of pixels	**Pixel size [nm]**	**FWHM [nm]**
x	256	26	262
y	256	26	262
z	100	30	938

Having the simulated PSF for the experimental microscope configuration the next step is experimental verification carried out by imaging gold beads. 150nm gold nanoparticles from BBI solutions were diluted in ethanol and spread onto the coverslip, which was then mounted using the 97% solution of TDE on the microscope slide. Figure 4.3 and Figure 4.4 show the obtained PSF for both excitation beam and depletion beam. Table 4.3 and Table 4.4 show the FWHM values calculated for both beams. Images of gold beads were recorded for pixel size of 20nm and total number of pixels of 256x256. The stack size was 20nm and total number of line scan averages was set to 100. The field of view was 5µm x 5 µm.

TABLE 4.3: Calculated FWHM for the recorded PSF of 256x256 pixels 150nm gold bead recorded with excitation laser.

	Number of pixels	**Pixel size [nm]**	**FWHM [nm]**
x	256	26	247
y	256	26	233
z	100	30	708

Imaging gold beads also helps to image and evaluate the quality of the phase mask applied on the SLM as well as spatial alignment of both STED and excitation beams.

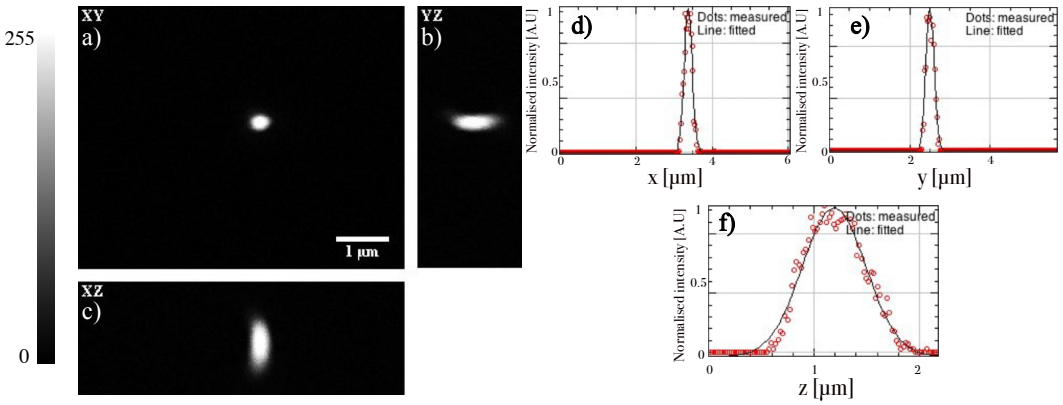

FIGURE 4.3: 256x256 pixels PSF of 150nm gold bead image recorded with excitation laser. a) presents xy plane of the PSF, b) yz profile, c) xz profile; d) x profile and Gaussian fitting, e) y profile and Gaussian fitting, f) z profile and Gaussian fitting.

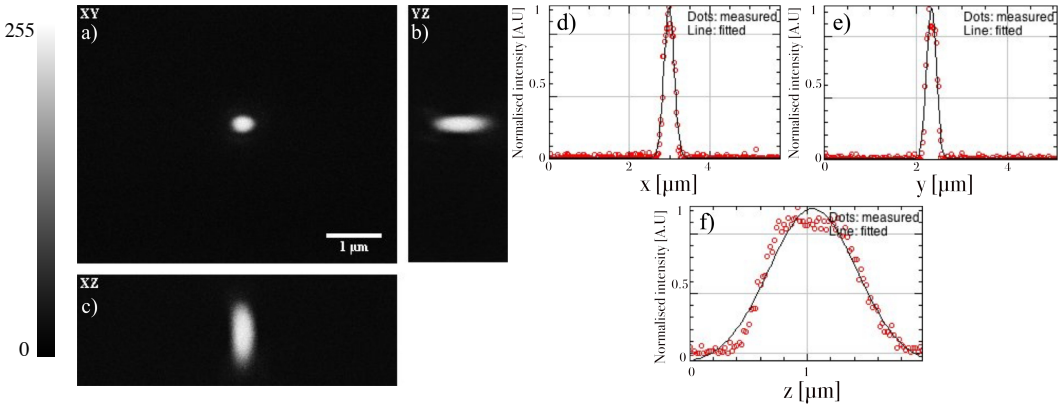

FIGURE 4.4: 256x256pixels PSF of 150nm gold bead image recorded with depletion laser. a) presents xy plane of the PSF, b) yz profile, c) xz profile; d) x profile and Gaussian fitting, e) y profile and Gaussian fitting, f) z profile and Gaussian fitting.

TABLE 4.4: Calculated FWHM for the recorded PSF of 256x256 pixels 150nm gold bead recorded with depletion laser.

	Number of pixels	**Pixel size [nm]**	**FWHM [nm]**
x	256	26	296
y	256	26	243
z	100	30	881

Imaging of the beam shape modified with the phase mask applied on the SLM is very important, as aberrations can significantly distort the Laguerre-Gaussian beam. A directly imaged depletion beam with vortex phase mask, top hat phase mask and the effect of aberrations and misalignment in the beam are shown in Figure 4.5. Figure 4.6 shows the proper spatial alignment and superposition of excitation beam and depletion beam.

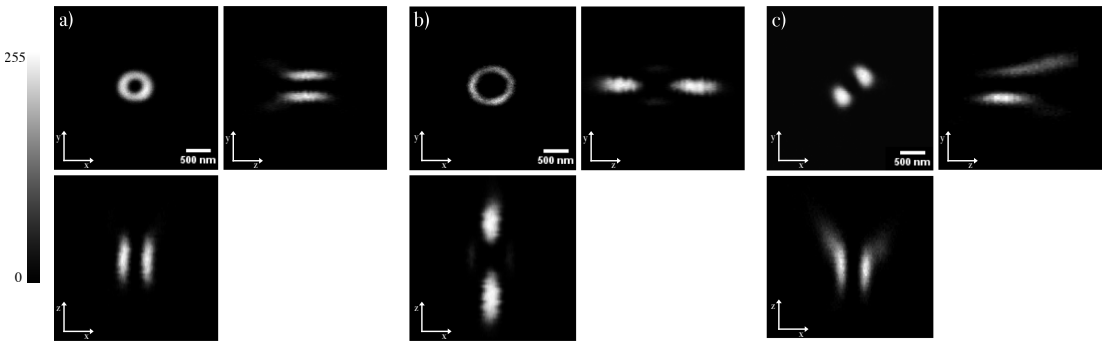

FIGURE 4.5: Depletion beam shape imaged with the 150nm gold beads. a) vortex phase mask is used for creating Laguerre-Gaussian for 2D STED; b) π-step phase mask is used for creating a 3D depletion beam; c) effect of misalignment and aberrations on depletion beam.

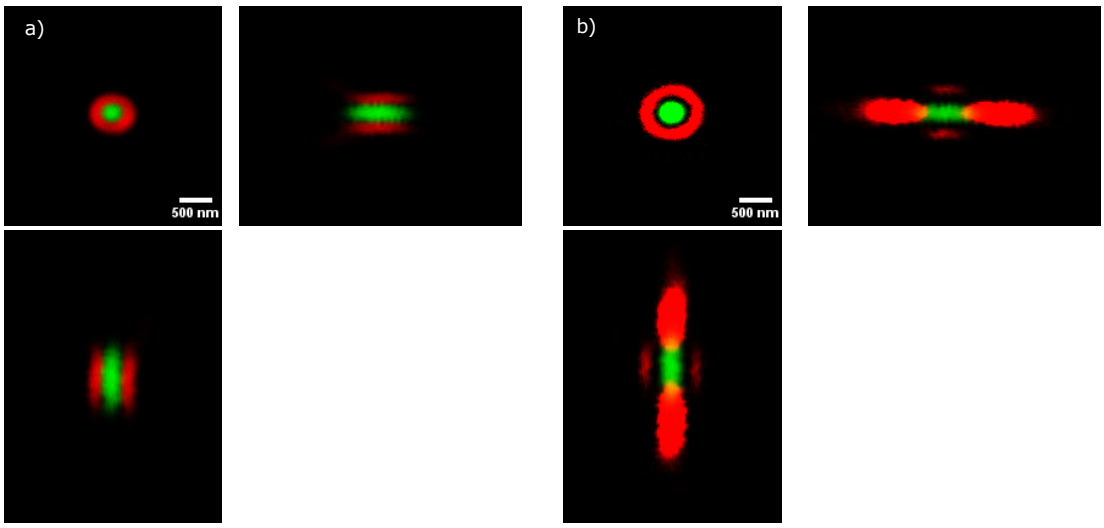

FIGURE 4.6: Depletion beam phase mask imaged with the 150nm gold beads merged with the gold bead recorded with the excitation beam. This shows spatial alignment of the excitation and depletion beams. a) vortex phase mask creating Laguerre-Gaussian beam creating 2D depletion beam; b) π-step phase mask creating the 3D depletion beam.

4.1.1 Laser pulse measurements

With proper spatial alignment of the STED and excitation beams, the next step is to check the temporal alignment of the pulses of both lasers. In order to do that, pulses were measured with a 2GHz photodiode (Thorlabs DET025A/M) and a fast 2GHz oscilloscope. Pulses can be finely tuned using the electronic pulse delay unit (MPD Picosecond Delayer). Results of the pulse measurements are shown in Figure 4.7.

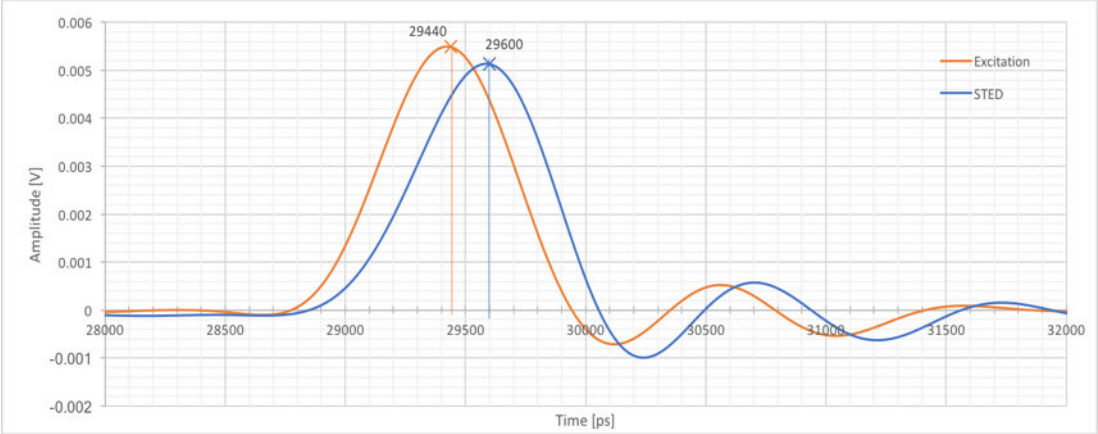

FIGURE 4.7: Pulse measurements for excitation beam (orange) and depletion beam (blue).

Pulses had to be measured separately for each laser, since the time resolution of the diode was not sufficient to distinguish both pulses simultaneously. According to previous reports, STED pulse should arrive approximately 150ps after the excitation pulse, so that depletion the highest efficiency [128], [149]. Measurements shown in Figure 4.7 show both pulses measured for the delay set to 2020ps, which makes the depletion beam arrive ≈160ps after the excitation pulse. The pulses were set to 40MHz repetition rate.

4.2 Fluorescent beads measurements

The next microscope performance test was imaging of fluorescent beads. The chosen beads have to be much smaller than the anticipated resolution of the microscope. The chosen beads were 23nm Gatta-Beads filled with Atto647n dye supplied by the GattaQuant were already mounted on slides by the manufacturer. Figure 4.8 shows images of fluorescent beads acquired in the confocal mode and for both 2D and 3D STED phase masks.

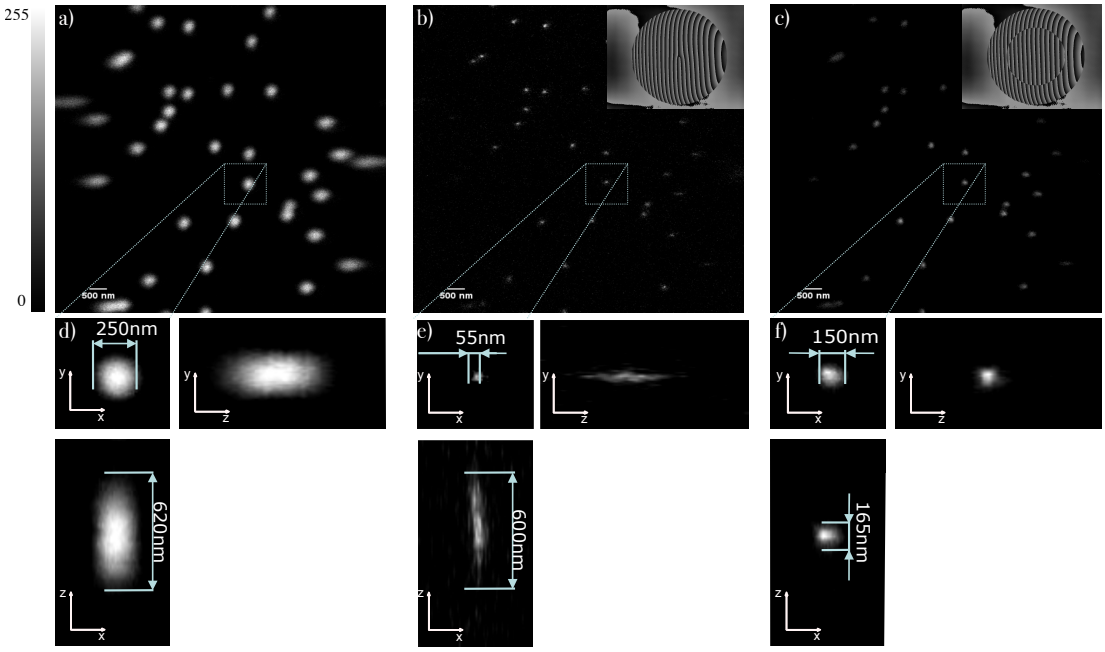

FIGURE 4.8: Comparison of the (a) confocal, (b) 2D STED and (c) 3D STED images. Zoomed bead and its orthogonal views for confocal, 2D STED and 3D STED microscope modes is shown on images d), e), f) respectively.

It is clear that there is a significant increase in the resolution of the STED images well below the diffraction limit. For the evaluation of the resolution, several beads were chosen and their FWHM was calculated. For calculating the FWHM the cross-sections of the beads in XY and XZ plane were taken and either Gaussian (confocal) or Lorentzian (2D STED and 3D STED) fits were done. For classic, confocal PSF determination, blurring of the early photons can be accurately described using the Gaussian function [127], [149]. Unfortunately, a Gaussian function is not a good model for approximation of the PSF in the STED imaging. For the determination of the FWHM of the STED images, a well established approximation of the STED PSF is Lorentzian function [141], [179]. All the calculations were done in ImageJ using the curve fitting option. The Gaussian distribution formula was already shown in Equation 4.1 and formula for a Lorentzian distribution is shown in Equation 4.2:

$$L(x, x_0, \Gamma, a, B) = a \cdot \frac{\left(\frac{\Gamma}{2}\right)^2}{(x - x_0)^2 + \left(\frac{\Gamma}{2}\right)^2} + B \tag{4.2}$$

where x is the position of the cross-section data, x_0 is the position of the centre of the peak, a is the value of the peak's centre, Γ is the FWHM value and B is the background value. Figure 4.9 shows an example cross-section in XY and XZ planes of the beads for different microscope modes(confocal, 2D STED, 3D STED) and

either Gaussian distribution fit (confocal images) or Lorentzian distribution fit (2D STED and 3D STED). The images were acquired using 56mW depletion laser power measured at the BFP. Figure 4.10 shows the calculated FWHM for the set of 20 fluorescent beads acquired for all three microscope acquisition modes: confocal, 2D STED and 3D STED. FWHM was calculated for both XY and XZ planes. The values of the obtained FWHM are a good approximation of the resolution of the STED microscope developed for this work.

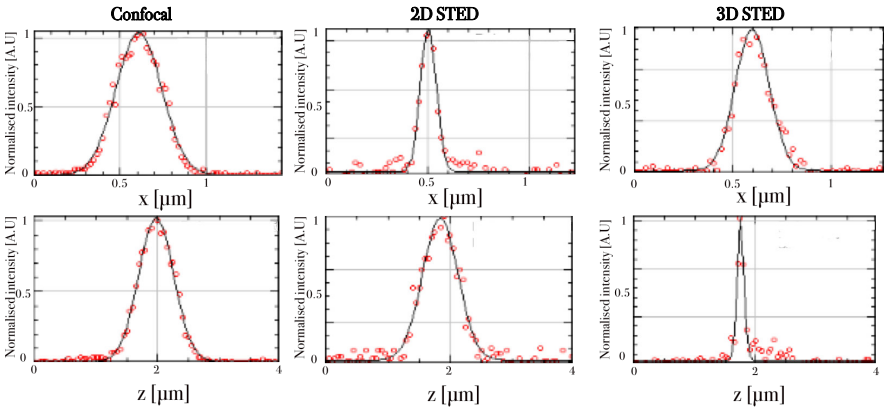

FIGURE 4.9: Typical cross-section of the fluorescent beads for confocal, 2D STED and 3D STED microscope modes. Gaussian or Lorentzian curves were fitted to the cross-sections in order to calculate the PSF and FWHM for each of the microscope modes. Top row present the XY plane cross-section and bottom row presents XZ plane cross-section.

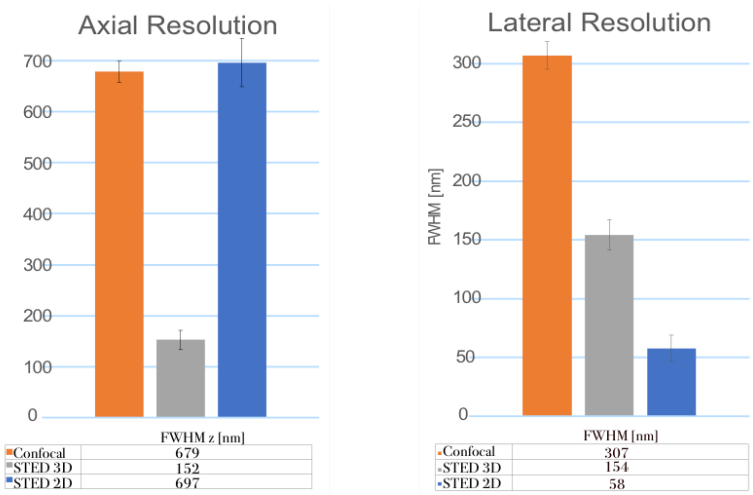

FIGURE 4.10: Calculated average axial and lateral FWHM for the set of 20 fluorescent beads for different microscope modes: Confocal (orange), 2D STED (blue) and 3D STED (grey).

As a next step of the evaluation of the microscope performance, measurements of the resolution of the microscope for different depletion laser powers were taken. The theoretical lateral STED resolution can be approximated using Equation 4.3.

$$d_{STED} = \frac{0.45\lambda}{NA\ \sqrt{1+\frac{I}{I_{sat}}}} \tag{4.3}$$

where I is the depletion laser intensity and I_{sat} is the fluorophore saturation intensity, measured for the drop of total fluorescent intensity by the factor of $1/e$. Table 4.5 shows the FWHM values obtained for the fluorescent beads acquired using 2D STED phase mask for different depletion laser powers.

TABLE 4.5: Measured lateral resolution of the STED microscope for different depletion laser powers

STED Power [mW]	**FWHM ± STD [nm]**
5.5	155 ± 5.15
10	121 ± 5.1
21	91 ± 9.14
41	70 ± 6.9
56	61 ± 5.4

Figure 4.11 presents the theoretical curve of the STED microscope resolution for different values of depletion laser power. The saturation intensity for the fluorescent beads that were used in the experiment (23nm Gattabeads filled with Atto647n fluorophore) $I_{sat} = 5.5mW$ at the BFP of the microscope objective. The measured values fit well with the theoretical STED resolution curve which means that the performance of the microscope is consistent and proper.

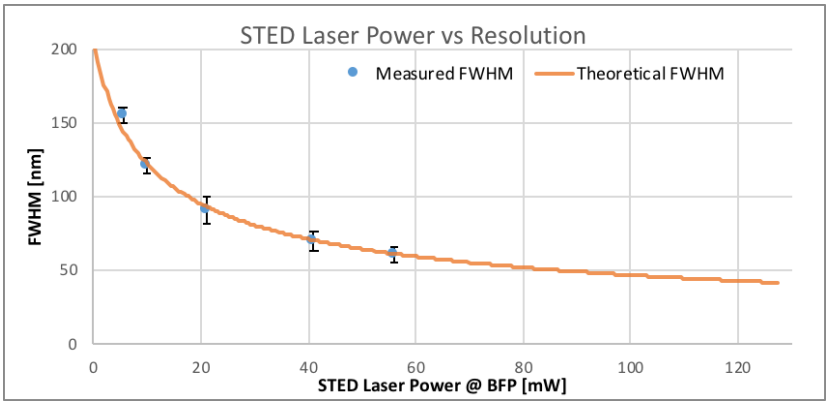

FIGURE 4.11: Theoretical STED resolution curve for the $I_{sat} = 5.5mW$ and the measured FWHM of the fluorescent beads obtained for the fluorescent beads images acquired for different depletion laser power at 40MHz repetition rate.

The next measurement regarding the performance of the microscope was the evaluation of the pulse delay giving the most efficient depletion and resolution increase. Thanks to having the electronic pulse delay unit, it is possible to easily change the delay of the depletion laser pulse with regard to the excitation laser. As before, the same fluorescent bead sample was used and images were acquired for different pulse delay values and constant depletion average laser power of 56mW. The obtained results are shown in the Table 4.6 and Figure 4.12 and are consistent with the previously published results [149], [180], confirming that the most efficient depletion and increase of the resolution is for the depletion laser pulse delay of approximately 160ps, measured as the distance between two excitation and depletion pulse peaks.

TABLE 4.6: Measured STED microscope resolution using 2D STED phase mask and different depletion laser pulse delay values.

Pulse delay [ps]	**FWHM [nm]**
60	70
160	55
260	60
360	67
460	90

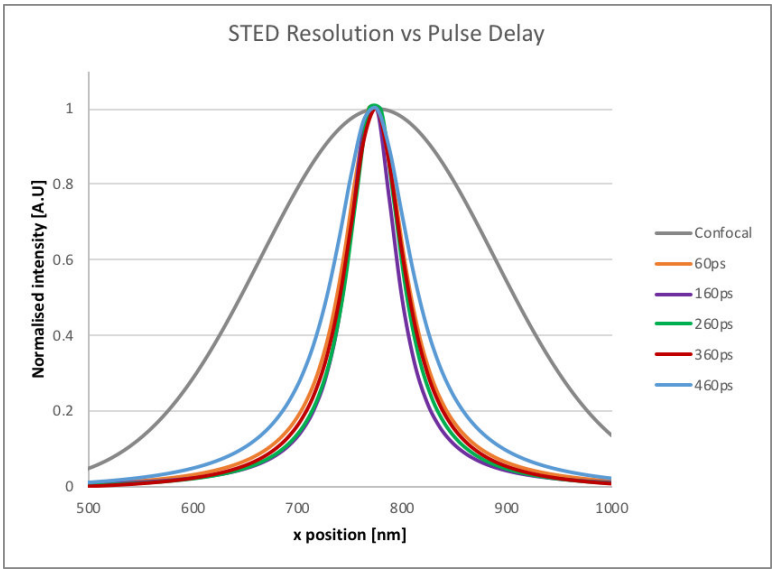

FIGURE 4.12: Graph showing the Gaussian fit (confocal curve) and Lorentzian fit (STED) obtained for the fluorescent beads images acquired with 2D STED phase mask and different pulse delay values.

4.3 Summary and conclusions of the microscope performance evaluation.

As shown in the previous sections, I have successfully built an AO STED microscope. I was able to quantify its performance based on the imaging on gold beads and fluorescent beads. According to the performed measurements, the microscope can carry out measurements with the lateral resolution up to 55nm using the classical, vortex STED phase mask and axial resolution up to 160nm with the use of the Top Hat STED phase mask. In my design I take advantage of the SLM that is used for both dynamic change of the depletion beam phase mask and aberration correction. Aberration correction routine (sensorless wavefront sensing) implemented in the microscope setup can compensate for aberrations that are introduced by the optics (static aberrations), as well as aberrations originating in the imaged sample (dynamic aberrations), thanks to the feedback loop. Knowing the microscope performs consistently and having quantified its resolution I was able to proceed to the imaging of the more challenging and interesting biological structures.

Chapter 5

Biological samples imaging results.

The main reason for constructing a super-resolution fluorescent microscope is to use it for imaging of the biological structures. This chapter presents results of the imaging of different type of cells with the sub-diffraction resolution both in lateral and axial direction.

5.1 Imaging of HeLa and RPE-1 cells microtubules.

The first biological structures I was interested in imaging were microtubules. I used both HeLa and RPE-1 fixed cells for the experiment. Figure 5.1 shows the HeLa cell microtubules, labelled using immunofluorescence labelling protocol described in methods chapter 3, acquired with three different microscope modes: confocal, 2D STED with vortex phase mask and 3D STED with top hat phase mask. Cells were fixed with 3.7% formaldehyde. The experiment conditions used to acquire images in Figure 5.1 were:

- primary antibody: mouse α-tubulin, 1:200 dilution
- secondary antibody: anti-mouse Abberior STAR 635P, 1:50
- image size: 1536 x 1536 x 80 voxels
- voxel size: 18nm x 18nm x 50nm
- single plane acquisition time: 41s

The images show the lateral plane at the 2.35µm volume of the sample. It is clear, that the resolution significantly increased when using either of STED modes compared to confocal image. 2D STED image is much sharper in the XY plane, however, the axial resolution is comparable to the resolution obtained with confocal imaging. The axial resolution of the 3D STED image is much higher when compared to both confocal and 2D STED modes. 3D STED image also shows the slight increase in the lateral resolution.

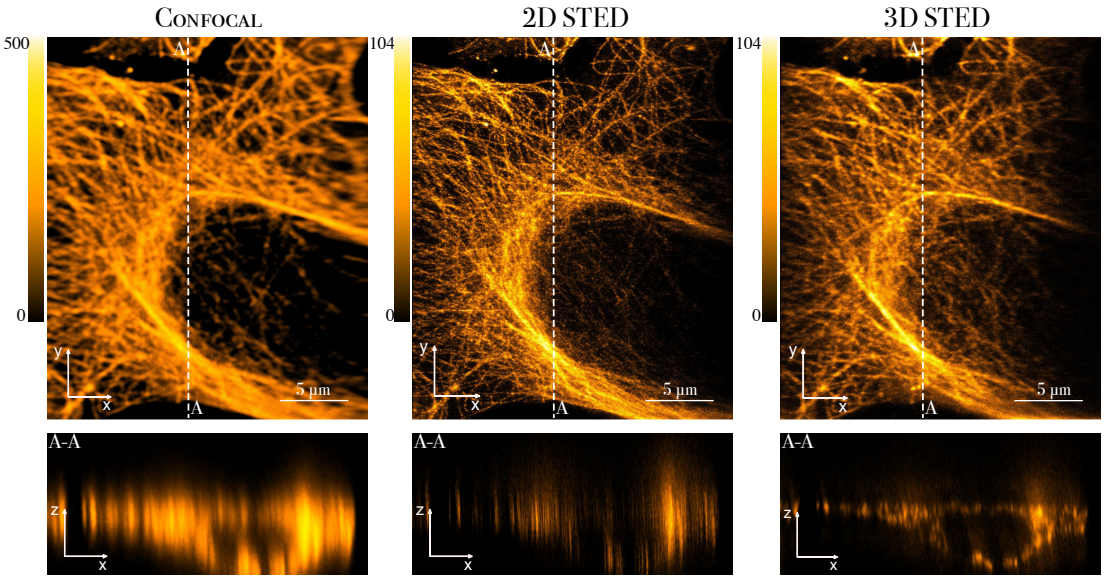

FIGURE 5.1: HeLa cells α-tubulin labelled with Abberior STAR 635P. Top raw shows the lateral plane images, bottom row shows the axial plane images in the ZX plane at the A-A cross-section marked with the white, dashed line

5.2 Mitotic spindle imaging of the RPE-1 cells.

One of the goals of the project was to use the STED microscope built to obtain super-resolution images of the human mitotic spindle. To achieve that, RPE-1 cells were used. They were fixed in 3.7% formaldehyde with 0.1% glutaraldehyde. Figure 5.2 shows the mitotic cell in early anaphase. Images were taken using all the microscope modes: confocal, 2D STED and 3D STED. What is worth noting, is that the obtained image of the mitotic cell has significant thickness of approximately 12µm. When compared to published super-resolution STED images, presented results usually are just single XY plane images at the edge of the coverslip. Thanks to using the SLM for aberration correction, fine alignment of depletion beam with regard to the excitation beam and possibility to change the depletion beam phase mask, it is possible to acquire 3D super-resolution images of the biological structures. Aberration correction for the depletion beam was carried out for the whole volume of the imaged mitotic cell, with the Zernike modes corrected as shown in Table 2.1.

The experiment conditions used to acquire images in the Figure 5.2 were:

- primary antibody: mouse α-tubulin, 1:200 dilution
- secondary antibody: anti-mouse Abberior STAR 635P, 1:50 dilution
- image size: 1728 x 1024 x 240 voxels

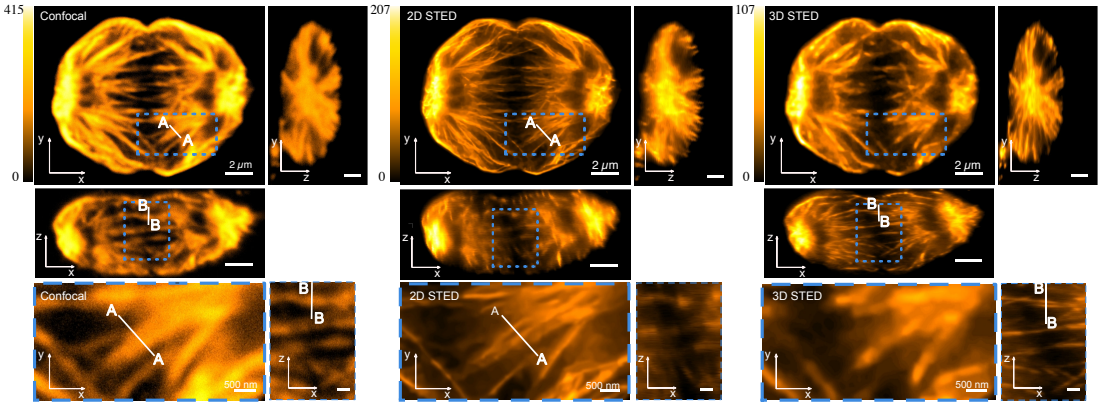

FIGURE 5.2: Comparison of the mitotic spindle images of RPE-1 cells with α-tubulin stained with the Abberior STAR 635P acquired for different microscope modes: confocal, 2D STED and 3D STED.

- voxel size: 18nm x 18nm x 50nm
- single frame acquisition time: 31s

Dashed blue rectangles in Figure 5.2 show the area that was zoomed and shown in the bottom row. A-A and B-B mark the position where the cross-sections were taken in order to measure the FWHM of the single microtubule showed in the images. The cross-sections and the Gaussian curves fitted to them are shown in the Figure 5.3.

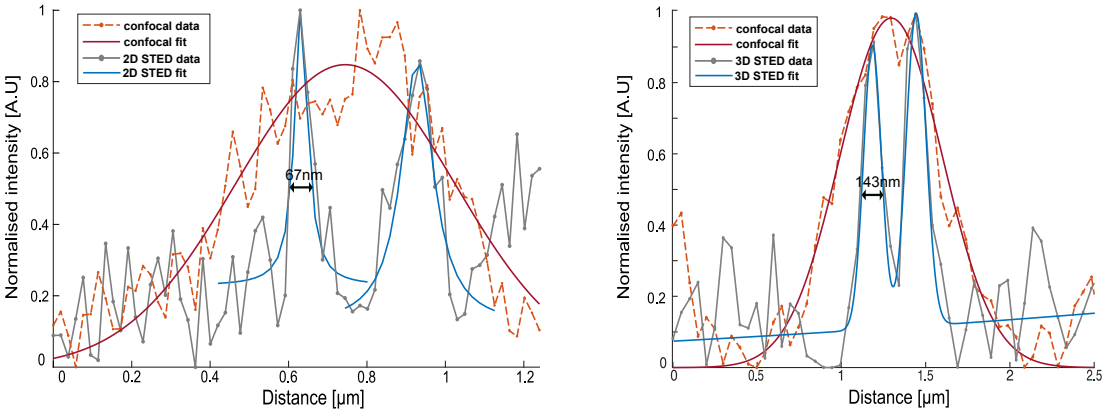

FIGURE 5.3: Cross-sections A-A and B-B of the microtubules shown in Figure 5.2. Red lines represent Gaussian fits for the images obtained in the confocal mode, blue lines represent Lorentzian fits for the images obtained in the 2D STED (A-A) or 3D STED (B-B) modes.

Red curves represent the Gaussian fit to confocal cross-sections and blue curves represent Lorentzian fit to 2D STED (A-A) and 3D STED (B-B) fit. Similar to the bead images described in section 4.2, curve fitting was carried out using the curve fitting tool of ImageJ and the Gaussian fit was done according to Equation 4.1, while

the Lorentzian fit was performed according to the Equation 4.2. The FWHM was calculated for both cross-sections and the results confirmed the previously calculated FWHM for the fluorescent beads shown in Chapter 4. The lateral FWHM calculated for the microtubule image acquired in 2D STED mode was 67nm and axial FWHM calculated for the image acquired in 3D STED mode was 143nm. Figure 5.4 shows another example of the mitotic cell being in the late anaphase. Similarly, an image stack was acquired for 3 different microscope modes. Both 2D STED and 3D STED show significant increase in the resolution. Super-resolution images show much more detail either laterally and axially. As when imaging the mitotic cell in Figure 5.4, an aberration correction routine was performed for the whole volume of the mitotic cell in which the same 9 Zernike modes were corrected. When imaging the mitotic cells, the aberrations could be treated as constant in the full volume of the mitotic spindle, as the correction at different planes and for the full volume gave comparable results.

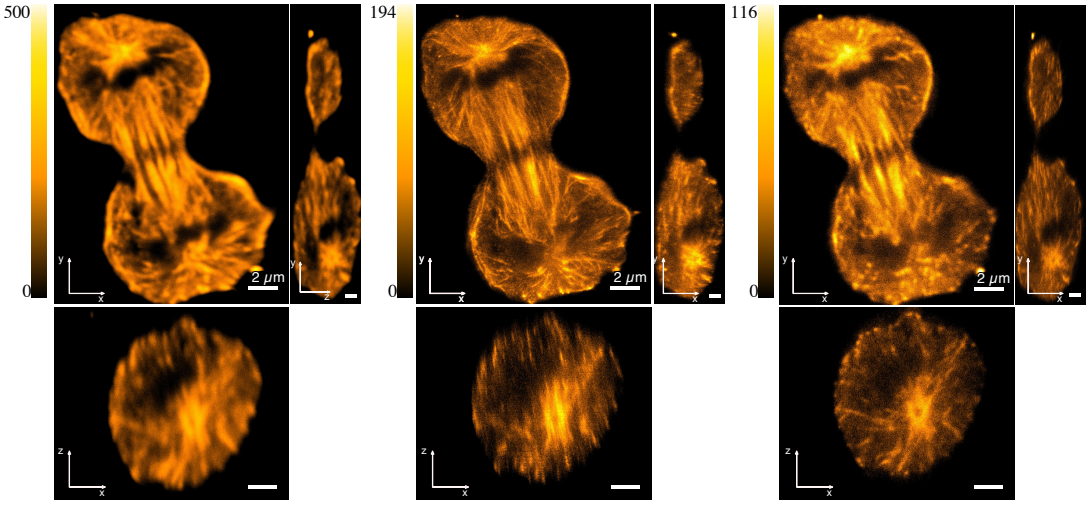

FIGURE 5.4: Comparison of the mitotic spindle images with α-tubulin stained with the Abberior STAR 635P acquired for different microscope modes: confocal, 2D STED and 3D STED.

The experimental parameters that were used to obtain the images were same as when acquiring the stack in Figure 5.4:

- primary antibody: mouse α-tubulin, 1:200 dilution
- secondary antibody: anti-mouse Abberior STAR 635P, 1:50
- image size: 1728 x 1024 x 240 voxels
- voxel size: 18nm x 18nm x 50nm

- single frame acquisition time: 31s

5.3 Dual colour imaging

The next experiment I carried out was to confirm the ability of dual colour imaging with the built STED microscope. In order to do that, a second excitation laser with the wavelength of 488nm was used. Specially designed for STED, a long stoke shift dye was used. A long stoke shift, in theory, should enable the use of two fluorescent dyes with different absorption spectra and deplete them with the single depletion wavelength. Figure 5.5 shows a comparison of confocal and 2D STED images of RPE-1 mitotic cell acquired using 488nm excitation laser and 766nm depletion laser.

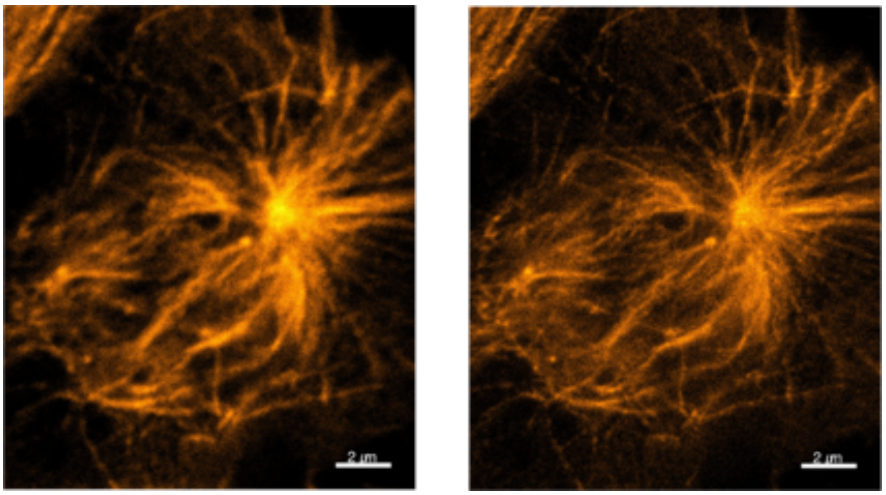

FIGURE 5.5: Comparison of confocal (left) and 2D STED (right) images of mitotic cell with α-tubulin labelled with Abberior STAR 470SXP

Experimental parameters used for obtaining the images were:

- primary antibody: rabbit α-tubulin, 1:100 dilution
- secondary antibody: anti-rabbit Abberior STAR 470SXP, 1:50 dilution
- image size: 1024 x 1024 x 25 voxels
- voxel size: 20nm x 20nm x 200nm
- single frame acquisition time: 12s

The images in Figure 5.5 prove that the proposed STED microscope is working with the long stoke shift dye, as the 2D STED image is sharper than the confocal one.

However, the big problem with the dye was that the photobleaching was so severe, that it does not allow for proper 3D imaging. This is why, this dye was usually used only for obtaining a second channel for reference. It turned out to be very useful for imaging of the mitotic cell structures such as pericentrin. Figure 5.6 shows RPE-1 dual-colour STED image.

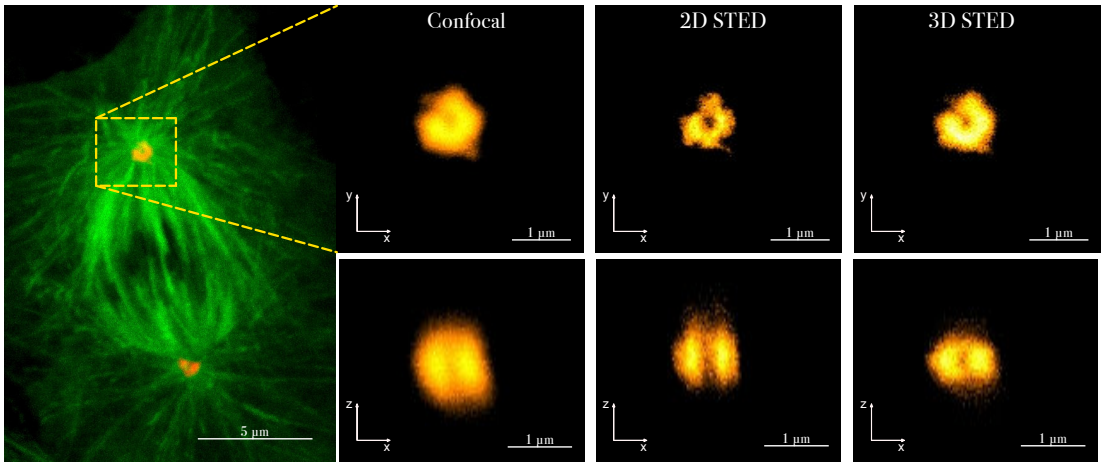

FIGURE 5.6: Dual colour 3D projection of mitotic cell with α-tubulin labelled with Abberior STAR 470SXP (green) and pericentrin labelled with Abberior STAR 635P (orange). Images on the right show zoomed structure of pericentrin acquired with confocal, 2D STED and 3D STED microscope modes. Bottom row shows XZ plane images for confocal, 2D STED and 3D STED images.

Figure 5.6 was acquired for the following experimental conditions:

- 1st primary antibodies: rabbit α-tubulin, 1:100 dilution
- 1st secondary antibody: anti-rabbit Abberior STAR 470SXP, 1:50
- 2nd primary antibody: mouse Pericentrin, 1:250 dilution
- 2nd secondary antibody: anti-mouse Abberior STAR 635P, 1:50
- image size: 1024 x 1024 x 120 voxels
- voxel size:
  - blue channel: 27nm x 27nm x 100nm
  - red channel: 27nm x 27nm x 50nm
- single frame acquisition time:
  - blue channel: 7.3s

  - red channel: 12.1s

α-tubulin structure in the Figure 5.6 is acquired using only confocal acquisition, as the Abberior STAR 470SXP photobleaches very quickly and it was impossible to acquire a full 3D super-resolution stack of it, as it requires longer exposure times and acquisition of 3 different stacks. However, an additional channel is always useful in imaging of biological structures, even if it only gives a reference image without the super-resolution option.

5.4 iPS cells imaging

The most challenging imaging experiment carried out by the proposed 3D STED microscope was the imaging of the iPS cells. They were cultured in the 8-well chambered coverslip. While growing, iPS cells create random structures and the microscope needs to be able to image through the thick tissue. In some areas of the coverslip, they grow layers of tissue, while other areas show axons at the edge of the well. For that reason, a second SLM was added to the 637nm excitation laser, so that sample introduced aberrations can also be corrected for the excitation beam. It is very important, especially when imaging through thick layers of tissue, as they introduce strong spherical aberrations which are increasing with the depth. An aberration correction routine was carried out for the structure that was imaged for both excitation and depletion beams. Figure 5.7 shows the image of the iPS cell labelled with the Tuj-1 primary antibody, a neuron-specific tubulin marker. The cells were mounted in the 97% TDE mounting media. Images were acquired from the region of the coverslip, where the axon grew at the edge of the coverslip, hence the aberrations were not very strong. It is clear that the STED imaging shows more detail of the dendrite attachments, and with 2D STED imaging all the structures are much sharper. Such detail of the dendrite attachments would be impossible to acquire using confocal microscope. Similarly, with the 3D STED imaging the axial resolution is much higher, what can be seen in the comparison of the XZ plane image in the Figure 5.7. Experimental parameters used for acquiring the image in Figure 5.7 were:

- primary antibodies: mouse Tuj-1
- secondary antibody: anti-mouse Abberior STAR 635P
- image size: 1024 x 1024 x 100 voxels

- voxel size: 18nm x 18nm x 50nm
- single frame acquisition time: 21.7s

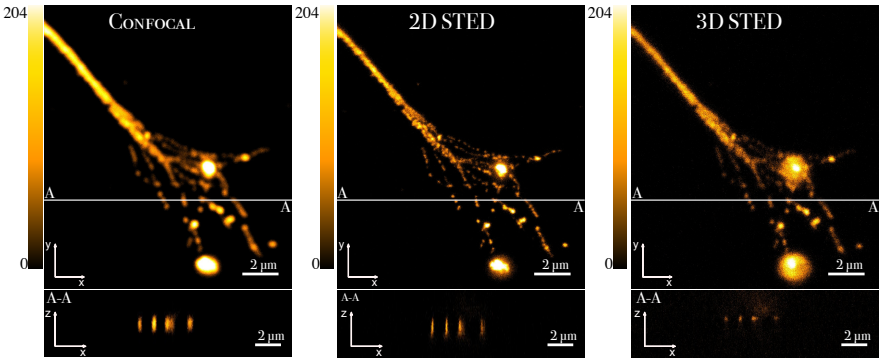

FIGURE 5.7: iPS cell culture with the iPS cell specific tubulin marker: Tuj-1. Images show the single axon end that grew at the coverslip. It was imaged using confocal, 2D STED and 3D STED modes.

The microscope showed its real capabilities in the imaging of the iPS cells with the developed thick tissue in the sample. Figure 5.8 shows the confocal image of axon deep below the surface of the thick tissue. The bleached rectangle in the image shows the area where the STED images were taken, as they were acquired before obtaining the stack of the tissue.

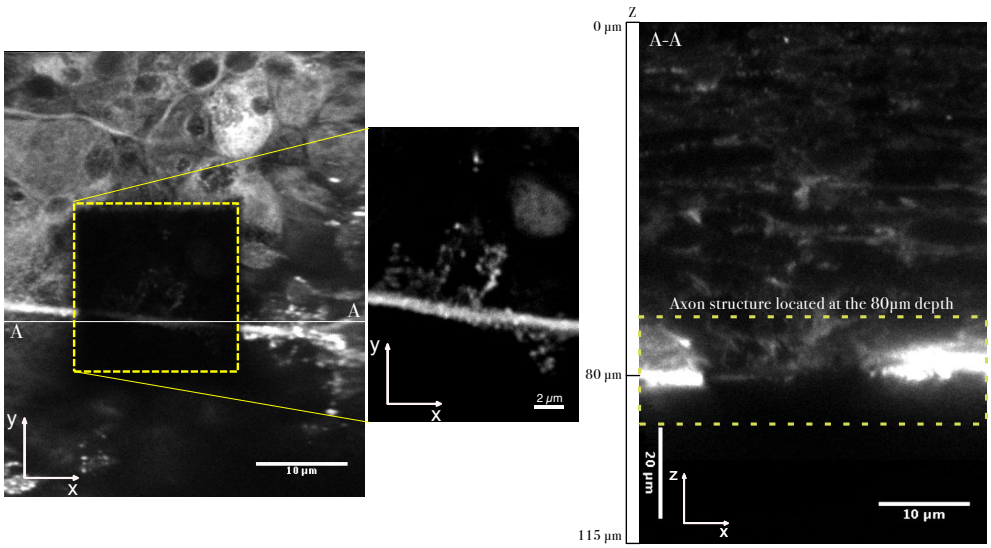

FIGURE 5.8: Image of the iPS cell tissue stack (left) and its XZ projection at A-A (right). Yellow dashed rectangle shows the location of the axon at the depth of approx. 80μm.

Acquisition parameters for Figure 5.8:

- primary antibodies: mouse Tuj-1
- secondary antibody: anti-mouse Abberior STAR 635P
- image size: 467 x 512 x 574 voxels
- voxel size: 100nm x 100nm x 200nm
- single frame acquisition time: 0.31s

As can be seen in the XZ cross-section A-A in the Figure 5.8, the axon grew at the depth of approximately 80µm. Both excitation and depletion beams need to pass through the tissue, which aberrates the wavefronts that propagate through it. In this case, aberration correction have been carried out, as without it, the quality of the image significantly dropped. Figure 5.9 shows the zoomed area that was bleached in the Figure 5.8. Both images were acquired using confocal imaging.

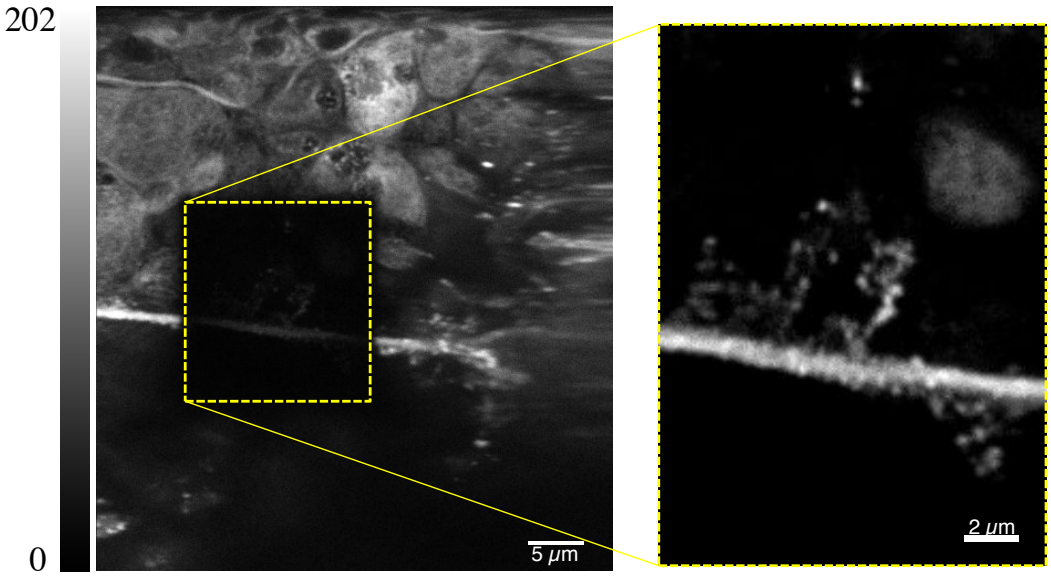

FIGURE 5.9: Large field of view (left) and zoomed area (right) shown with yellow dashed rectangle. The zoomed area shows the axon that was later imaged with different STED modes of the microscope. Both of the above images were acquired using confocal mode of the microscope.

Figure 5.10 shows the impact that aberration correction has when imaging highly scattering and aberrating samples. When no aberrations are corrected, the image loses contrast and resolution. There is a lot more background and a lot less signal. If the SLM is used to correct for aberrations only in the excitation beam, the image gains contrast and it has much higher resolution even compared to the 3D STED image when no corrections are done. In the 3D STED image with both excitation

and depletion beams corrected, the gain in the axial resolution is clearly seen. Acquisition parameters were as following:

- primary antibodies: mouse Tuj-1
- secondary antibody: anti-mouse Abberior STAR 635P
- image size: 720 x 744 x 120 voxels
- voxel size: 27nm x 27nm x 50nm
- single frame acquisition time: 21.7s

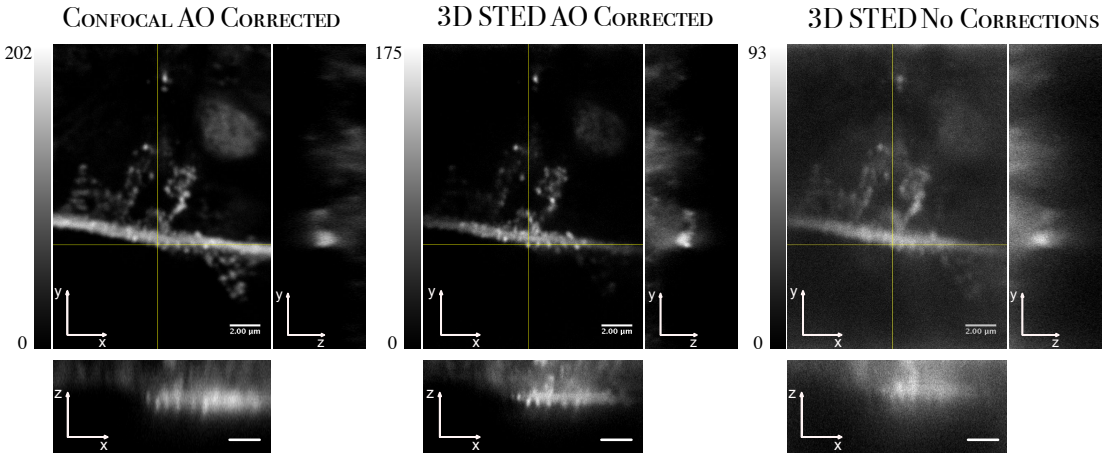

FIGURE 5.10: iPS cell axon imaged at the 80µm depth within tissue. *The Confocal AO corrected* image shows confocal image acquired with the aberration correction of the excitation beam, *3D STED AO Corrected* shows the super-resolution image acquired with 3D STED phase mask and for both excitation and depletion beams corrected for aberrations, *3D STED No Corrections* image show the image acquired with no corrections of excitation or depletion beams. Yellow lines on the XY images show the position at which the XZ and YZ cross-sections had been taken.

The images in Figure 5.10 confirm, that for the demanding samples, with structures that introduce significant aberrations, it would be impossible to use STED imaging without adaptive optics and aberration correction. It has been shown, that aberrations degrading 3D STED image quality introduced by highly aberrating specimens, such as Drosophila brain, can be corrected using AO, although up to date, the reported imaging depth did not exceed 15µm [158]. However, authors are expecting to reach much larger depths with well prepared sample and aberration correction.

As shown in Figure 5.10, it is indeed possible to obtain super resolution 3D STED images in aberrating specimens at depth reaching 80µm. Figure 5.11 shows the

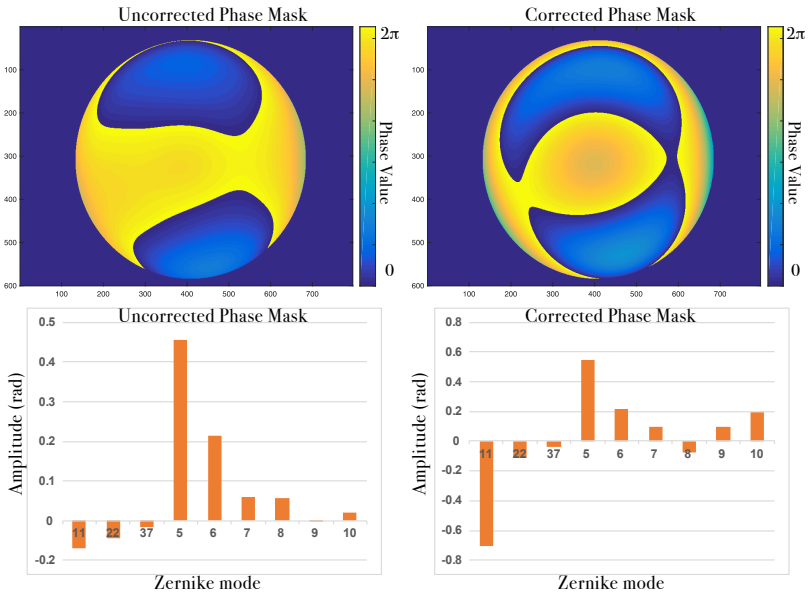

FIGURE 5.11: Phase applied to the depletion beam SLM and corresponding Zernike mode. Shown phase masks have been displayed on the SLM while acquiring images from Figure 5.10

values of corrected Zernike coefficients used for obtaining image from Figure 5.10, and the phase masks corresponding to the corrected Zernike polynomials. As expected, spherical aberration plays a critical role in the degradation of the depletion beam quality and resulting image.

Figure 5.12 shows the continuation of the axon shown in Figure 5.10 and the cell body it is attached to. Again, the zoomed area was imaged using confocal and 3D STED mode with and without aberration corrections.

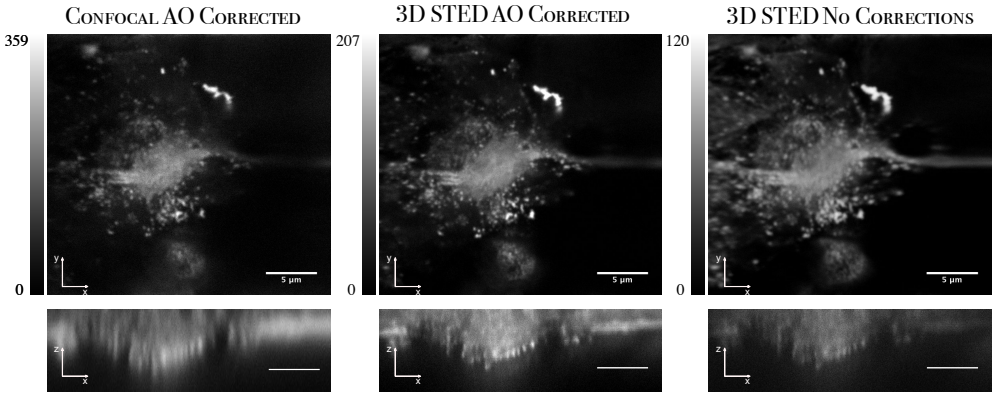

FIGURE 5.12: Image of the cell body of the same axon shown in the Figure 5.10. The zoomed area on the right was imaged using 3D STED mode of the microscope.

In images shown in Figure 5.13, we can see a comparison of the cell body shown in the Figure 5.12 and the effect aberration correction has on the quality of the

final image. Again, aberration correction was performed for both excitation and depletion beams. Acquisition parameters were as following:

- primary antibodies: mouse Tuj-1
- secondary antibody: anti-mouse Abberior STAR 635P
- image size: 1072 x 936 x 120 voxels
- voxel size: 27nm x 27nm x 50nm
- single frame acquisition time: 21.7s
- imaging depth: 80μm

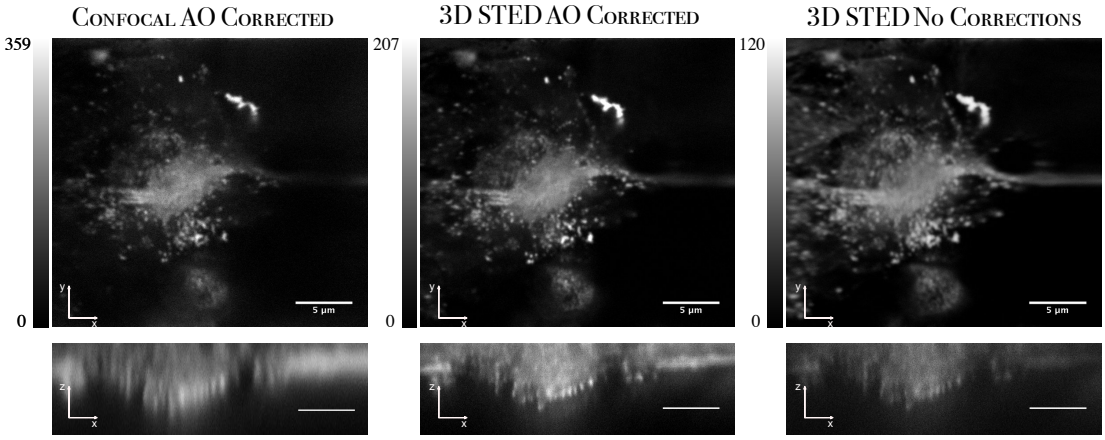

FIGURE 5.13: Image of the cell body of the same axon shown in the Figure 5.10. The zoomed area on the right was imaged using 3D STED mode of the microscope.

Results presented in the Figure 5.13 confirm, that when aberrations are not corrected, the resulting image is dimmer and has significantly lower resolution. Thanks to AO and aberration correction, it was possible to acquire a super-resolution image of the biological structure located deep inside aberrating tissue.
Taking into account the results obtained using designed STED microscope it is clear that it fulfils the purposes it was built for. The microscope was able to acquire super-resolution images with the sub-diffraction resolution both laterally and axially. I was able to increase lateral resolution up to 55nm and axial resolution up to 150nm. With proper sample preparation protocol, which was also established during this work, the microscope can successfully acquire super-resolution images of biological structures. Thanks to the application of the spatial light modulator it is possible to change depletion beam phase mask dynamically. Employment of indirect wavefront

modal sensing for aberration correction showed its power in imaging of samples inside thick layer of tissue. The results show that without SLM and aberration correction, it would be impossible to obtain 3D STED images of highly aberrating specimens.

Chapter 6

Conclusions and outlook.

6.1 Outlook

Even though it was shown that the STED microscope built here can be used to obtain 3D super-resolved images when imaging through thick samples, there is still room for improvements. In this chapter I will propose possible upgrades for the microscope.

6.1.1 Image deconvolution

STED microscopy is the only super-resolution technique that provides sub-diffraction images without the necessity of image reconstruction or processing. Yet, STED images can be further improved with the deconvolution algorithms. When we think about the resolution of the microscope as an ability of transferring the spatial frequencies (Section 1.2), diffraction limits the maximum cut-off frequency $k_{cut-off}$ that a classical microscope can transmit. All sample small details represented by the frequencies above $k_{cut-off}$ will not be resolvable by the microscope and will impose as blur in the acquired raw image. In STED microscopy, diffraction is not the factor that limits the maximum $k_{cut-off}$, hence theoretically all of the spatial frequencies of the imaged sample are transmitted by the microscope [181], [182]. Unfortunately, even though in STED microscopy diffraction is not a barrier, the factor that attenuates the frequencies that are effectively transmitted by the microscope is noise. Notably, the resolving power of the STED microscope can be described as the highest spatial frequency whose signal level is above the noise level. Increasing the intensity of the depletion beam increases the $k_{cut-off}$, but at the same time, with higher depletion beam intensity SNR decreases, mainly due to the photobleaching. What is more, increasing depletion beam intensity can lead to the photodamage in the sample. The noise can be reduced by increasing the acquisition time, but this leads to lower temporal resolution and longer sample exposure to the depletion beam. To help with these problems, the implementation of deconvolution algorithms for image restoration could potentially help uncover the information buried in the

noise. Effective STED deconvolution can lead to faster and much less invasive super-resolution imaging. There have been already some reports showing the STED image restoration using deconvolution algorithms [183], [184]
In order to take advantage of deconvolution algorithms, knowledge of the OTF or PSF is required. As shown in Figure 1.9, image formation through the optical system can be shown as a convolution of the object and the PSF of the imaging system. This means, that by knowing the PSF of the imaging system, we can do the inverse operation in order to find the more detailed representation of the object. This inverse operation is known as deconvolution. Graphically, deconvolution can be described as in Figure 6.1

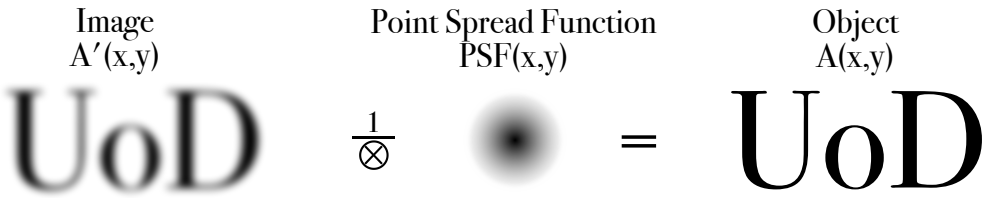

FIGURE 6.1: Graphical representation of the image deconvolution operation.

In STED microscopy, PSF/OTF does not solely depend on the optics of the microscope, but also on the parameters of the fluorescent dye used and sample conditions [182]. Due to that, PSF/OTF of the microscope should be extracted directly from the acquired image. I implemented the deconvolution algorithm described in [183], preliminary results showing maximum intensity projection (MIP) of bead images acquired with 2D STED phase mask are shown in Figure 6.2.
The acquisition parameters used for acquisition of the images in Figure 6.2 were:

- 23nm GattaBeads on the coverslip filled with Atto647N
- image size: 575 x 546 x 60 voxels
- voxel size: 18nm x 18nm x 50nm
- single frame acquisition time: 18s

Figure 6.3 presents the XY cross-section of the averaged bead from the Figure 6.2 and fitted Lorentzian curves.
According to the preliminary results, the FWHM of the acquired beads decreased from 71nm to 44nm. This gives very promising outcome and possible application to more images.

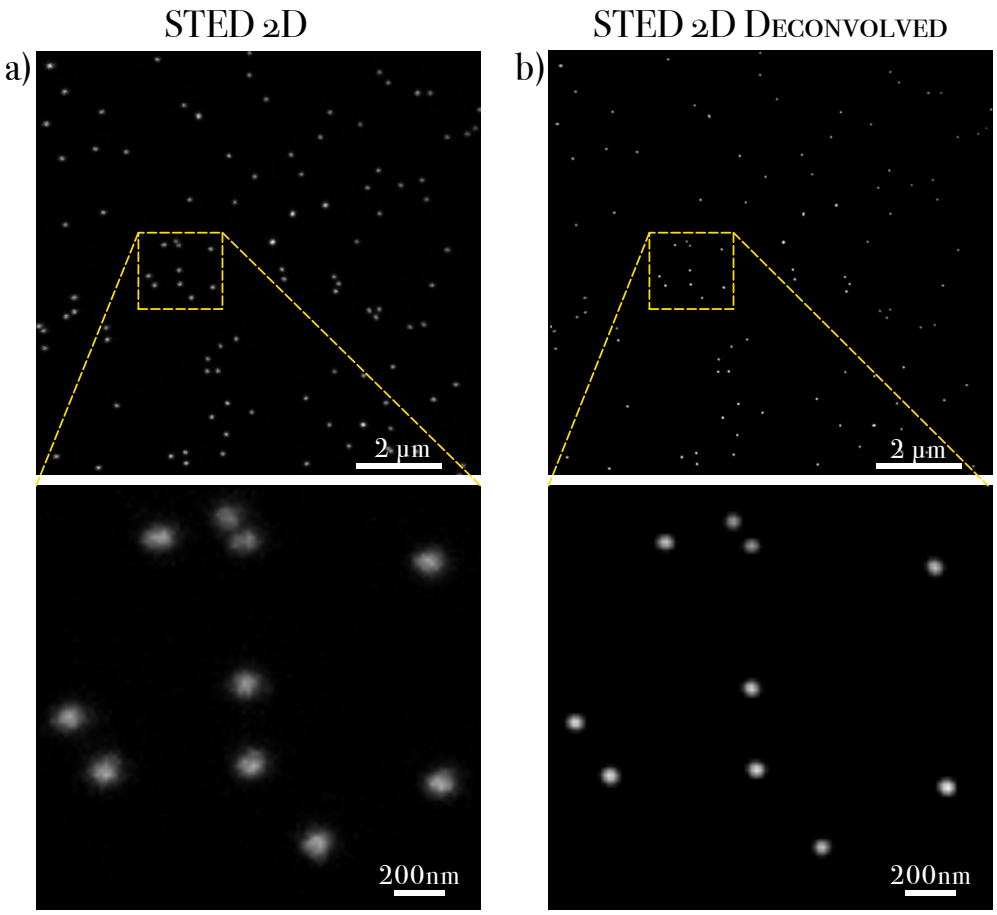

FIGURE 6.2: Bead images acquired with the STED2D phase mask with a) no deconvolution applied and b) deconvolved images. Images below a) and b) show the zoomed area marked with the yellow dashed rectangle.

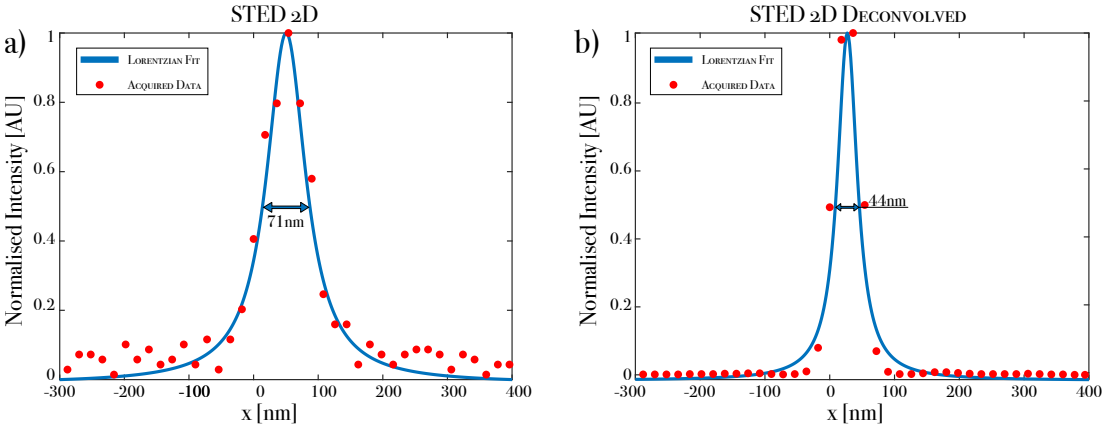

FIGURE 6.3: Plots and FWHM of the beads shown in Figure 6.2. a) shows the cross-section of the averaged bead for raw 2D STED image, b) shows the cross-section of the averaged bead for the deconvolved 2D STED image.

Deconvolved images increase the usually low signal to noise ratio of the raw STED data. It effectively increases the resolution of the image, without increasing the depletion beam power. Hence, deconvolution can lead to reduction of the sample exposure to the depletion beam and, as a result, reduce the photobleaching and phototoxicity effects. As mentioned before, the PSF of the STED microscope cannot be estimated by imaging the fluorescent beads and it has to be calculated from the image itself. This causes much more difficulties in applying correct deconvolution algorithm for raw STED images. A big improvement in the deconvolution process of STED data would be the implementation of blind or semi-blind deconvolution algorithms, that use image information to automatically estimate the PSF/OTF [185]–[187]. Unfortunately, up to date none of these algorithms has been successfully implemented in STED microscopy [182], [183].

6.1.2 Possible system upgrades

The proposed AO 3D STED microscope, even though its performance is very satisfying, can still be upgraded and improved. In this section I will try to write about possible upgrades that could improve the microscope performance.

Time-gating

For improving the resolution of the STED image, the intensity of the depletion beam has to be increased. It causes the reduction of the effective PSF of the microscope. Unfortunately, the increase of the depletion laser intensity causes the increased photobleaching of the fluorophores and strongly decreases the SNR of the acquired image. Thus it can be stated, that photobleaching and SNR is the limiting factor of the effective STED microscope resolution.
Photobleaching in the microscope can be reduced by one of the following strategies:

- using a fluorophore in which the absorption spectra does coincide with the wavelength of the depletion beam, or alternatively using a depletion beam wavelength at which the fluorophore does absorb the depletion beam [131], [137],
- fast scanning of the sample [188], [189] or reduction of the laser pulse repetition rate [116], [136], allowing the molecules to relax before the arrival of the next STED pulse,

- minimising the unnecessary illumination of the fluorophores, by using excitation and depletion beams only in the pixels corresponding to the sub-diffraction regions (RESCue [190]) or similarly, acquiring only a defined sub-diffraction area of interest in the sample (MINFIELD [191]. The combination of both RESCue and MINFIELD, DyMIN has also been reported [192]

- time-gating for efficient use of the long STED pulses that reduce the photobleaching of the sample [193]–[195]

The STED microscope system proposed in this work already takes advantage of the fast sample scanning with the resonant mirror and long STED pulses. Fluorophores are selected, so that the overlapping of the STED wavelength with the absorption spectra is minimal. The STED pulse width is at the sub-nanosecond region for further reduce of the photobleaching. However, with the increase of the STED pulse width, effective resolution is decreasing due to the lower fluorophore quenching [119], [127], [129]. As a result, the increase of the resolution comes with the cost of the increased photobleaching with short STED pulses and vice versa; and reduction of the photobleaching by stretching the STED pulse decreases the spatial resolution of the STED microscope. Fortunately, it has been shown that the application of time-gating can help maintain the resolution while widening the STED pulse [195]. Depletion efficiency of the depletion beam does not depend on the pulse width when the fluorescent photons are collected immediately after the arrival of the depletion pulse. In such case, the resolution is dependent on the average depletion beam intensity instead of the peak intensity [129]. Hence, time-gating can increase the depletion efficiency of the STED microscope.
In [195] the authors claim, that the application of time-gating allows the same comparative resolution and SNR for the 600ps depletion pulses as for 200ps pulses. Time-gating was achieved with the application of a gated photon counter with programmable width of the gating window developed by Boso *et al.* in [196]. The photon counter output was connected to a NI FPGA-based data acquisition card that carried out photon counting. The excitation laser was connected to the electronic pulse delay unit (MPD Picosecond Delayer), which triggered the photon counter.

Such an implementation should be possible in the STED system proposed in this thesis, as it also uses FPGA-based data acquisition and a single photon counting module possible of triggered detection. The system would require additional electronic delay unit for the fine adjustment of triggering gated detection, but apart from that it should be capable of time-gating with slight modification of the microscope control software.

Two-colour imaging

Even though the microscope developed in this thesis proved it is capable of acquiring dual-colour fluorescent imaging, it would require further investigation of the efficient fluorophores or addition of another excitation laser. Dual-colour results presented in the Chapter 5 showed, that for the used blue dye (Abberior STAR 470SXP) bleaching rate was too fast for obtaining high quality super-resolution STED images. The imaging should be tested for different dyes that can be excited with the 488nm laser and depleted with the 766nm laser, as those are already available in the system. Reports have shown, that alternatives to Abberior STAR470SXP exist and can be used in STED microscopes, such as Chromeo 494 [197] or Atto 490LS [198]. Alternatively, another laser with the wavelength of $590nm$, such as Picoquant LDH D-TA-595 could be applied. It has been reported, that the 590nm wavelength laser can be successfully used with the depletion laser wavelength of approximately 766nm and one of the following dyes: ATTO 590, ATTO 594, Abberior STAR580 [91], [194], [199]. With relatively low system changes, two-colour STED imaging could be improved in the existing setup.

Live-cell imaging

Thanks to the application of fast scanning resonant mirror and minimisation of the photobleaching, the setup should be capable of doing live cell imaging. Live cell STED microscopy has been reported in a number of papers up to date. The most common fluorescent markers for live cell imaging are fluorescent proteins [200], self-labelling protein tags, such as CLIP-, HALO- or SNAP- [197], [201]–[203], or ligand-coupled probes that bind to the targeted protein, such as silicone-rhodamine (SiR) [204], [205]. All of the mentioned dyes were successfully used for live cell imaging. The biggest problem of live cell imaging with STED is the phototoxicity due to the high intensity of the depletion laser. It is dependent on the illuminating wavelength of the laser. Far red wavelengths strongly decrease the phototoxicity compared to the ultraviolet light [206]. Due to that, there has been strong interest in development of far-red fluorescent markers. According to recent reports, SiR probes provide a very desired properties for live-cell STED imaging: it has high brightness, high labelling specificity and high stability [202].
SiR dyes are fully compatible with the excitation and depletion lasers spectra of the built STED microscope. With the addition of the environmental chamber that can sustain the life cycle of the cells, the system could be easily modified for life cell imaging.

6.2 Conclusions

The purpose of this work was to successfully build and use a super-resolution stimulated emission depletion fluorescent microscope, capable of imaging challenging samples with resolution exceeding capabilities of classical widefield or confocal systems. The goal of the project was successfully fulfilled and the results were described in previous chapters. I proposed an AO 3D STED system, that enabled super-resolution imaging of thick biological structures. In optical methods Chapter 2, I have written a detailed description of the microscope setup and the purpose of all elements. Built microscope exploits advanced devices such as spatial light modulators. SLMs enable imaging of complex structures, even when focusing through aberrating media. The performance of the microscope shown in Chapter 4 proved that the system has the means of imaging beyond the diffraction limit, demonstrating the resolution enhancement in both lateral and axial direction. I was able to obtain the resolution of 55nm laterally and 150nm axially, measured on the fluorescent beads samples.

Apart from being able to image test samples, in Chapter 5 I have shown that it is possible to use the microscope for imaging the biological structures. HeLa and RPE-1 cell samples were imaged. The system performed consistently whether it was imaging thin, $<4\mu$m microtubule structures in HeLa cells (Figure 5.1) or thicker $>10\mu$m RPE-1 cell mitotic spindle (Figure 5.2). The results obtained from imaging biological samples showed that the resolution surpassed the diffraction limit in all directions, and calculations shown that even for thick samples, $\approx$60nm lateral and $\approx$150nm axial resolution can be achieved.
However, the real strength and possibilities of the microscope unveiled when more challenging samples where used. iPS cells grow in a fairly random way, creating tissues in some areas, while other places remain tissue free. Tissue causes strong aberrations to the beam that propagates through them. Fortunately, thanks to the application of adaptive optics, I was able to correct the depletion and excitation beams, what resulted in much improved, more detailed images compared to the non-corrected images (Figure 5.10). When no AO correction was applied, the image resulted in much more blur and lower contrast. 3D resolution looked particularly good in the 3D STED image with AO correction.

Estimating the performance of the microscope and using it for imaging of thick, aberrating specimens, it can be claimed that the AO 3D STED microscope can provide data unavailable to other microscopes, especially diffraction limited systems. Without the AO correction, imaging deep, through the aberrating tissue would not

provide such a detailed results. When compared to the other works, 3D STED was only achieved at depths of <15μm [94], [157], [158]. When compared to 2D STED phase mask, 3D STED phase mask is even more sensitive to aberrations, hence it is crucial to use AO when imaging thick, >10μm samples. Shown in this work, 3D STED imaging proved to work even when focusing through 80μm thick tissue.

What is more, the benefits of having the custom built systems are that it can be adjusted for the end-user needs. As described in the Outlook 6.1 section, with little additional elements or modifications, the effective resolution could be increased with time gating, SNR can be raised with the deconvolution, dual-colour imaging has an enhancement potential and live-cell imaging can be introduced with the addition of environmental chamber. The proposed AO 3D STED microscope has shown it can successfully image thick samples with both axial and lateral sub-diffraction resolution as well as it showed the potential for further improvements. There are still a lot of areas that the microscope can be investigated and challenging samples that it can be used to possibly unveil new information about imaged structures.

Appendix A

Parts list table

TABLE A.1: Parts numbers and names used in the built STED microscope.

Name in Fig 2.1	**Part name**	**Part number**
637nm	Excitation laser head 637nm	PicoQuant LDH-P-C 640B
637nm	Excitation laser head driver	PicoQuant PDL 800-B
766nm	Depletion laser 766nm	PicoQuant VisIR 765 STED
APP	Anamorphic Prism Pair	Thorlabs PS873-A - N-KZFS8
FC	Coupling Lens f=15.29mm	Thorlabs C260TMD
PMF	Polarisation Maintaining Fibre	Thorlabs P5-630PMAR-2
M1-M6	Broadband Dielectric Mirrors	Semrock MI1050-SBB
f1	Molded glass aspheric lens, B-Coated, f = 11mm	Thorlabs A220TM-B
f2	Achromatic Double, B-Coated, f = 80mm	Thorlabs AC254-080-B-ML
f1'	Achromatic Double, B-Coated, f = 300mm	Thorlabs AC254-300-B-ML
f2'	Achromatic Double, B-Coated, f = 50mm	Thorlabs AC254-050-B-ML
f3	FC/PC 633nm Fiber collimation package, f = 10.99mm	Thorlabs F220FC-B
f4	Achromatic Double, A-Coated, f = 30mm	Thorlabs AC127-030-A-ML
f5	Achromatic Double, A-Coated, f = 50mm	Thorlabs AC254-050-A-ML
f6	VIS-NIR, Inked, Achromatic Lens, f = 400mm	Edmund Optics #49-369-INK

TABLE A.1: Parts numbers and names used in the built STED microscope.

Name in Fig 2.1	**Part name**	**Part number**
f7	VIS-NIR, Inked, Achromatic Lens, f = 200mm	Edmund Optics #49-364-INK
f8	VIS-NIR, Inked, Achromatic Lens, f = 60mm	Edmund Optics #49-357-INK
f9	VIS-NIR, Inked, Achromatic Lens, f = 50mm	Edmund Optics #49-356-INK
f10	VIS-NIR, Inked, Achromatic Lens, f = 38mm	Edmund Optics #49-788-INK
f11	VIS-NIR, Inked, Achromatic Lens, f = 300mm	Edmund Optics #49-368-INK
f12	VIS-NIR, Inked, Achromatic Lens, f = 200	Edmund Optics #49-364-INK
f_{if}	VIS-NIR, Inked, Achromatic Lens, f = 60mm	Edmund Optics #49-364-INK
f_{ir}	VIS-NIR, Inked, Achromatic Lens, f = 40mm	Edmund Optics #49-364-INK
MO	100x NA 1.45 Microscope Objective	Nikon CFI Plan Apo Lambda 100X Oil
SLM	Spatial Light Modulator	Hamamatsu X-10468-02
GLP	Glan Laser Polariser, B-Coated	Thorlabs GL10-B - Mounted
$\lambda/2$	Achromatic Half Wave Plate	Thorlabs AQWP05M-600
$\lambda/4$	Quarter Wave Plate	Thorlabs AHWP05M-600
GM	Galvanometer Mirror Pair	Scanlab DynAXIS XS
RM	Resonant Mirror	EOPC SC-30
Pellicle	8:92 Pellicle Beamsplitter	Thorlabs BP108
PHR	200µm Pinhole	Thorlabs P200S
PHF	50µm Pinhole	Thorlabs P50H
EF	Emission Filter	Semrock 676/37
DM1	Dichroic Mirror	Semrock FF720-SDi01
DM2	Dichroic Mirror	Chroma ZT647rdc-UF3
DM3	Dichroic Mirror	Chroma ZT561rdc-UF3

TABLE A.1: Parts numbers and names used in the built STED microscope.

Name in Fig 2.1	**Part name**	**Part number**
x-y motorised stage	XY closed loop flat top translation stage	ASI Imaging ASI S31121010FT
Z piezo stage	Complete nanopositioning system	Piezoconcept HS1.70
SPAD	Single Photon Avalanche Diode	Excelitas SPCM-780-13-FC
MPPC	Multi Pixel Photon Counter	Hamamatsu C13366

Appendix B

Matlab Code

```
clear all;
addpath('\MATLAB\efficient_subpixel_registration')
addpath('\MATLAB')
javaaddpath('\MATLAB\bfmatlab\bioformats_package.jar');
currentDirectory = pwd;
[upperPath, deepestFolder, ext] = fileparts(currentDirectory);
if isempty(ext) == 0
    deepestFolder = strcat(deepestFolder,ext);
end
selectROI = 1;

name_out_sum = strcat(currentDirectory,'\Rec_Sum');
name_out_avg = strcat(currentDirectory,'\Rec_Avg');

fileID = fopen('Params.txt');
formatSpec = ['X Step Size [um]: %f X Steps: %d'...
'Y Step Size [um]: %f Y Steps: %d Z Step Size [nm]: '...
'%f Z Slices: %d Number of line scans: '...
'%d Number of Frame Averages: '...
'%d Frame Acquisition time [ms]: %f'];

Params = textscan(fileID,formatSpec,...
                'Delimiter', '\n');


dx          = Params{1};    %% X pixel size [um]
imsizeX     = Params{2};    %% Number of X pixels
dy          = Params{3};    %% Y pixel size [um]
imsizeY     = Params{4};    %% Number of Y pixels
dz          = Params{5}/1000;    %% Z pixel size [um]
imsizeZ     = Params{6};    %% Number of Z stacks
exposure    = Params{9};

img_raw = zeros(imsizeY,imsizeX,imsizeZ,1,1,'uint16');
```

```
for ii=0:1:imsizeZ-1
%     tic
    disp(ii);
    name = strcat('_',int2str(ii),'.tiff');
    img_raw(:,:,ii+1,1,1) = (imread(name));
end

if selectROI == 1
MIP=max(img_raw,[],3);
S = [1 1 848 280];
figure(1), imagesc(MIP);
h = imrect(gca, S);
addNewPositionCallback(h,@(p) title(mat2str(p,3)));
fcn = makeConstrainToRectFcn('imrect',...
        get(gca,'XLim'),get(gca,'YLim'))
setPositionConstraintFcn(h,fcn)
position = wait(h);
position1 = round(position);
img_raw = img_raw(position1(2):position1(2)+position1(4)-1,...
          position1(1):position1(1)+position1(3)-1,:);
[imsizeY, imsizeX, imsizeZ] = size(img_raw);
close(figure(1));
end

metadata_raw = createMinimalOMEXMLMetadata(img_raw);
img_raw_XZ = zeros(imsizeZ,imsizeX,imsizeY,1,1,'uint16');
metadata_raw_XZ = createMinimalOMEXMLMetadata(img_raw_XZ);
img_raw_YZ = zeros(imsizeY,imsizeZ,imsizeX,1,1,'uint16');
metadata_raw_YZ = createMinimalOMEXMLMetadata(img_raw_YZ);

pixelSizeX = ome.units.quantity.Length(java.lang.Double(dx),...
             ome.units.UNITS.MICROMETER);
pixelSizeY = ome.units.quantity.Length(java.lang.Double(dy),...
              ome.units.UNITS.MICROMETER);
metadata_raw.setPixelsPhysicalSizeX(pixelSizeX, 0);
metadata_raw.setPixelsPhysicalSizeY(pixelSizeY, 0);
pixelSizeZ = ome.units.quantity.Length(java.lang.Double(dz),...
             ome.units.UNITS.MICROMETER);
metadata_raw.setPixelsPhysicalSizeZ(pixelSizeZ, 0);

metadata_raw_YZ.setPixelsPhysicalSizeX(pixelSizeZ, 0);
metadata_raw_YZ.setPixelsPhysicalSizeY(pixelSizeY, 0);
metadata_raw_YZ.setPixelsPhysicalSizeZ(pixelSizeX, 0);
```

```
metadata_raw_XZ.setPixelsPhysicalSizeX(pixelSizeX, 0);
metadata_raw_XZ.setPixelsPhysicalSizeY(pixelSizeZ, 0);
metadata_raw_XZ.setPixelsPhysicalSizeZ(pixelSizeY, 0);


img_rec_avg = zeros(imsizeY,round(imsizeX/2),...
                imsizeZ,1,1,'uint16');
metadata_rec_avg = createMinimalOMEXMLMetadata(img_rec_avg);

img_rec_avg_XZ = zeros(imsizeZ,round(imsizeX/2),...
                imsizeY,1,1,'uint16');
metadata_rec_avg_XZ = createMinimalOMEXMLMetadata(img_rec_avg_XZ);

img_rec_avg_YZ = zeros(imsizeY,imsizeZ,...
                  round(imsizeX/2),1,1,'uint16');
metadata_rec_avg_YZ = createMinimalOMEXMLMetadata(img_rec_avg_YZ);

metadata_rec_avg.setPixelsPhysicalSizeX(pixelSizeX, 0);
metadata_rec_avg.setPixelsPhysicalSizeY(pixelSizeY, 0);
metadata_rec_avg.setPixelsPhysicalSizeZ(pixelSizeZ, 0);

metadata_rec_avg_YZ.setPixelsPhysicalSizeX(pixelSizeZ, 0);
metadata_rec_avg_YZ.setPixelsPhysicalSizeY(pixelSizeY, 0);
metadata_rec_avg_YZ.setPixelsPhysicalSizeZ(pixelSizeX, 0);

metadata_rec_avg_XZ.setPixelsPhysicalSizeX(pixelSizeX, 0);
metadata_rec_avg_XZ.setPixelsPhysicalSizeY(pixelSizeZ, 0);
metadata_rec_avg_XZ.setPixelsPhysicalSizeZ(pixelSizeY, 0);


img_rec_sum = zeros(imsizeY,round(imsizeX/2),...
                imsizeZ,1,1,'uint16');
metadata_rec_sum = createMinimalOMEXMLMetadata(img_rec_sum,'XYZCT');

img_rec_sum_XZ = zeros(imsizeZ,round(imsizeX/2),...
                imsizeY,1,1,'uint16');
metadata_rec_sum_XZ = createMinimalOMEXMLMetadata(img_rec_sum_XZ);

img_rec_sum_YZ = zeros(imsizeY,imsizeZ,...
                round(imsizeX/2),1,1,'uint16');
metadata_rec_sum_YZ = createMinimalOMEXMLMetadata(img_rec_sum_YZ);

metadata_rec_sum.setPixelsPhysicalSizeX(pixelSizeX, 0);
```

```
metadata_rec_sum.setPixelsPhysicalSizeY(pixelSizeY, 0);
metadata_rec_sum.setPixelsPhysicalSizeZ(pixelSizeZ, 0);

metadata_rec_sum_YZ.setPixelsPhysicalSizeX(pixelSizeZ, 0);
metadata_rec_sum_YZ.setPixelsPhysicalSizeY(pixelSizeY, 0);
metadata_rec_sum_YZ.setPixelsPhysicalSizeZ(pixelSizeX, 0);

metadata_rec_sum_XZ.setPixelsPhysicalSizeX(pixelSizeX, 0);
metadata_rec_sum_XZ.setPixelsPhysicalSizeY(pixelSizeZ, 0);
metadata_rec_sum_XZ.setPixelsPhysicalSizeZ(pixelSizeY, 0);

for ii=0:1:imsizeZ-1
disp(ii);
name = strcat('_',int2str(ii),'.tiff');
img = gpuArray(double(img_raw(:,:,ii+1,1,1)));
img1 = img(:,1:round(imsizeX/2));
img2 = img(:,round(imsizeX/2)+1:end);
img2 = fliplr(img2);
[output Greg] = dftregistration(fft2(img1),fft2(img2),100);
img_rec_avg(:,:,ii+1) = uint16(gather((img1+real(ifft2(Greg)))/2));
img_rec_sum(:,:,ii+1) = uint16(gather(img1+real(ifft2(Greg))));
end

img_raw_XZ = permute(img_raw,[3 2 1]);
img_raw_YZ = permute(img_raw,[1 3 2]);
img_rec_avg_XZ = permute(img_rec_avg,[3 2 1]);
img_rec_avg_YZ = permute(img_rec_avg,[1 3 2]);
img_rec_sum_XZ = permute(img_rec_sum,[3 2 1]);
img_rec_sum_YZ = permute(img_rec_sum,[1 3 2]);

disp(strcat('Saving',32, upperPath,'\',deepestFolder,...
      '_Raw','.ome.tif'));
bfsave(img_raw, strcat(upperPath,'\',deepestFolder,...
       '_Raw','.ome.tiff'), 'metadata', metadata_raw);
disp(strcat('Saving',32, upperPath,'\',deepestFolder,...
       '_Rec_Sum','.ome.tiff'));
bfsave(img_rec_sum, strcat(upperPath,'\',deepestFolder,...
       '_Rec_Sum','.ome.tiff'), 'metadata', metadata_rec_sum);
disp(strcat('Saving',32,upperPath,'\',deepestFolder,...
       '_Rec_Avg','.ome.tiff'));
bfsave(img_rec_avg, strcat(upperPath,'\',deepestFolder,...
       '_Rec_Avg','.ome.tiff'), 'metadata', metadata_rec_avg);
```

```
disp(strcat('Saving',32, upperPath,'\',deepestFolder,...
  '_Rec_Sum_XZ','.ome.tiff'));
bfsave(img_rec_sum_XZ, strcat(upperPath,'\',deepestFolder,...
  '_Rec_Sum_XZ','.ome.tiff'), 'metadata', metadata_rec_sum_XZ);
disp(strcat('Saving',32, upperPath,'\',deepestFolder,...
  '_Rec_Avg_XZ','.ome.tiff'));
bfsave(img_rec_avg_XZ, strcat(upperPath,'\',deepestFolder,...
  '_Rec_Avg_XZ','.ome.tiff'), 'metadata', metadata_rec_avg_XZ);

disp(strcat('Saving',32, upperPath,'\',deepestFolder,...
  '_Rec_Sum_YZ','.ome.tiff'));
bfsave(img_rec_sum_YZ, strcat(upperPath,'\',deepestFolder,...
  '_Rec_Sum_YZ','.ome.tiff'), 'metadata', metadata_rec_sum_YZ);
disp(strcat('Saving',32, upperPath,'\',deepestFolder,...
  '_Rec_Avg_YZ','.ome.tiff'));
bfsave(img_rec_avg_YZ, strcat(upperPath,'\',deepestFolder,...
  '_Rec_Avg_YZ','.ome.tiff'), 'metadata', metadata_rec_avg_YZ);
```

Bibliography

[1] H. Siedentopf and R. Zsigmondy, "Uber Sichtbarmachung und Größenbestimmung ultramikoskopischer Teilchen, mit besonderer Anwendung auf Goldrubingläser", *Annalen der Physik*, vol. 315, no. 1, pp. 1–39, 1902, ISSN: 00033804. DOI: 10.1002/andp.19023150102.

[2] U. Kubitscheck, *Fluorescence Microscopy From Principles to Biological Applications*. John Wiley & Sons, 2013, p. 400, ISBN: 9780470648476.

[3] F. Zernike, "Phase contrast, a new method for the microscopic observation of transparent objects", *Physica*, vol. 9, no. 10, pp. 974–986, Jul. 1942, ISSN: 00318914. DOI: 10.1016/S0031-8914(42)80079-8.

[4] R. D. Allen, G. B. David, and G Nomarski, "The zeiss-Nomarski differential interference equipment for transmitted-light microscopy.", *Zeitschrift für wissenschaftliche Mikroskopie und mikroskopische Technik*, vol. 69, no. 4, pp. 193–221, Nov. 1969, ISSN: 0373-031X.

[5] A. Jablonski, "Efficiency of Anti-Stokes Fluorescence in Dyes", *Nature*, vol. 131, no. 3319, pp. 839–840, Jun. 1933, ISSN: 0028-0836. DOI: 10.1038/131839b0.

[6] B. E. A. Saleh and M. C. Teich, *Fundamentals of Photonics*, Second, ser. Wiley Series in Pure and Applied Optics. Hoboken, New Jersey: John Wiley & Sons, Inc., 2007, ISBN: 978-0-471-35832-9.

[7] M Minsky, "Microscopy Apparatus", *US Patent 3013467*, vol. 3013467, no. 3013467, p. 5, Dec. 1957. DOI: US3013467A.

[8] M. Minsky, "Memoir on inventing the confocal scanning microscope", *Scanning*, vol. 10, no. 4, pp. 128–138, Jan. 1988, ISSN: 01610457. DOI: 10.1002/sca.4950100403.

[9] J. B. Pawley, *Handbook Of Biological Confocal Microscopy*, J. B. Pawley, Ed. Boston, MA: Springer US, 2006, ISBN: 978-0-387-25921-5. DOI: 10.1007/978-0-387-45524-2.

[10] E. Abbe, "Beiträge zur Theorie des Mikroskops und der mikroskopischen Wahrnehmung", *Archiv für Mikroskopische Anatomie*, vol. 9, no. 1, pp. 413–418, Dec. 1873, ISSN: 0176-7364. DOI: 10.1007/BF02956173.

[11] H. Gross, W. Singer, and M. Totzeck, *Handbook of Optical Systems Volume 2: Physical Image Formation*, H. Gross, W. Singer, and M. Totzeck, Eds. Weinheim, FRG: Wiley-VCH Verlag GmbH & Co. KGaA, Jul. 2005, vol. 2, pp. 1–690, ISBN: 9783527606689. DOI: 10.1002/3527606688.

[12] U. Kubitscheck, *Fluorescence microscopy : from principles to biological applications*. 2017, vol. Chapter 4, p. 504, ISBN: 9783527338375. DOI: 10.1002/9783527650002.ch11.

[13] G. B. Airy, "On the Diffraction of an Object-glass with a Circular Aperture", *Transactions of the Cambridge Philosophical Society*, vol. 5, no. August, pp. 283–291, 1834, ISSN: 1050-0529.

[14] L. RAYLEIGH, "On the Theory of Optical Images, with Special Reference to the Microscope", *Journal of the Royal Microscopical Society*, vol. 23, no. 4, pp. 447–473, Aug. 1903, ISSN: 03683974. DOI: 10.1111/j.1365-2818.1903.tb04830.x.

[15] J. W. Goodman, *Introduction To Fourier Optics*, ser. McGraw-Hill physical and quantum electronics series. Roberts & Company Publishers, 2005, ISBN: 9780974707723.

[16] H. Köhler, "On Abbe's theory of image formation in the microscope", *Optica Acta*, vol. 28, no. 12, pp. 1691–1701, 1981, ISSN: 00303909. DOI: 10.1080/713820514.

[17] O. T. Koppius, E. L. Cleveland, E. L. Cleveland, and B. P. Ramsay, "Criteria and the Intensity-Epoch Slope", pp. 26–33, 1941. DOI: 10.1364/JOSA.31.000026.

[18] M. Born and E. Wolf, *Principles of optics: Electromagnetic Theory of Propagation, Interference and Diffraction of Light*. Cambridge University Press, 1994, pp. 1–952, ISBN: 0521642221. DOI: 10.1016/S0030-3992(00)00061-X.

[19] H. T. M. Voort and G. J. Brakenhoff, "3-D image formation in high-aperture fluorescence confocal microscopy: a numerical analysis", *Journal of Microscopy*, vol. 158, no. 1, pp. 43–54, Apr. 1990, ISSN: 00222720. DOI: 10.1111/j.1365-2818.1990.tb02975.x.

[20] R. P. Feynman, "There's Plenty of Room at the Bottom", *Journal of Microeleciromechanical Systems*, vol. 1, no. 1, pp. 60–66, 1992, ISSN: 10577157. DOI: 10.1109/84.128057.

[21] G. T. Di Francia, "Super-gain antennas and optical resolving power", *Il Nuovo Cimento*, vol. 9, no. 3 Supplement, pp. 426–438, 1952, ISSN: 00296341. DOI: 10.1007/BF02903413.

[22] F. M. Huang and N. I. Zheludev, "Super-resolution without evanescent waves", *Nano Letters*, vol. 9, no. 3, pp. 1249–1254, 2009, ISSN: 15306984. DOI: 10.1021/nl9002014.

[23] J. Bechhoefer, "What is superresolution microscopy?", vol. 22, 2014, ISSN: 0002-9505. DOI: 10.1119/1.4900756.

[24] B. B. Fultz and J. M. Howe, *Transmission electron microscopy and diffractometry of materials*. Springer, 2008, p. 758, ISBN: 9783540738855.

[25] M. Knoll and E. Ruska, "Das Elektronenmikroskop", *Zeitschrift fur Physik*, vol. 78, no. 5-6, pp. 318–339, May 1932, ISSN: 14394413. DOI: 10.1007/BF01342199.

[26] A. Bogner, P. H. Jouneau, G. Thollet, D. Basset, and C. Gauthier, "A history of scanning electron microscopy developments: Towards "wet-STEM" imaging", *Micron*, vol. 38, no. 4, pp. 390–401, 2007, ISSN: 09684328. DOI: 10.1016/j.micron.2006.06.008.

[27] J. Rouquette, C. Cremer, T. Cremer, and S. Fakan, *Functional nuclear architecture studied by microscopy: Present and future*, 1st ed., C. Elsevier Inc., 2010, vol. 282, pp. 1–90, ISBN: 9780123812568. DOI: 10.1016/S1937-6448(10)82001-5.

[28] A. L. Olins, M. B. Senior, and D. E. Olins, "Ultrastructural features of chromatin ν bodies", *Journal of Cell Biology*, vol. 68, no. 3, pp. 787–793, 1976, ISSN: 00219525.

[29] S. y. Takemura, Y. Aso, T. Hige, A. Wong, Z. Lu, C. S. Xu, P. K. Rivlin, H. Hess, T. Zhao, T. Parag, S. Berg, G. Huang, W. Katz, D. J. Olbris, S. Plaza, L. Umayam, R. Aniceto, L. A. Chang, S. Lauchie, O. Ogundeyi, C. Ordish, A. Shinomiya, C. Sigmund, S. Takemura, J. Tran, G. C. Turner, G. M. Rubin, and L. K. Scheffer, "A connectome of a learning and memory center in the adult Drosophila brain", *ELife*, vol. 6, pp. 1–43, 2017, ISSN: 2050084X. DOI: 10.7554/eLife.26975.

[30] K. Eichler, F. Li, A. Litwin-Kumar, Y. Park, I. Andrade, C. M. Schneider-Mizell, T. Saumweber, A. Huser, C. Eschbach, B. Gerber, R. D. Fetter, J. W. Truman, C. E. Priebe, L. F. Abbott, A. S. Thum, M. Zlatic, and A. Cardona, "The complete connectome of a learning and memory centre in an insect brain", *Nature*, vol. 548, no. 7666, pp. 175–182, 2017, ISSN: 14764687. DOI: 10.1038/nature23455.

[31] R. Erni, M. D. Rossell, C. Kisielowski, and U. Dahmen, "Atomic-resolution imaging with a sub-50-pm electron probe", *Physical Review Letters*, vol. 102, no. 9, pp. 1–4, 2009, ISSN: 00319007. DOI: 10.1103/PhysRevLett.102.096101.

[32] R. F.E. C. Klomparens and K. L., "Artifacts in Biological Electron Microscopy.", *Science (New York, N.Y.)*, vol. 242, no. 4876, p. 309, Oct. 1988, ISSN: 0036-8075. DOI: 10.1126/science.242.4876.309.

[33] S. W. Hell and J Wichmann, "Breaking the diffraction resolution limit by stimulated emission: stimulated-emission-depletion fluorescence microscopy.", *Optics letters*, vol. 19, no. 11, pp. 780–2, Jun. 1994, ISSN: 0146-9592.

[34] E. Betzig, G. H. Patterson, R. Sougrat, O. W. Lindwasser, S. Olenych, J. S. Bonifacino, M. W. Davidson, J. Lippincott-Schwartz, and H. F. Hess, "Imaging intracellular fluorescent proteins at nanometer resolution", *Science*, vol. 313, no. 5793, pp. 1642–1645, 2006, ISSN: 00368075. DOI: 10.1126/science.1127344.

[35] H. Shroff, C. G. Galbraith, J. A. Galbraith, H. White, J. Gillette, S. Olenych, M. W. Davidson, and E. Betzig, "Dual-color superresolution imaging of genetically expressed probes within individual adhesion complexes.", *Proceedings of the National Academy of Sciences of the United States of America*, vol. 104, no. 51, pp. 20 308–13, Dec. 2007, ISSN: 1091-6490. DOI: 10.1073/pnas.0710517105.

[36] S. T. Hess, T. P. Girirajan, and M. D. Mason, "Ultra-High Resolution Imaging by Fluorescence Photoactivation Localization Microscopy", *Biophysical Journal*, vol. 91, no. 11, pp. 4258–4272, Dec. 2006, ISSN: 00063495. DOI: 10.1529/biophysj.106.091116.

[37] S. T. Hess, T. J. Gould, M. V. Gudheti, S. A. Maas, K. D. Mills, and J. Zimmerberg, "Dynamic clustered distribution of hemagglutinin resolved at 40 nm in living cell membranes discriminates between raft theories", *Proceedings*

of the National Academy of Sciences, vol. 104, no. 44, pp. 17 370–17 375, Oct. 2007, ISSN: 0027-8424. DOI: 10.1073/pnas.0708066104.

[38] M. J. Rust, M. Bates, and X. Zhuang, "Sub-Diffraction-Limit Imaging by Stochastic Optical Reconstruction Microscopy (STORM)", *Nature Methods*, vol. 3, no. 10, pp. 793–795, Oct. 2006, ISSN: 1548-7091.

[39] M. Bates, B. Huang, G. T. Dempsey, and X. Zhuang, "Multicolor super-resolution imaging with photo-switchable fluorescent probes", *Science*, vol. 317, no. 5845, pp. 1749–1753, Sep. 2007, ISSN: 00368075. DOI: 10.1126/science.1146598.

[40] M. Heilemann, S. van-de-Linde, M. Schüttpelz, R. Kasper, B. Seefeldt, A. Mukherjee, P. Tinnefeld, and M. Sauer, "Subdiffraction-Resolution Fluorescence Imaging with Conventional Fluorescent Probes", *Angewandte Chemie International Edition*, vol. 47, no. 33, pp. 6172–6176, Aug. 2008, ISSN: 14337851. DOI: 10.1002/anie.200802376.

[41] S. van de Linde, A. Löschberger, T. Klein, M. Heidbreder, S. Wolter, M. Heilemann, and M. Sauer, "Direct stochastic optical reconstruction microscopy with standard fluorescent probes", *Nature Protocols*, vol. 6, no. 7, pp. 991–1009, Jun. 2011, ISSN: 1754-2189. DOI: 10.1038/nprot.2011.336.

[42] M. Hofmann, C. Eggeling, S. Jakobs, and S. W. Hell, "Breaking the diffraction barrier in fluorescence microscopy at low light intensities by using reversibly photoswitchable proteins.", *Proceedings of the National Academy of Sciences of the United States of America*, vol. 102, no. 49, pp. 17 565–17 569, 2005, ISSN: 0027-8424. DOI: 10.1073/pnas.0506010102.

[43] J. Fölling, M. Bossi, H. Bock, R. Medda, C. A. Wurm, B. Hein, S. Jakobs, C. Eggeling, and S. W. Hell, "Fluorescence nanoscopy by ground-state depletion and single-molecule return", *Nature Methods*, vol. 5, no. 11, pp. 943–945, Nov. 2008, ISSN: 15487091. DOI: 10.1038/nmeth.1257.

[44] B. Lalkens, I. Testa, K. I. Willig, and S. W. Hell, "MRT letter: Nanoscopy of protein colocalization in living cells by STED and GSDIM.", *Microscopy research and technique*, vol. 75, no. 1, pp. 1–6, Jan. 2012, ISSN: 1097-0029. DOI: 10.1002/jemt.21026.

[45] R. T. Borlinghaus, "STED and GSDIM : Diffraction Unlimited Resolution for all Types of Fluorescence Imaging", no. 4, pp. 848–854, 2012.

[46] M. G. Gustafsson, "Surpassing the lateral resolution limit by a factor of two using structured illumination microscopy.", *Journal of microscopy*, vol. 198, no. Pt 2, pp. 82–87, 2000, ISSN: 0022-2720. DOI: 10.1046/j.1365-2818.2000.00710.x.

[47] M. G. L. Gustafsson, "Nonlinear structured-illumination microscopy : Wide-field fluorescence imaging with theoretically unlimited resolution", vol. 102, no. 37, pp. 13 081–13 086, 2005.

[48] S. W. Hell, "Nanoscopy with focused light", *Nobel Lecture*, vol. 527, no. 7-8, pp. 423–445, 2014, ISSN: 15213889. DOI: 10.1002/andp.201500805.

[49] E. Betzig, "Single Molecules, Cells, and Super-Resolution Optics", *Nobel Lecture*, pp. 111–137, 2014.

[50] W. E. Moerner, "Single-Molecule Spectroscopy, Imaging,and Photocontrol : Foundations for Super-Resolution Microscopy", *Nobel Lecture*, vol. l, pp. 205–257, 2014.

[51] C. G. Galbraith and J. A. Galbraith, "Super-resolution microscopy at a glance", *Journal of Cell Science*, vol. 124, no. 10, pp. 1607–1611, 2011, ISSN: 0021-9533. DOI: 10.1242/jcs.080085.

[52] S. J. Sahl, S. W. Hell, and S. Jakobs, "Fluorescence nanoscopy in cell biology", *Nature Reviews Molecular Cell Biology*, vol. 18, no. 11, pp. 685–701, 2017, ISSN: 14710080. DOI: 10.1038/nrm.2017.71.

[53] C. A. Combs and H. Shroff, "Fluorescence microscopy: A concise guide to current imaging methods", *Current Protocols in Neuroscience*, vol. 2017, no. April, pp. 1–2, 2017, ISSN: 19348576. DOI: 10.1002/cpns.29.

[54] J. Huff, A. Bergter, J. Birkenbeil, I. Kleppe, and R. Engelmann, "The new 2D Superresolution mode for ZEISS Airyscan", *Nature Methods*, vol. 14, no. 12, pp. iv–vi, 2017, ISSN: 1548-7091. DOI: 10.1038/nmeth.f.403.

[55] R. E. Thompson, D. R. Larson, and W. W. Webb, "Precise nanometer localization analysis for individual fluorescent probes.", *Biophysical journal*, vol. 82, no. 5, pp. 2775–83, May 2002, ISSN: 0006-3495. DOI: 10.1016/S0006-3495(02)75618-X.

[56] A. Yildiz, J. N. Forkey, S. A. McKinney, T. Ha, Y. E. Goldman, and P. R. Selvin, "Myosin V walks hand-over-hand: Single fluorophore imaging with 1.5-nm localization", *Science*, vol. 300, no. 5628, pp. 2061–2065, Jun. 2003, ISSN: 00368075. DOI: 10.1126/science.1084398.

[57] B. Huang, H. Babcock, and X. Zhuang, "Breaking the diffraction barrier: Super-resolution imaging of cells", *Cell*, vol. 143, no. 7, pp. 1047–1058, 2010, ISSN: 00928674. DOI: 10.1016/j.cell.2010.12.002.

[58] G. Giannone, E. Hosy, F. Levet, A. Constals, K. Schulze, A. I. Sobolevsky, M. P. Rosconi, E. Gouaux, R. Tampé, D. Choquet, and L. Cognet, "Dynamic superresolution imaging of endogenous proteins on living cells at ultra-high density.", *Biophysical journal*, vol. 99, no. 4, pp. 1303–10, Aug. 2010, ISSN: 1542-0086. DOI: 10.1016/j.bpj.2010.06.005.

[59] M. Andresen, A. C. Stiel, J. Fölling, D. Wenzel, A. Schönle, A. Egner, C. Eggeling, S. W. Hell, and S. Jakobs, "Photoswitchable fluorescent proteins enable monochromatic multilabel imaging and dual color fluorescence nanoscopy", *Nature Biotechnology*, vol. 26, no. 9, pp. 1035–1040, Sep. 2008, ISSN: 1087-0156. DOI: 10.1038/nbt.1493.

[60] H. Bock, C. Geisler, C. Wurm, C. von Middendorff, S. Jakobs, A. Schönle, A. Egner, S. W. Hell, and C. Eggeling, "Two-color far-field fluorescence nanoscopy based on photoswitchable emitters", *Applied Physics B*, vol. 88, no. 2, pp. 161–165, Jul. 2007, ISSN: 0946-2171. DOI: 10.1007/s00340-007-2729-0.

[61] A. Schönle and S. W. Hell, "Fluorescence nanoscopy goes multicolor", *Nature Biotechnology*, vol. 25, no. 11, pp. 1234–1235, Nov. 2007, ISSN: 1087-0156. DOI: 10.1038/nbt1107-1234.

[62] S. van de Linde, U. Endesfelder, A. Mukherjee, M. Schüttpelz, G. Wiebusch, S. Wolter, M. Heilemann, and M. Sauer, "Multicolor photoswitching microscopy for subdiffraction-resolution fluorescence imaging", *Photochemical & Photobiological Sciences*, vol. 8, no. 4, p. 465, Mar. 2009, ISSN: 1474-905X. DOI: 10.1039/b822533h.

[63] B. Huang, W. Wang, M. Bates, and X. Zhuang, "Three-dimensional super-resolution imaging by stochastic optical reconstruction microscopy", *Science*, vol. 319, no. 5864, pp. 810–813, Feb. 2008, ISSN: 00368075. DOI: 10.1126/science.1153529.

[64] S. R. P. Pavani, M. A. Thompson, J. S. Biteen, S. J. Lord, N. Liu, R. J. Twieg, R. Piestun, and W. E. Moerner, "Three-dimensional, single-molecule fluorescence imaging beyond the diffraction limit by using a double-helix point spread function.", *Proceedings of the National Academy of Sciences of the*

United States of America, vol. 106, no. 9, pp. 2995–9, Mar. 2009, ISSN: 1091-6490. DOI: 10.1073/pnas.0900245106.

[65] G. Shtengel, J. A. Galbraith, C. G. Galbraith, J. Lippincott-Schwartz, J. M. Gillette, S. Manley, R. Sougrat, C. M. Waterman, P. Kanchanawong, M. W. Davidson, R. D. Fetter, and H. F. Hess, "Interferometric fluorescent super-resolution microscopy resolves 3D cellular ultrastructure.", *Proceedings of the National Academy of Sciences of the United States of America*, vol. 106, no. 9, pp. 3125–30, Mar. 2009, ISSN: 1091-6490. DOI: 10.1073/pnas.0813131106.

[66] C. Shannon, "Communication in the Presence of Noise", *Proceedings of the IRE*, vol. 37, no. 1, pp. 10–21, Jan. 1949, ISSN: 0096-8390. DOI: 10.1109/JRPROC.1949.232969.

[67] W. R. Legant, L. Shao, J. B. Grimm, T. A. Brown, D. E. Milkie, B. B. Avants, L. D. Lavis, and E. Betzig, "High-density three-dimensional localization microscopy across large volumes", *Nature Methods*, vol. 13, no. 4, pp. 359–365, Apr. 2016, ISSN: 1548-7091. DOI: 10.1038/nmeth.3797.

[68] J. Demmerle, E. Wegel, L. Schermelleh, and I. M. Dobbie, "Assessing resolution in super-resolution imaging", *Methods*, vol. 88, pp. 3–10, Oct. 2015, ISSN: 10462023. DOI: 10.1016/j.ymeth.2015.07.001.

[69] T. J. Lambert and J. C. Waters, "Navigating challenges in the application of superresolution microscopy", *The Journal of Cell Biology*, pp. 1–11, 2016, ISSN: 0021-9525. DOI: 10.1083/jcb.201610011.

[70] A. Sharonov and R. M. Hochstrasser, "Wide-field subdiffraction imaging by accumulated binding of diffusing probes.", *Proceedings of the National Academy of Sciences of the United States of America*, vol. 103, no. 50, pp. 18 911–6, Dec. 2006, ISSN: 0027-8424. DOI: 10.1073/pnas.0609643104.

[71] M. G. Gustafsson, L. Shao, P. M. Carlton, C. J. R. Wang, I. N. Golubovskaya, W. Z. Cande, D. A. Agard, and J. W. Sedat, "Three-Dimensional Resolution Doubling in Wide-Field Fluorescence Microscopy by Structured Illumination", *Biophysical Journal*, vol. 94, no. 12, pp. 4957–4970, Jun. 2008, ISSN: 0006-3495. DOI: 10.1529/BIOPHYSJ.107.120345.

[72] J. R. Allen, S. T. Ross, and M. W. Davidson, "Structured illumination microscopy for superresolution", *ChemPhysChem*, vol. 15, no. 4, pp. 566–576, 2014, ISSN: 14397641. DOI: 10.1002/cphc.201301086.

[73] K. Patorski, *Handbook of the moiré fringe technique*. Elsevier, 1993, xix, 431 p. ISBN: 0444888233.

[74] M. A. A. Neil, R. Juškaitis, and T. Wilson, "Method of obtaining optical sectioning by using structured light in a conventional microscope", *Optics Letters*, vol. 22, no. 24, p. 1905, 1997, ISSN: 0146-9592. DOI: 10.1364/OL.22.001905.

[75] R. Heintzmann and C. G. Cremer, "Laterally modulated excitation microscopy: improvement of resolution by using a diffraction grating</title>", I. J. Bigio, H. Schneckenburger, J. Slavik, K. Svanberg, and P. M. Viallet, Eds., vol. 3568, International Society for Optics and Photonics, Jan. 1999, pp. 185–196. DOI: 10.1117/12.336833.

[76] L. Schermelleh, P. M. Carlton, S. Haase, L. Shao, L. Winoto, P. Kner, B. Burke, M. C. Cardoso, D. A. Agard, M. G. Gustafsson, H. Leonhardt, and J. W. Sedat, "Subdiffraction multicolor imaging of the nuclear periphery with 3D structured illumination microscopy", *Science*, vol. 320, no. 5881, pp. 1332–1336, Jun. 2008, ISSN: 00368075. DOI: 10.1126/science.1156947.

[77] M. G. Gustafsson, "Extended resolution fluorescence microscopy", *Current Opinion in Structural Biology*, vol. 9, no. 5, pp. 627–628, Oct. 1999, ISSN: 0959440X. DOI: 10.1016/S0959-440X(99)00016-0.

[78] L. Shao, B. Isaac, S. Uzawa, D. A. Agard, J. W. Sedat, and M. G. L. Gustafsson, "I5S: wide-field light microscopy with 100-nm-scale resolution in three dimensions.", *Biophysical journal*, vol. 94, no. 12, pp. 4971–83, Jun. 2008, ISSN: 1542-0086. DOI: 10.1529/biophysj.107.120352.

[79] E. H. Rego, L. Shao, J. J. Macklin, L. Winoto, G. A. Johansson, N. Kamps-Hughes, M. W. Davidson, and M. G. L. Gustafsson, "Nonlinear structured-illumination microscopy with a photoswitchable protein reveals cellular structures at 50-nm resolution", *Proceedings of the National Academy of Sciences*, vol. 109, no. 3, E135–E143, Jan. 2012, ISSN: 0027-8424. DOI: 10.1073/pnas.1107547108.

[80] J. Huisken, J. Swoger, F. Del Bene, J. Wittbrodt, and E. H. Stelzer, "Optical sectioning deep inside live embryos by selective plane illumination microscopy", *Science*, vol. 305, no. 5686, pp. 1007–1009, Aug. 2004, ISSN: 00368075. DOI: 10.1126/science.1100035.

[81] P. J. Keller, A. D. Schmidt, J. Wittbrodt, and E. H. Stelzer, "Reconstruction of zebrafish early embryonic development by scanned light sheet microscopy", *Science*, vol. 322, no. 5904, pp. 1065–1069, Nov. 2008, ISSN: 00368075. DOI: 10.1126/science.1162493.

[82] B. C. Chen, W. R. Legant, K. Wang, L. Shao, D. E. Milkie, M. W. Davidson, C. Janetopoulos, X. S. Wu, J. A. Hammer, Z. Liu, B. P. English, Y. Mimori-Kiyosue, D. P. Romero, A. T. Ritter, J. Lippincott-Schwartz, L. Fritz-Laylin, R. D. Mullins, D. M. Mitchell, J. N. Bembenek, A. C. Reymann, R. Böhme, S. W. Grill, J. T. Wang, G. Seydoux, U. S. Tulu, D. P. Kiehart, and E. Betzig, "Lattice light-sheet microscopy: Imaging molecules to embryos at high spatiotemporal resolution", *Science*, vol. 346, no. 6208, pp. 1 257 998–1 257 998, 2014, ISSN: 10959203. DOI: 10.1126/science.1257998.

[83] D. Li, L. Shao, B.-C. Chen, X. Zhang, M. Zhang, B. Moses, D. E. Milkie, J. R. Beach, J. A. Hammer, M. Pasham, T. Kirchhausen, M. A. Baird, M. W. Davidson, P. Xu, and E. Betzig, "Extended-resolution structured illumination imaging of endocytic and cytoskeletal dynamics", *Science*, vol. 349, no. 6251, aab3500–aab3500, Aug. 2015, ISSN: 0036-8075. DOI: 10.1126/science.aab3500.

[84] L. Gao, L. Shao, C. D. Higgins, J. S. Poulton, M. Peifer, M. W. Davidson, X. Wu, B. Goldstein, and E. Betzig, "Noninvasive imaging beyond the diffraction limit of 3D dynamics in thickly fluorescent specimens.", *Cell*, vol. 151, no. 6, pp. 1370–85, Dec. 2012, ISSN: 1097-4172. DOI: 10.1016/j.cell.2012.10.008.

[85] T.-l. Liu, S. Upadhyayula, D. E. Milkie, V. Singh, K. Wang, I. A. Swinburne, K. R. Mosaliganti, Z. M. Collins, T. W. Hiscock, J. Shea, A. Q. Kohrman, T. N. Medwig, D. Dambournet, R. Forster, B. Cunniff, Y. Ruan, H. Yashiro, S. Scholpp, E. M. Meyerowitz, D. Hockemeyer, D. G. Drubin, B. L. Martin, D. Q. Matus, M. Koyama, S. G. Megason, T. Kirchhausen, and E. Betzig, "Observing the cell in its native state: Imaging subcellular dynamics in multicellular organisms", *Science*, vol. 360, no. 6386, eaaq1392, Apr. 2018, ISSN: 0036-8075. DOI: 10.1126/science.aaq1392.

[86] T. a. Klar and S. W. Hell, "Subdiffraction resolution in far-field fluorescence microscopy.", *Optics letters*, vol. 24, no. 14, pp. 954–6, Jul. 1999, ISSN: 0146-9592. DOI: 10.1364/OL.24.000954.

[87] T. a. Klar, S Jakobs, M Dyba, A Egner, and S. W. Hell, "Fluorescence microscopy with diffraction resolution barrier broken by stimulated emission.", *Proceedings of the National Academy of Sciences of the United States of America*, vol. 97, no. 15, pp. 8206–8210, 2000, ISSN: 0027-8424. DOI: 10.1073/pnas.97.15.8206.

[88] P. Török and P. Munro, "The use of Gauss-Laguerre vector beams in STED microscopy", *Optics Express*, vol. 12, no. 15, p. 3605, 2004, ISSN: 1094-4087. DOI: 10.1364/OPEX.12.003605.

[89] S. A. Kennedy, M. J. Szabo, H. Teslow, J. Z. Porterfield, and E. R. Abraham, "Creation of Laguerre-Gaussian laser modes using diffractive optics", *Physical Review A - Atomic, Molecular, and Optical Physics*, vol. 66, no. 4, pp. 438 011–438 015, 2002, ISSN: 10502947. DOI: 10.1103/PhysRevA.66.043801.

[90] V. Westphal and S. W. Hell, "Nanoscale resolution in the focal plane of an optical microscope", *Physical Review Letters*, vol. 94, no. 14, pp. 1–4, 2005, ISSN: 00319007. DOI: 10.1103/PhysRevLett.94.143903.

[91] F. Göttfert, C. A. Wurm, V. Mueller, S. Berning, V. C. Cordes, A. Honigmann, and S. W. Hell, "Coaligned dual-channel STED nanoscopy and molecular diffusion analysis at 20 nm resolution", *Biophysical Journal*, vol. 105, no. 1, 2013, ISSN: 00063495. DOI: 10.1016/j.bpj.2013.05.029.

[92] E. Rittweger, K. Y. Han, S. E. Irvine, C. Eggeling, and S. W. Hell, "STED microscopy reveals crystal colour centres with nanometric resolution", *Nature Photonics*, vol. 3, no. 3, pp. 144–147, 2009, ISSN: 17494885. DOI: 10.1038/nphoton.2009.2.

[93] T. J. Gould, E. B. Kromann, D. Burke, M. J. Booth, and J. Bewersdorf, "Auto-aligning stimulated emission depletion microscope using adaptive optics", *Optics Letters*, vol. 38, no. 11, p. 1860, Jun. 2013, ISSN: 0146-9592. DOI: 10.1364/OL.38.001860.

[94] T. J. Gould, D. Burke, J. Bewersdorf, and M. J. Booth, "Adaptive optics enables 3D STED microscopy in aberrating specimens", *Optics express*, vol. 20, no. 19, p. 20 998, Sep. 2012, ISSN: 1094-4087. DOI: 10.1364/OE.20.020998.

[95] D. Wildanger, R. Medda, L. Kastrup, and S. W. Hell, "A compact STED microscope providing 3D nanoscale resolution.", *Journal of microscopy*, vol. 236, no. 1, pp. 35–43, Oct. 2009, ISSN: 1365-2818. DOI: 10.1111/j.1365-2818.2009.03188.x.

[96] M. Dyba and S. W. Hell, "Photostability of a fluorescent marker under pulsed excited-state depletion through stimulated emission.", *Applied optics*, vol. 42, no. 25, pp. 5123–5129, 2003, ISSN: 0003-6935. DOI: 10.1364/AO.42.005123.

[97] P. C. Goodwin, "Evaluating Optical Aberration Using Fluorescent Microspheres: Methods, Analysis, and Corrective Actions", *Methods in Cell Biology*, vol. 81, pp. 397–413, Jan. 2007, ISSN: 0091-679X. DOI: 10.1016/S0091-679X(06)81018-6.

[98] J. R. Fienup and J. J. Miller, "Aberration correction by maximizing generalized sharpness metrics", *Journal of the Optical Society of America A*, vol. 20, no. 4, p. 609, 2003, ISSN: 1084-7529. DOI: 10.1364/JOSAA.20.000609.

[99] M. J. Booth, M. A. A. Neil, and T Wilson, "Aberration correction for confocal imaging in refractive-index-mismatched media", *Journal of Microscopy-Oxford*, vol. 192, no. May, pp. 90–98, 1998, ISSN: 0022-2720. DOI: 10.1111/j.1365-2818.1998.99999.x.

[100] M. J. Booth, M. A. A. Neil, R. Juskaitis, and T. Wilson, "Adaptive aberration correction in a confocal microscope", *Proceedings of the National Academy of Sciences*, vol. 99, no. 9, pp. 5788–5792, 2002, ISSN: 0027-8424. DOI: 10.1073/pnas.082544799.

[101] M. J. Booth, D. Andrade, D. Burke, B. R. Patton, and M. Zurauskas, "Aberrations and adaptive optics in super-resolution microscopy", *Microscopy*, vol. 64, no. 4, pp. 251–261, 2015, ISSN: 20505701. DOI: 10.1093/jmicro/dfv033.

[102] A. Cornea and P. M. Conn, *Fluorescence Microscopy: Super-resolution and Other Novel Techniques*, 10. Elsevier, 2014, vol. 2014, pp. 15–33, ISBN: 9780124095137. DOI: 10.1016/B978-0-12-409513-7.00002-6.

[103] M. J. Booth, "Adaptive optical microscopy: The ongoing quest for a perfect image", *Light: Science and Applications*, vol. 3, no. 4, e165, Apr. 2014, ISSN: 20477538. DOI: 10.1038/lsa.2014.46.

[104] D. Débarre, M. J. Booth, and T. Wilson, "Image based adaptive optics through optimisation of low spatial frequencies", *J. W. Hardy OPTICS EXPRESS*, vol. 15, no. 18, pp. 5131–5139, 1991, ISSN: 1094-4087. DOI: 10.1364/OE.15.008176.

[105] N. Ji, "Adaptive optical fluorescence microscopy", *Nature Methods*, vol. 14, no. 4, pp. 374–380, 2017, ISSN: 15487105. DOI: 10.1038/nmeth.4218.

[106] G. Ball, J. Demmerle, R. Kaufmann, I. Davis, I. M. Dobbie, and L. Schermelleh, "SIMcheck: a Toolbox for Successful Super-resolution Structured Illumination Microscopy", *Scientific Reports*, vol. 5, no. 1, p. 15 915, Dec. 2015, ISSN: 2045-2322. DOI: 10.1038/srep15915.

[107] S. Deng, L. Liu, Y. Cheng, R. Li, and Z. Xu, "Effects of primary aberrations on the fluorescence depletion patterns of STED microscopy.", *Optics express*, vol. 18, no. 2, pp. 1657–1666, 2010, ISSN: 1094-4087. DOI: 10.1364/OE.18.001657.

[108] X. Chen, J. Chen, S. Dong, H. Yang, and S. Xie, "Effects of Seidel aberration and light polarization on the resolution of STED imaging", *Optik*, vol. 130, pp. 76–81, 2017, ISSN: 00304026. DOI: 10.1016/j.ijleo.2016.11.026.

[109] J. Antonello, E. B. Kromann, D. Burke, J. Bewersdorf, and M. J. Booth, "Coma aberrations in combined two- and three-dimensional STED nanoscopy", *Optics Letters*, vol. 41, no. 15, p. 3631, 2016, ISSN: 0146-9592. DOI: 10.1364/OL.41.003631.

[110] N. T. Urban, K. I. Willig, S. W. Hell, and U. V. Nägerl, "STED nanoscopy of actin dynamics in synapses deep inside living brain slices", *Biophysical Journal*, vol. 101, no. 5, pp. 1277–1284, Sep. 2011, ISSN: 00063495. DOI: 10.1016/j.bpj.2011.07.027.

[111] S. W. Hell, "Toward fluorescence nanoscopy", *Nature Biotechnology*, vol. 21, no. 11, pp. 1347–1355, 2003, ISSN: 10870156. DOI: 10.1038/nbt895.

[112] S. W. Hell, "Microscopy and its focal switch", *Nature Methods*, vol. 6, no. 1, pp. 24–32, Jan. 2009, ISSN: 15487091. DOI: 10.1038/nmeth.1291.

[113] S. W. Hell and M. Kroug, "Ground-state-depletion fluorscence microscopy: A concept for breaking the diffraction resolution limit", *Applied Physics B Lasers and Optics*, vol. 60, no. 5, pp. 495–497, May 1995, ISSN: 0946-2171. DOI: 10.1007/BF01081333.

[114] P. F. G. Rodriguez, Y Wu, H Singh, and H Zhao, "Building a fast scanning stimulated emission depletion microscope: a step by step guide", *Current Microscopy Contributions to Advances in Science and Technology*, pp. 791–800, 2012.

[115] T. Klar, E. Engel, and S. W. Hell, "Breaking Abbe's diffraction resolution limit in fluorescence microscopy with stimulated emission depletion beams of various shapes", *Physical Review E*, vol. 64, no. 6, p. 066 613, Nov. 2001, ISSN: 1063-651X. DOI: 10.1103/PhysRevE.64.066613.

[116] G. Donnert, J. Keller, R. Medda, M. A. Andrei, S. O. Rizzoli, R. Luhrmann, R. Jahn, C. Eggeling, and S. W. Hell, "Macromolecular-scale resolution in biological fluorescence microscopy", *Proceedings of the National Academy of Sciences*, vol. 103, no. 31, pp. 11 440–11 445, 2006, ISSN: 0027-8424. DOI: 10.1073/pnas.0604965103.

[117] M. P. Clausen, S. Galiani, J. B.d. l. Serna, M. Fritzsche, J. Chojnacki, K. Gehmlich, B. C. Lagerholm, and C. Eggeling, "Pathways to optical STED microscopy", *NanoBioImaging*, vol. 1, no. 1, Jan. 2014, ISSN: 2299-3150. DOI: 10.2478/nbi-2013-0001.

[118] P. Tinnefeld, C. Eggeling, and S. W. Hel, *Far-Field Optical Nanoscopy*, P. Tinnefeld, C. Eggeling, and S. W. Hel, Eds. Berlin: Springer-Verlag Berlin Heidelberg, 2015, vol. 14, p. 335, ISBN: 978-3-662-45546-3. DOI: 10.1007/978-3-662-45547-0.

[119] M. Leutenegger, C. Eggeling, and S. W. Hell, "Analytical description of STED microscopy performance", *Optics Express*, vol. 18, no. 25, p. 26 417, Dec. 2010, ISSN: 1094-4087. DOI: 10.1364/OE.18.026417.

[120] G. Vicidomini, G. Moneron, C. Eggeling, E. Rittweger, and S. W. Hell, "STED with wavelengths closer to the emission maximum", *Optics Express*, vol. 20, no. 5, p. 5225, 2012, ISSN: 1094-4087. DOI: 10.1364/OE.20.005225.

[121] V. Westphal, C. M. Blanca, M. Dyba, L. Kastrup, and S. W. Hell, "Laser-diode-stimulated emission depletion microscopy", *Applied Physics Letters*, vol. 82, no. 18, pp. 3125–3127, 2003, ISSN: 00036951. DOI: 10.1063/1.1571656.

[122] S. Schrof, T. Staudt, E. Rittweger, N. Wittenmayer, T. Dresbach, J. Engelhardt, and S. W. Hell, "STED nanoscopy with mass-produced laser diodes.", *Optics express*, vol. 19, no. 9, pp. 8066–8072, 2011, ISSN: 1094-4087. DOI: 10.1364/OE.19.008066.

[123] B. Harke, "3D STED microscopy with pulsed and continuous wave lasers", PhD thesis, 2008.

[124] G. Moneron, R. Medda, B. Hein, A. Giske, V. Westphal, and S. W. Hell, "Fast STED microscopy with continuous wave fiber lasers.", *Optics express*, vol. 18, no. 2, pp. 1302–9, Jan. 2010, ISSN: 1094-4087.

[125] K. I. Willig, B. Harke, R. Medda, and S. W. Hell, "STED microscopy with continuous wave beams", *Nature Methods*, vol. 4, no. 11, pp. 915–918, 2007, ISSN: 15487091. DOI: 10.1038/nmeth1108.

[126] P. Bianchini and A. Diaspro, "Fast scanning STED and two-photon fluorescence excitation microscopy with continuous wave beam", *Journal of Microscopy*, vol. 245, no. 3, pp. 225–228, 2012, ISSN: 00222720. DOI: 10.1111/j.1365-2818.2011.03577.x.

[127] J. R. Moffitt, C. Osseforth, and J. Michaelis, "Time-gating improves the spatial resolution of STED microscopy", *Optics Express*, vol. 19, no. 5, p. 4242, 2011, ISSN: 1094-4087. DOI: 10.1364/OE.19.004242.

[128] G. Vicidomini, G. Moneron, K. Y. Han, V. Westphal, H. Ta, M. Reuss, J. Engelhardt, C. Eggeling, and S. W. Hell, "Sharper low-power STED nanoscopy by time gating", *Nature Methods*, vol. 8, no. 7, pp. 571–575, 2011, ISSN: 15487091. DOI: 10.1038/nmeth.1624.

[129] G. Vicidomini, A. Schönle, H. Ta, K. Y. Han, G. Moneron, C. Eggeling, and S. W. Hell, "STED Nanoscopy with Time-Gated Detection: Theoretical and Experimental Aspects", *PLoS ONE*, vol. 8, no. 1, 2013, ISSN: 19326203. DOI: 10.1371/journal.pone.0054421.

[130] L Eggeling, S Oberle, and H Sahm, "Improved L-lysine yield with Corynebacterium glutamicum: Use of dapA resulting in increased flux combined with growth limitation", *Applied Microbiology and Biotechnology*, vol. 49, no. 1, pp. 24–30, Jan. 1998, ISSN: 01757598. DOI: 10.1007/s002530051132.

[131] B. R. Rankin, G. Moneron, C. a. Wurm, J. C. Nelson, A. Walter, D. Schwarzer, J. Schroeder, D. a. Colón-Ramos, and S. W. Hell, "Nanoscopy in a living multicellular organism expressing GFP", *Biophysical Journal*, vol. 100, no. 12, pp. 63–65, 2011, ISSN: 00063495. DOI: 10.1016/j.bpj.2011.05.020.

[132] Y. Wu, X. Wu, R. Lu, J. Zhang, L. Toro, and E. Stefani, "Resonant Scanning with Large Field of View Reduces Photobleaching and Enhances Fluorescence Yield in STED Microscopy.", *Scientific reports*, vol. 5, no. November 2014, p. 14 766, 2015, ISSN: 2045-2322. DOI: 10.1038/srep14766.

[133] R. T. Borlinghaus, "MRT letter: High speed scanning has the potential to increase fluorescence yield and to reduce photobleaching", *Microscopy Research and Technique*, vol. 69, no. 9, pp. 689–692, Sep. 2006, ISSN: 1059910X. DOI: 10.1002/jemt.20363.

[134] L. Song, C. A. Varma, J. W. Verhoeven, and H. J. Tanke, "Influence of the triplet excited state on the photobleaching kinetics of fluorescein in microscopy.", *Biophysical journal*, vol. 70, no. 6, pp. 2959–68, Jun. 1996, ISSN: 0006-3495. DOI: 10.1016/S0006-3495(96)79866-1.

[135] L. Song, E. J. Hennink, I. T. Young, and H. J. Tanke, "Photobleaching kinetics of fluorescein in quantitative fluorescence microscopy.", *Biophysical journal*, vol. 68, no. 6, pp. 2588–600, Jun. 1995, ISSN: 0006-3495. DOI: 10.1016/S0006-3495(95)80442-X.

[136] G. Donnert, C. Eggeling, and S. W. Hell, "Major signal increase in fluorescence microscopy through dark-state relaxation", *Nature Methods*, vol. 4, no. 1, pp. 81–86, 2007, ISSN: 15487091. DOI: 10.1038/nmeth986.

[137] J.-i. Hotta, E. Fron, P. Dedecker, K. P. F. Janssen, C. Li, K. Müllen, B. Harke, J. Bückers, S. W. Hell, and J. Hofkens, "Spectroscopic rationale for efficient stimulated-emission depletion microscopy fluorophores", *Journal of the American Chemical Society*, vol. 132, no. 14, pp. 5021–5023, 2010, ISSN: 00027863. DOI: 10.1021/ja100079w.

[138] C. Osseforth, J. R. Moffitt, L. Schermelleh, and J. Michaelis, "Simultaneous dual-color 3D STED microscopy.", *Optics express*, vol. 22, no. 6, p. 7028, Mar. 2014, ISSN: 1094-4087. DOI: 10.1364/OE.22.007028.

[139] B. Harke, C. K. Ullal, J. Keller, and S. W. Hell, "Three-dimensional nanoscopy of colloidal crystals", *Nano Letters*, vol. 8, pp. 1309–1313, 2008, ISSN: 15306984. DOI: 10.1021/nl073164n.

[140] M. Reuss, J. Engelhardt, and S. W. Hell, "Birefringent device converts a standard scanning microscope into a STED microscope that also maps molecular orientation.", *Optics express*, vol. 18, no. 2, pp. 1049–58, Jan. 2010, ISSN: 1094-4087.

[141] A. Klauss, M. König, and C. Hille, "Upgrade of a Scanning Confocal Microscope to a Single-Beam Path STED Microscope", *PLOS ONE*, vol. 10, no. 6, T. Abraham, Ed., e0130717, Jun. 2015, ISSN: 1932-6203. DOI: 10.1371/journal.pone.0130717.

[142] E. Auksorius, B. R. Boruah, C. Dunsby, P. M. P. Lanigan, G. Kennedy, M. A. A. Neil, and P. M. W. French, "Stimulated emission depletion microscopy with a supercontinuum source and fluorescence lifetime imaging.", *Optics letters*, vol. 33, no. 2, pp. 113–5, Jan. 2008, ISSN: 0146-9592.

[143] G. P. J. Laporte, D. B. Conkey, A. Vasdekis, R. Piestun, and D. Psaltis, "Double-helix enhanced axial localization in STED nanoscopy", *Optics Express*, vol. 21, no. 25, p. 30 984, 2013, ISSN: 1094-4087. DOI: 10.1364/OE.21.030984.

[144] S. Li, C. Kuang, X. Hao, Z. Gu, and X. Liu, "Generation of a 3D isotropic hollow focal spot for single-objective stimulated emission depletion microscopy", *Journal of Optics*, vol. 14, no. 8, p. 085 704, 2012, ISSN: 2040-8978. DOI: 10.1088/2040-8978/14/8/085704.

[145] T. Čižmár, M. Mazilu, and K. Dholakia, "In situ wavefront correction and its application to micromanipulation", *Nature Photonics*, vol. 4, no. 6, pp. 388–394, 2010, ISSN: 17494885. DOI: 10.1038/nphoton.2010.85.

[146] B. R. Patton, D. Burke, R. Vrees, and M. J. Booth, "Is phase-mask alignment aberrating your STED microscope?", *Methods and Applications in Fluorescence*, vol. 3, no. 2, p. 024 002, 2015, ISSN: 2050-6120. DOI: 10.1088/2050-6120/3/2/024002.

[147] Z. Deng, T. Zink, H.-y. Chen, D. Walters, F.-t. Liu, and G.-y. Liu, "Impact of Actin Rearrangement and Degranulation on the Membrane Structure of Primary Mast Cells: A Combined Atomic Force and Laser Scanning Confocal Microscopy Investigation", *Biophysical Journal*, vol. 96, no. 4, pp. 1629–1639, Feb. 2009, ISSN: 00063495. DOI: 10.1016/j.bpj.2008.11.015.

[148] J. Antonello, D. Burke, and M. J. Booth, "Aberrations in stimulated emission depletion (STED) microscopy", *Optics Communications*, vol. 404, no. March, pp. 203–209, 2017, ISSN: 00304018. DOI: 10.1016/j.optcom.2017.06.037.

[149] S. Galiani, B. Harke, G. Vicidomini, G. Lignani, F. Benfenati, A. Diaspro, and P. Bianchini, "Strategies to maximize the performance of a STED microscope.", *Optics express*, vol. 20, no. 7, pp. 7362–74, Mar. 2012, ISSN: 1094-4087.

[150] J. Keller, A. Schönle, and S. W. Hell, "Efficient fluorescence inhibition patterns for RESOLFT microscopy", *Optics Express*, vol. 15, no. 6, p. 3361, Mar. 2007, ISSN: 1094-4087. DOI: 10.1364/OE.15.003361.

[151] X. Hao, C. Kuang, T. Wang, and X. Liu, "Effects of polarization on the de-excitation dark focal spot in STED microscopy", *Journal of Optics*, vol. 12, no. 11, 2010, ISSN: 20408978. DOI: 10.1088/2040-8978/12/11/115707.

[152] G. Moneron and S. W. Hell, "Two-photon excitation STED microscopy.", *Optics express*, vol. 17, no. 17, pp. 14 567–73, Aug. 2009, ISSN: 1094-4087.

[153] K. T. Takasaki, J. B. Ding, and B. L. Sabatini, "Live-cell superresolution imaging by pulsed STED two-photon excitation microscopy.", *Biophysical journal*, vol. 104, no. 4, pp. 770–7, Feb. 2013, ISSN: 1542-0086. DOI: 10.1016/j.bpj.2012.12.053.

[154] W. Yan, Y. Yang, Y. Li, X. Peng, D. Lin, J. Qu, and T. Ye, "Aberration correction for stimulated emission depletion microscopy with coherent optical adaptive technique", *Adaptive Optics and Wavefront Control for Biological Systems II*, vol. 9717, 97170K, 2016, ISSN: 16057422. DOI: 10.1117/12.2211907.

[155] W. Yan, Y. Yang, Y. Tan, X. Chen, Y. Li, J. Qu, and T. Ye, "Coherent optical adaptive technique improves the spatial resolution of STED microscopy in thick samples", *Photonics Research*, vol. 5, no. 3, p. 176, 2017, ISSN: 2327-9125. DOI: 10.1364/PRJ.5.000176.

[156] W. Yu, Z. Ji, D. Dong, X. Yang, Y. Xiao, Q. Gong, P. Xi, and K. Shi, "Super-resolution deep imaging with hollow Bessel beam STED microscopy", *Laser and Photonics Reviews*, vol. 10, no. 1, pp. 147–152, 2016, ISSN: 18638899. DOI: 10.1002/lpor.201500151.

[157] M. O. Lenz, H. G. Sinclair, A. Savell, J. H. Clegg, A. C. N. Brown, D. M. Davis, C. Dunsby, M. A. A. Neil, and P. M. W. French, "3-D stimulated emission depletion microscopy with programmable aberration correction", *Journal of Biophotonics*, vol. 7, no. 1-2, pp. 29–36, Jan. 2014, ISSN: 1864063X. DOI: 10.1002/jbio.201300041.

[158] B. R. Patton, D. Burke, D. Owald, T. J. Gould, J. Bewersdorf, and M. J. Booth, "Three-dimensional STED microscopy of aberrating tissue using dual adaptive optics", *Optics Express*, vol. 24, no. 8, p. 8862, 2016, ISSN: 1094-4087. DOI: 10.1364/OE.24.008862.

[159] Z. Zhang, Z. You, and D. Chu, "Fundamentals of phase-only liquid crystal on silicon (LCOS) devices", *Light: Science and Applications*, vol. 3, no. 10, e213, 2014, ISSN: 20477538. DOI: 10.1038/lsa.2014.94.

[160] C. Sheppard and A. Choudhury, "Image Formation in the Scanning Microscope", *Optica Acta: International Journal of Optics*, vol. 24, no. 10, pp. 1051–1073, Oct. 1977, ISSN: 0030-3909. DOI: 10.1080/713819421.

[161] C. A. Wurm, K. Kolmakov, F. Göttfert, H. Ta, M. Bossi, H. Schill, S. Berning, S. Jakobs, G. Donnert, V. N. Belov, and S. W. Hell, "Novel red fluorophores with superior performance in STED microscopy", *Optical Nanoscopy*, vol. 1, no. 1, p. 7, 2012, ISSN: 2192-2853. DOI: 10.1186/2192-2853-1-7.

[162] K. Kolmakov, C. a. Wurm, D. N. H. Meineke, F. Göttfert, V. P. Boyarskiy, V. N. Belov, and S. W. Hell, "Polar red-emitting rhodamine dyes with reactive groups: synthesis, photophysical properties, and two-color STED nanoscopy applications.", *Chemistry (Weinheim an der Bergstrasse, Germany)*, vol. 20, no. 1, pp. 146–57, Jan. 2014, ISSN: 1521-3765. DOI: 10.1002/chem.201303433.

[163] K. Kolmakov, C. A. Wurm, R. Hennig, E. Rapp, S. Jakobs, V. N. Belov, and S. W. Hell, "Red-Emitting Rhodamines with Hydroxylated, Sulfonated, and Phosphorylated Dye Residues and Their Use in Fluorescence Nanoscopy", *Chemistry - A European Journal*, vol. 18, no. 41, pp. 12 986–12 998, Oct. 2012, ISSN: 09476539. DOI: 10.1002/chem.201201168.

[164] H. Schill, S. Nizamov, F. Bottanelli, J. Bierwagen, V. N. Belov, and S. W. Hell, "4-Trifluoromethyl-Substituted Coumarins with Large Stokes Shifts: Synthesis, Bioconjugates, and Their Use in Super-Resolution Fluorescence Microscopy", *Chemistry - A European Journal*, vol. 19, no. 49, pp. 16 556–16 565, Dec. 2013, ISSN: 09476539. DOI: 10.1002/chem.201302037.

[165] M. W. D. Jeffrey M. Larson Stanley A. Schwartz, *Resonant Scanning in Laser Confocal Microscopy*.

[166] N Callamaras and I Parker, "Construction of a confocal microscope for real-time x-y and x-z imaging.", *Cell calcium*, vol. 26, no. 6, pp. 271–279, 1999, ISSN: 01434160. DOI: 10.1054/ceca.1999.0085.

[167] L. Leybaert, a. De Meyer, C. Mabilde, and M. J. Sanderson, "A simple and practical method to acquire geometrically correct images with resonant scanning-based line scanning in a custom-built video-rate laser scanning microscope", *Journal of Microscopy*, vol. 219, no. 3, pp. 133–140, 2005, ISSN: 00222720. DOI: 10.1111/j.1365-2818.2005.01502.x.

[168] Rolf T. Borlinghaus, *Smart Control for Resonant Galvo Scanners*.

[169] M. Guizar-Sicairos, S. T. Thurman, and J. R. Fienup, "Efficient subpixel image registration algorithms.", *Optics letters*, vol. 33, no. 2, pp. 156–8, Jan. 2008, ISSN: 0146-9592.

[170] M. Guizar-Sicairos, *http://www.mathworks.com/matlabcentral/fileexchange/18401-efficient-subpixel-image-registration-by-cross-correlation*.

[171] M. A. A. Neil, M. J. Booth, and T. Wilson, "Closed-loop aberration correction by use of a modal Zernike wave-front sensor.", *Optics letters*, vol. 25, no. 15, pp. 1083–1085, 2000, ISSN: 0146-9592. DOI: 10.1364/OL.25.001083.

[172] H. Gross, H. Zügge, M. Peschka, and F. Blechinger, *Handbook of Optical Systems Volume 3: Aberration Theory and Correction of Optical Systems*, H. Gross, H. Zügge, M. Peschka, and F. Blechinger, Eds. Weinheim, Germany: Wiley-VCH Verlag GmbH & Co. KGaA, Dec. 2006, vol. 2, ISBN: 9783527699254. DOI: 10.1002/9783527699254.

[173] M. J. Booth and B. R. Patton, *Adaptive Optics for Fluorescence Microscopy*. Elsevier, 2014, pp. 15–33, ISBN: 9780124167131. DOI: 10.1016/B978-0-12-409513-7.00002-6.

[174] C. A. Wurm, D. Neumann, R. Schmidt, A. Egner, and S. Jakobs, "Sample Preparation for STED Microscopy", in, Humana Press, 2010, pp. 185–199. DOI: 10.1007/978-1-60761-404-3{_}11.

[175] S. M. Chambers, C. A. Fasano, E. P. Papapetrou, M. Tomishima, M. Sadelain, and L. Studer, "Highly efficient neural conversion of human ES and iPS cells by dual inhibition of SMAD signaling", *Nature Biotechnology*, vol. 27, no. 3, pp. 275–280, 2009, ISSN: 10870156. DOI: 10.1038/nbt.1529.

[176] H. Kirshner, D. Sage, and M. Unser, "3D PSF models for fluorescence microscopy in ImageJ", vol. 1, p. 2010, 2011.

[177] H. KIRSHNER, F. AGUET, D. SAGE, and M. UNSER, "3-D PSF fitting for fluorescence microscopy: implementation and localization application", *Journal of Microscopy*, vol. 249, no. 1, pp. 13–25, Jan. 2013, ISSN: 00222720. DOI: 10.1111/j.1365-2818.2012.03675.x.

[178] B Richards and E Wolf, "Electromagnetic Diffraction in Optical Systems. II. Structure of the Image Field in an Aplanatic System", *Proceedings of the Royal Society of London Series a-Mathematical and Physical Sciences*, vol. 253, no. 1274, p. 3 580 379, Dec. 1959, ISSN: 1364-5021. DOI: 10.1098/rspa.1959.0200.

[179] D. Merino, A. Mallabiabarrena, J. Andilla, D. Artigas, T. Zimmermann, and P. Loza-Alvarez, "STED imaging performance estimation by means of Fourier transform analysis", *Biomedical Optics Express*, vol. 8, no. 5, pp. 2472–2482, 2017, ISSN: 2156-7085. DOI: 10.1364/BOE.8.002472.

[180] K. Beeson, M. J. Potasek, and E. Parilov, "Optimizing experimental conditions for stimulated emission depletion microscopy in biophotonics", vol. 9369, no. March, p. 93690V, 2015, ISSN: 1996756X. DOI: 10.1117/12.2079479.

[181] S. W. Hell, S. J. Sahl, M. Bates, X. Zhuang, R. Heintzmann, M. J. Booth, J. Bewersdorf, G. Shtengel, H. Hess, P. Tinnefeld, A. Honigmann, S. Jakobs, I. Testa, L. Cognet, B. Lounis, H. Ewers, S. J. Davis, C. Eggeling, D. Klenerman, K. I. Willig, G. Vicidomini, M. Castello, A. Diaspro, and T. Cordes, "The 2015 super-resolution microscopy roadmap", *Journal of Physics D: Applied Physics*, vol. 48, no. 44, 2015, ISSN: 13616463. DOI: 10.1088/0022-3727/48/44/443001.

[182] G. Vicidomini, P. Bianchini, and A. Diaspro, "STED super-resolved microscopy", *Nature Methods*, no. i, 2018, ISSN: 1548-7091. DOI: 10.1038/nmeth.4593.

[183] R. Zanella, G. Zanghirati, R. Cavicchioli, L. Zanni, P. Boccacci, M. Bertero, and G. Vicidomini, "Towards real-time image deconvolution: application to confocal and STED microscopy", *Scientific Reports*, vol. 3, pp. 1593–1601, Aug. 2013, ISSN: 2045-2322. DOI: 10.1038/srep02523.

[184] M. Castello, A. Diaspro, and G. Vicidomini, "Multi-images deconvolution improves signal-to-noise ratio on gated stimulated emission depletion microscopy", *Applied Physics Letters*, vol. 105, no. 23, 2014, ISSN: 00036951. DOI: 10.1063/1.4904092.

[185] P. Campisi and K Egiazarian, *Blind image deconvolution: theory and applications*. 2007, p. 472, ISBN: 0849300525.

[186] B. Kim and T. Naemura, "Blind deconvolution of 3D fluorescence microscopy using depth-variant asymmetric PSF", *Microscopy Research and Technique*, vol. 79, no. 6, pp. 480–494, 2016, ISSN: 10970029. DOI: 10.1002/jemt.22650.

[187] B. Kim and T. Naemura, "Blind Depth-variant Deconvolution of 3D Data in Wide-field Fluorescence Microscopy", *Scientific Reports*, vol. 5, no. 1, p. 9894, Sep. 2015, ISSN: 2045-2322. DOI: 10.1038/srep09894.

[188] Y. Wu, X. Wu, L. Toro, and E. Stefani, "Resonant-scanning dual-color STED microscopy with ultrafast photon counting: A concise guide", *Methods*, vol. 88, pp. 48–56, 2015, ISSN: 10959130. DOI: 10.1016/j.ymeth.2015.06.019.

[189] J. Schneider, J. Zahn, M. Maglione, S. J. Sigrist, J. Marquard, J. Chojnacki, H. G. Kräusslich, S. J. Sahl, J. Engelhardt, and S. W. Hell, "Ultrafast, temporally stochastic STED nanoscopy of millisecond dynamics", *Nature Methods*, vol. 12, no. 9, pp. 827–830, 2015, ISSN: 15487105. DOI: 10.1038/nmeth.3481.

[190] T. Staudt, A. Engler, E. Rittweger, B. Harke, J. Engelhardt, and S. W. Hell, "Far-field optical nanoscopy with reduced number of state transition cycles", *Optics Express*, vol. 19, no. 6, p. 5644, 2011, ISSN: 1094-4087. DOI: 10.1364/OE.19.005644.

[191] F. Göttfert, T. Pleiner, J. Heine, V. Westphal, D. Görlich, S. J. Sahl, and S. W. Hell, "Strong signal increase in STED fluorescence microscopy by imaging regions of subdiffraction extent", *Proceedings of the National Academy of Sciences*, vol. 114, no. 9, pp. 2125–2130, 2017, ISSN: 0027-8424. DOI: 10.1073/pnas.1621495114.

[192] J. Heine, M. Reuss, B. Harke, E. D'Este, S. J. Sahl, and S. W. Hell, "Adaptive-illumination STED nanoscopy", *Proceedings of the National Academy of Sciences*, vol. 114, no. 37, pp. 9797–9802, Sep. 2017, ISSN: 0027-8424. DOI: 10.1073/pnas.1708304114.

[193] P. Bianchini, C. Peres, M. Oneto, S. Galiani, G. Vicidomini, and A. Diaspro, "STED nanoscopy: a glimpse into the future", *Cell and Tissue Research*, 2015, ISSN: 0302-766X. DOI: 10.1007/s00441-015-2146-3.

[194] F. Bottanelli, E. B. Kromann, E. S. Allgeyer, R. S. Erdmann, S. W. Baguley, G. Sirinakis, A. Schepartz, D. Baddeley, D. K. Toomre, J. E. Rothman, and J. Bewersdorf, "Two-colour live-cell nanoscale imaging of intracellular targets", *Nature Communications*, vol. 7, no. May 2015, p. 10 778, 2016, ISSN: 20411723. DOI: 10.1038/ncomms10778.

[195] M. Castello, G. Tortarolo, I. C. Hernández, P. Bianchini, M. Buttafava, G. Boso, A. Tosi, A. Diaspro, and G. Vicidomini, "Gated-sted microscopy with subnanosecond pulsed fiber laser for reducing photobleaching", *Microscopy Research and Technique*, vol. 79, no. 9, pp. 785–791, 2016, ISSN: 10970029. DOI: 10.1002/jemt.22716.

[196] G. Boso, A. Tosi, A. D. Mora, and F. Zappa, "High-throughput gated photon counter with two detection windows programmable down to 70 ps width", *Review of Scientific Instruments*, vol. 85, no. 1, 2014, ISSN: 00346748. DOI: 10.1063/1.4862060.

[197] P. A. Pellett, X. Sun, T. J. Gould, J. E. Rothman, M.-q. Xu, I. R. Corrêa, and J. Bewersdorf, "Two-color STED microscopy in living cells.", *Biomedical optics express*, vol. 2, no. 8, pp. 2364–2371, 2011, ISSN: 2156-7085. DOI: 10.1364/BOE.2.002364.

[198] S. Galiani, D. Waithe, K. Reglinski, L. D. Cruz-Zaragoza, E. Garcia, M. P. Clausen, W. Schliebs, R. Erdmann, and C. Eggeling, "Super-resolution microscopy reveals compartmentalization of peroxisomal membrane proteins", *Journal of Biological Chemistry*, vol. 291, no. 33, pp. 16 948–16 962, 2016, ISSN: 1083351X. DOI: 10.1074/jbc.M116.734038.

[199] K. Y. Han and T. Ha, "Dual-color three-dimensional STED microscopy with a single high-repetition-rate laser.", *Optics letters*, vol. 40, no. 11, pp. 2653–6, 2015, ISSN: 1539-4794. DOI: 10.1364/OL.40.002653.

[200] B. Hein, K. I. Willig, and S. W. Hell, "Stimulated emission depletion (STED) nanoscopy of a fluorescent protein-labeled organelle inside a living cell.", *Proceedings of the National Academy of Sciences of the United States of America*, vol. 105, no. 38, pp. 14 271–6, Sep. 2008, ISSN: 1091-6490. DOI: 10.1073/pnas.0807705105.

[201] J. Schröder, H. Benink, M. Dyba, and G. V. Los, "In vivo labeling method using a genetic construct for nanoscale resolution microscopy", *Biophysical Journal*, vol. 96, no. 1, pp. 1–3, 2009, ISSN: 00063495. DOI: 10.1016/j.bpj.2008.09.032.

[202] G. Lukinavicius, K. Umezawa, N. Olivier, A. Honigmann, G. Yang, T. Plass, V. Mueller, L. Reymond, I. R. Corrêa, Z.-G. Luo, C. Schultz, E. a. Lemke, P. Heppenstall, C. Eggeling, S. Manley, and K. Johnsson, "A near-infrared fluorophore for live-cell super-resolution microscopy of cellular proteins.", *Nature Chemistry*, vol. 5, no. 2, pp. 132–9, 2013, ISSN: 1755-4349. DOI: 10.1038/nchem.1546.

[203] A. N. Butkevich, H. Ta, M. Ratz, S. Stold, S. Jakobs, V. N. Belov, and S. W. Hell, "Two-color 810 nm STED Nanoscopy of Living Cells with Endogenous SNAP-tagged Fusion Proteins", *ACS Chemical Biology*, acschembio.7b00616, 2017, ISSN: 1554-8929. DOI: 10.1021/acschembio.7b00616.

[204] G. Lukinavičius, C. Blaukopf, E. Pershagen, A. Schena, L. Reymond, E. Derivery, M. Gonzalez-Gaitan, E. D'Este, S. W. Hell, D. Wolfram Gerlich, and K. Johnsson, "SiR–Hoechst is a far-red DNA stain for live-cell nanoscopy", *Nature Communications*, vol. 6, no. 1, p. 8497, Dec. 2015, ISSN: 2041-1723. DOI: 10.1038/ncomms9497.

[205] A. N. Butkevich, G. Y. Mitronova, S. C. Sidenstein, J. L. Klocke, D. Kamin, D. N. Meineke, E. D'Este, P. T. Kraemer, J. G. Danzl, V. N. Belov, and S. W. Hell, "Fluorescent Rhodamines and Fluorogenic Carbopyronines for Super-Resolution STED Microscopy in Living Cells", *Angewandte Chemie - International Edition*, vol. 55, no. 10, pp. 3290–3294, 2016, ISSN: 15213773. DOI: 10.1002/anie.201511018.

[206] S. Waldchen, J. Lehmann, T. Klein, S. Van De Linde, and M. Sauer, "Light-induced cell damage in live-cell super-resolution microscopy", *Scientific Reports*, vol. 5, pp. 1–12, 2015, ISSN: 20452322. DOI: 10.1038/srep15348.